Study of molecular properties in inorganic and combustion chemistry employing coupled cluster and density functional methods

by

Beulah Sugandhini Narendrapurapu

(Under the Direction of Henry F. Schaefer III)

Abstract

Reactions on the C_3H_5 potential energy surface (PES) were investigated using the coupled cluster methodology with an unrestricted Hartree-Fock reference wavefunction. Accurate energetics of the reactions on the PES was obtained, within the focal point scheme, using correlation treatments as extensive as coupled cluster with perturbative quadruple excitations [CCSDT(Q)]. The computed barrier heights should enable future studies of C_3H_5 species and related systems which are of critical importance in combustion chemistry. In another study, density functional theory (DFT) was employed to understand the role of hydrogen bonding in NiN_2S_2 complexes related to Nickel Superoxide Dismutase (Ni-SOD). Analysis of molecular orbital compositions, natural charges and point electrostatic potentials provide insights into the significance of H-bonding in assisting nickel based oxidation as opposed to thiolate oxidation in Ni-SOD models. Finally, the metal-metal and metal-ligand equilibrium bond distances of six transition metal compounds were computed using DFT with small, medium and large basis sets. The general reliability of small basis sets, such as the Hood-Pitzer sets, for predicting structural parameters were investigated in the study.

Index words: combustion chemistry, coupled cluster theory, focal point analysis, nickel superoxide dismutase, density functional theory, basis sets.

Study of molecular properties in inorganic and combustion chemistry employing coupled cluster and density functional methods

by

Beulah Sugandhini Narendrapurapu

B.Sc., Osmania University, 2006

M.Sc., Indian Institute of Technology Bombay, 2008

A Dissertation Submitted to the Graduate Faculty

of The University of Georgia in Partial Fulfillment

of the

Requirements for the Degree

Doctor of Philosophy

Athens, Georgia

2013

Study of molecular properties in inorganic and combustion chemistry employing coupled cluster and density functional methods

by

Beulah Sugandhini Narendrapurapu

Approved:

Major Professors:	Henry F. Schaefer III
Committee:	Gary Douberly Geoffrey Smith

Electronic Version Approved:

Maureen Grasso
Dean of the Graduate School
The University of Georgia
May 2013

Study of molecular properties in inorganic and combustion chemistry employing coupled cluster and density functional methods

Beulah Sugandhini Narendrapurapu

April 29, 2013

Dedication

Dedicated to my mother, Mrs. Ruth Priyadarshini Vakiti.

Acknowledgments

I am forever indebted to my mother, Mrs. Ruth Priyadarshini Vakiti, for her unconditional love and for providing all the support and inspiration required to pursue knowledge and education. She believed that the greatest gift she can give her children is a sound education and for this she has battled many a difficulty and has set an example for me to emulate. I thank her for praying for me and encouraging me during the course of my graduate school. I sincerely thank my wonderful advisor, Prof. Henry Schaefer for his guidance and constant support. His encouragement in research and teaching has meant so much to me. I thank him for allowing me the opportunity to teach at South Georgia College, and it was a valuable teaching experience during graduate school. My sincere thanks to Dr. Andrew Simmonett, who mentored me in my first year and showed me how to use various computational chemistry packages. He patiently answered all my questions and provided valuable guidance on the research projects.

Linda Lacy and Prof. Michael Lacy adopted me as their daughter and were always there for me right from the time I stepped into the United States. They made my adjustment to the new culture very smooth and provided all the support and encouragement I needed to do well in graduate school. I thank them for their friendship and for all the numerous rides, lunches and talks in these five years. I cannot forget the love of my two brothers and, especially, my sister who bore with all my complaints and swinging moods and, yet, always saw my positive side.

Katie Compaan has been a wonderful friend and office-mate for three years. I enjoyed the study group she hosted at her apartment which facilitated fruitful dicussions. Her cake (especially, cheese-cake) baking and cutting skills will forever be remembered. I thank Dr. Justin Turney and Dr. Jeremiah Wilke for answering all my questions related to research and

technical difficulties. I thank my colleagues, Qianyi, Peter and Brandon for their friendship and all the members of CCQC for providing a congenial atmosphere to work. Dr. Eric Gale and Dr. Todd Harrop from the chemistry department have been excellent collaborators, on the Ni-SOD project. I also thank the chemistry faculty members, Prof. Schleyer, Prof. Allen, Dr. Yamaguchi, Prof. Duncan for teaching structure and bonding, quantum chemistry and spectroscopy courses which were very valuable for my understanding of computational chemistry.

Behind the scenes, my room-mates and friends, Priyanka, Sajini, Charu, Mayuri, Sanhita and Shruthi are the ones who eased my complaints/regrets and celebrated my little successes. Priyanka has always softened the rough edges in graduate school with her encouragement and humor. I shared some of the memorable and fun moments with my friends in Athens of whom I should name Bo and Brian, and I thank all the friends whom I did not name here. I am grateful for the fellowship with other graduate students from Georgia Christian Grads at the University of Georgia. Last but not the least, I thank the Lord Almighty who sustains the universe and lets man imitate and explore His creative genius, which makes science possible.

Contents

List of Figures

List of Tables

Chapter 1

Introduction and background

1.1 Combustion Chemistry

Combustion of fuel unleashes the energy upon which many modern devices run. At the same time, fuel combustion leads to the production of polyaromatic hydrocarbons (PAHs). These are the major components of soot, which are carcinogenic and/or mutagenic in nature, and pose serious toxicological, environmental and technical problems.[1–4] An understanding of chemical reactions that lead to PAH formation and growth are important to address environmental problems and to improve the efficiency of flames. The formation of the first aromatic ring is widely accepted as the rate determining step in the formation of PAHs. The newly formed aromatic rings grow toward PAHs by Hydrogen-abstraction-C_2H_2-addition mechanism, commonly termed HACA.[5] The HACA mechanism is initiated by abstraction of H atom from an aromatic precursor, followed by addition of C_2H_2 to the free radical formed in the H-abstraction step. Repetitive cycles of HACA eventually lead to the accumulation of new aromatic rings. Two pathways have been proposed for the formation of the first aromatic ring, namely, the odd-carbon-atom pathway which involves C3 species and the even-carbon-atom pathway involving C2 and C4 species. There is much debate about which of the two pathways is important in the formation of benzene ring, but now, it is generally accepted that the odd-electron (C3) pathway is the dominant one.

Propargyl and allyl radicals, both of which have three carbon atoms are important precursors in soot formation. Resonant stabilization makes allyl and propargyl radicals

resistant to O_2 attack and leads to a significant build-up of their population in fuel-rich flames[6] such as propane and butane. Marinov and co-workers investigated aromatic and PAH formation in methane, ethane, ethylene, propane and butane flames employing a combination of experiments and kinetic models.[7–10] The studies indicated that propargyl recombination ($C_3 + C_3$) pathway was the dominant pathway to benzene formation. They also proposed a second most important reaction between propargyl and allyl, in their study of atmospheric-pressure propane flame.[10] Reaction between propargyl and allyl is a two-step process leading to the formation of fulvene. In rich flames, fulvene is converted to benzene by H-atom assisted isomerization.[11] An alternate even-odd-carbon-atom sequence to soot formation includes the reaction of propargyl radicals (C_3H_3) with acetylene (C_2H_2) to yield the cyclopentadienyl radical (C_5H_5). The latter can react in multiple steps to benzene.

In the context of soot formation in combustion chemistry, reaction of propyne with hydrogen is an important reaction and it proceeds through multiple channels. The abstraction of methyl hydrogen channel,

$$CH_3CCH + H \leftrightarrow CH_2CCH + H_2, \tag{1.1}$$

provides a source of propargyl radicals. Reaction of propyne with hydrogen atoms connects the so called odd-carbon-atom and even-carbon-atom channels via two consecutive steps,

$$CH_3CCH + H \leftrightarrow CH_3CHCH \tag{1.2}$$

$$CH_3CHCH \leftrightarrow C_2H_2 + CH_3. \tag{1.3}$$

The reaction also catalyzes the mutual isomerization of propyne and allene in two steps,

$$CH_3CCH + H \leftrightarrow CH_3CCH_2 \tag{1.4}$$

and

$$CH_3CCH_2 \leftrightarrow CH_2CCH_2 + H. \tag{1.5}$$

In the first step, 2-propenyl is formed by addition of H to terminal carbon. 2-propenyl dissociates in the second step to form allene, which in turn undergoes H-abstraction to generate propargyl according to the reaction,

$$CH_2CCH_2 + H \leftrightarrow CH_2CCH + H_2. \tag{1.6}$$

All these reactions as well as the reverse reactions such as the dissociation of allyl, 1-propenyl and 2-propenyl radicals lie on the C_3H_5 potential energy surface (PES). The rates and product distributions of these elementary reactions have been studied experimentally in the past. In 1976, Whytock, Payne and Steif obtained rate constants for the propyne + H reaction at temperatures from 215 to 460 K and pressures in the range 5–600 Torr.[12] Recently, Bentz *et al.* studied the same reaction in a shock tube at higher temperatures, 1200 to 1400 K, and at pressures between 1.3 and 4.0 atm.[13] At low temperatures as those in Whytock *et al.*, the reaction is kinetically controlled leading to the formation of CH_3CCH_2 (see Equation 1.4). This is because the barrier for adding H to terminal carbon in propyne is smaller than for the central carbon. At temperatures greater than 700 K, addition of H atom to the central carbon takes over. Therefore, the propargyl + H_2 and the C_2H_2 + CH_3 channels are predominant at higher temperatures (see equations 1.1–1.3).

Apart from experiments, an understanding of the mechanism of soot formation comes from kinetic modeling and theoretical chemistry. With the help of kinetic models, one can infer the rate coefficients of reactions in a broad temperature and pressure range. Recently, Miller *et al.* have employed time dependent multiple-well master equation (ME)[14–21] for kinetic modeling of the unimolecular and bimolecular reactions on the C_3H_5 PES.[22] The ME method also models non-equilibrium (irreversible) chemical processes such as the dissociation

of weakly bound radicals like allyl, 1-propenyl and 2-propenyl reactions. A weakly bound radical is one in which a free radical dissociates primarily to a stable molecule and another free radical. Such radicals dissociate rapidly at high temperatures owing to their small bond energies and require single-well (multiple-product) ME methodology for evaluation of phenomenological rate constants. ME methodology employs rate constants determined from the potential energy surface using transition-state theory (TST). An accurate prediction of rate constants, in turn, requires electronic structure methods that can compute very precise barrier heights. Rising computing power has made it possible to obtain answers within chemical accuracy using quite large *ab initio* computations in Quantum Chemistry. In the first chapter, high accuracy coupled-cluster method is used to compute very precise barrier heights for reactions on the C_3H_5 PES. A brief description of theoretical methods is discussed int he following sections.

1.2 Theoretical Methods

Determination of the electronic structure of a chemical species involves solving the Schrödinger equation with the electronic Hamiltonian. Since, Schrödinger equation cannot be solved exactly for non-hydrogen-like systems, approximations have to be made. Hartree-Fock (HF) theory is the starting point for solving the many-body hamiltonian. It approximates the total electronic wavefunction to the variationally optimized linear combination of products of one electron wavefunctions which is often expressed as a Slater determinant. Implicit in this approximation is the assumption that each electron moves independently of all others and 'feels' only the Coulomb repulsion due to the average positions of all other electrons (and also exchange interaction as a consequence of antisymmetrization). In reality, electrons avoid each other due to instantaneous Coulomb repulsion and their motion is said to be 'correlated'. The difference between the exact energy and the HF energy in the complete basis set limit

is called correlation energy which, in other words, is the interaction energy of electrons with opposite spins. Even though HF wavefunctions typically recover ∼99% of total electronic energy, it is the remaining 1% electron correlation energy which is critical for accurate and quantitative evaluation of molecular energies and properties. Methods that improve on the HF energy by adding the correlation energy are called Post-Hartree-Fock methods which differ from one another in the type of orbital occupations and weighting factors of different configurations considered. Coupled cluster (CC) method is a very efficient method that takes the basic HF model and constructs multi-electron wavefunctions employing the exponential cluster operator to recover electron correlation energy. It was first introduced to electronic structure by Čížek and Paldus.[23,24]

In the coupled cluster formalism, the wavefunction is expressed as an exponential ansatz,

$$|\Psi\rangle = e^{\hat{T}}|\Phi_0\rangle, \tag{1.7}$$

where $\hat{T}$ is the cluster operator which is a sum of all excitation operators such as single $\hat{T}_1$, double $\hat{T}_2$ and triple $\hat{T}_3$ excitation operators and Φ_0 is, typically, the Hartree-Fock reference determinant.

$$\hat{T} = \hat{T}_1 + \hat{T}_2 + \hat{T}_3 + \cdots \tag{1.8}$$

The exponentiated cluster operator ($\hat{T}$) when acts on the reference determinant, Φ_0, produces the wavefunction containing cluster functions each of which correlates the motion of electrons within specific orbitals. For practical purposes, the cluster operator is truncated at double, triple or quadruple excitation operators. In the CCSD (coupled cluster singles and doubles) formalism, the cluster operator is the sum of only single and double excitation operators,

$$|\Psi\rangle = e^{\hat{T}_1+\hat{T}_2}|\Phi_0\rangle. \tag{1.9}$$

By rewriting the exponential operator using power series expansion, the CCSD wavefunction can be expressed as

$$|\Psi\rangle = \left(1 + \hat{T}_1 + \hat{T}_2 + \frac{(\hat{T}_1 + \hat{T}_2)^2}{2!} + \frac{(\hat{T}_1 + \hat{T}_2)^3}{3!} + \cdots\right)|\Phi_0\rangle. \tag{1.10}$$

The expression not only contains the single and double excitation operators but also the triple excitation operators such as $\hat{T_1}^3$, $\hat{T_1}\hat{T_2}$ and quadruple excitation operators such as $\hat{T_1}^4$, $\hat{T_2^2}$. This shows that as a consequence of an exponential ansatz, higher order excitation character is introduced in the CCSD method even though the cluster operator contains only single and double excitation operators. Similarly, the cluster operator in CCSDT (coupled cluster singles, doubles and triples) method is truncated at the triple excitation operator but includes higher order excitation operators such as $\hat{T_3}^2$. Due to the iterative nature of coupled cluster solution, the computational cost of this method is very high. The CCSD method scales as $\mathcal{O}(N6)$ whereas the CCSDT method scales as $\mathcal{O}(N8)$. The intermediate-level method, CCSD(T) is called the 'golden standard' of quantum chemistry because its computational cost is lower than that of the CCSDT method and predicts very accurate energies (within 1-2 kcal/mol) when combined with basis sets such as cc-pVTZ and cc-pVQZ. It is an improvement over CCSD method in which the triples contribution ($\hat{T_3}$) is estimated approximately as a perturbative correction (non-iterative) to doubles. Similarly, the CCSDT(Q) method applies approximate quadruples contribution to the CCSDT method.

1.3 Focal Point Analysis (FPA)

In Quantum Chemistry, molecular orbitals are described as linear combinations of atomic orbitals which are a set of functions centered on each atom. The term 'basis set' is used to describe these atom-centered functions and their mathematical forms are often

gaussian functions. It is in this atomic orbital basis that the solutions to the non-relativistic Schrödinger equation are obtained. Including an infinite number of basis functions will provide all the freedom necessary to describe the molecular orbitals accurately. However, in practice, the number of functions in a given basis set are finite, leading to basis set truncation error. The basis set error in obtaining energies can be reduced by systematically increasing the basis set size

The correlation consistent basis sets constructed by Dunning are widely used in quantum chemistry.[25,26] They are denoted by cc-pVXZ, where X is the cardinal number that represents the number of functions used to describe the valence electrons of each atom. These basis sets are constructed in such a way that those with higher cardinal number have higher angular momentum functions. This leads to a consistency in the convergence of absolute and relative energies with increasing cardinal number. Hartree-Fock energy, which exhibits exponential dependence[27] on the maximum angular momentum in the basis set, varies with the cardinal number as

$$E_{HF}(X) = A + Be^{-CX}. \tag{1.11}$$

Hartree-Fock energy in the complete basis set (CBS) limit is the asymptote of the above expression and is given by

$$E_{HF}(\infty) = \lim_{X\to\infty} A + Be^{-CX} = A. \tag{1.12}$$

Hartee-Fock method is relatively less basis set dependent than correlated methods because it is a one electron method utilizing one-particle basis set. For correlated methods, the wavefunction decays rapidly as two electrons approach one another. Helgaker and co-workers[28] have demonstrated that correlation energy (E_{corr}) decreases with increasing cardinal number as

$$E_{corr}(X) = A + BX^{-3}. \tag{1.13}$$

In the complete basis set limit, correlation energy is given by the expression,

$$E_{corr}(\infty) = \lim_{X \to \infty} A + BX^{-3} = A. \tag{1.14}$$

Apart from the basis set incompleteness error, the insufficient treatment of electron correlation by a method introduces errors in relative energies. The focal point approach developed by Allen and co-workers[29–34] gives accurate results for relative energies by extrapolating the energies towards basis set and correlation limit following a simple procedure. In the focal point approach, geometries of all the species on the potential energy surface are optimized only once at reasonably high level of theory. Using the reference geometries, a series of single point energies are computed by systematically increasing the basis set size and correlation treatment until a level permitted by the size of the system. The potential energy surface is quadratic in nature around the equilibrium geometries and small deviations from equilibrium structures cause only small deviations in absolute energies. These errors are in turn canceled while computing absolute energies. Hence, there is no need to re-optimize the structures for computing single point energies.

In a typical focal point table, the columns consist of energy changes for a given reaction computed using hierarchy of levels, $HF \rightarrow MP2 \rightarrow CCSD \rightarrow CCSD(T) \rightarrow CCSDT \rightarrow CCSSDT(Q)$. For the post Hartree-Fock methods, the columns are incremental energy changes rather than total energy changes. For example, the δCCSD column consists of CCSD energy increment to the MP2 energy.

$$\delta CCSD = \Delta E_{CCSD} - \Delta E_{MP2} \tag{1.15}$$

Sometimes, focal point tables include additive corrections for higher order correlation treatments in which computations are affordable with only a few basis sets and are insufficient for performing rigorous extrapolation. In the additive approximation, the energy difference

between two correlation methods is calculated with a small basis set and it is appended to the energy computed by the lower level correlation method in the complete basis set limit. For example, the CCSDT energy in the complete basis set limit, according to the additive approximation will be

$$E^{\infty}_{CCSDT} = E^{\infty}_{CCSD(T)} + E^{cc-pVDZ}_{CCSDT} - E^{cc-pVDZ}_{CCSD(T)} \tag{1.16}$$

For well-behaved single reference systems, the incremental corrections become negligible for higher order correlation treatments. The focal point method is a very flexible and inexpensive and can be used to obtain relative energies within 0.1 kcal/mol accuracy.

1.4 Nickel Superoxide Dismutase

Superoxide ($O_2^{\bullet -}$) is a cytotoxic byproduct of aerobic metabolism and high levels of this reactive oxygen species has been associated with various diseases such cancer, diabetes, Parkinson's and Alzheimer's. In order to manage high concentrations of $O_2^{\bullet -}$, aerobic organisms have enzymatic defense systems known as superoxide dismutases (SODs). The SOD enzymes catalyze the transformation of $O_2^{\bullet -}$ to H_2O_2 and O_2 by alternate oxidation and reduction, respectively, of their metal centers. The co-ordination environment is responsible for tuning the redox potential of the metal co-factor into a range accessible by the SOD [-0.04 to 1.09 V vs Ag/AgCl (-0.16 to 0.89 V vs. NHE) at pH 7.0]. Based on the transition metal co-factor, three isoforms of SOD exist, namely, Cu/Zn, Mn or Fe and Ni SODs. Nickel superoxide dismutase (Ni-SOD) is recently discovered and is different from other SODs in terms of protein fold, co-ordination geometry and unusual donors such as anionic carbamido-N, N-terminal amine and cysteine thiolates. Crystallographic studies of Ni-SOD reveal that the active site is monomeric. In the reduced state ($Ni\text{-}SOD_{red}$), Ni(II) is co-ordinated to N-terminal amine of His1, the anionic carboxamido-N of Cys2, and the

cysteine thiolates of Cys2 and Cys6 in a N_2S_2 square planar geometry. In the oxidized state (Ni-SOD_{ox}), Ni(III) is bound to imidazole-N of His1 at the apical position (see Figure 1.1). The cysteine thiolates are important in modulating the Ni(II)/Ni(III) redox couple to physiologically relevant potentials.[35,36] However, it is known that nickel complexes with sulfur donors quickly undergo oxidation by reactive oxygen species such as $O_2^{\bullet -}$ to sulfoxides.[37,38] How Ni-SOD undergoes nickel based oxidation, despite the presence of thiolates susceptible to oxidation is intriguing and has been a subject of study for many years.

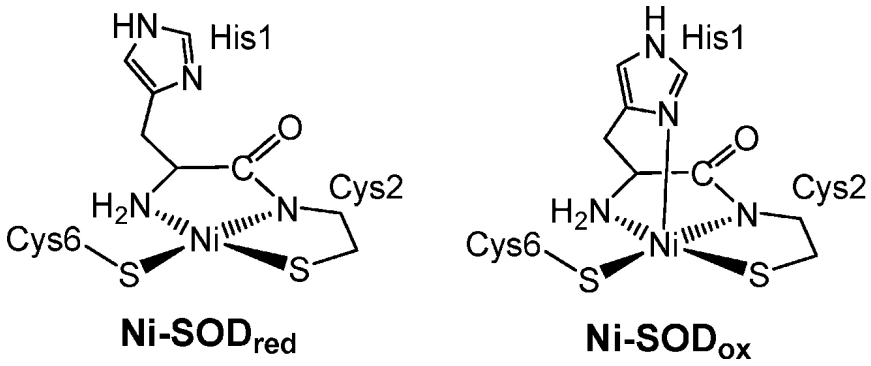

Figure 1.1: Active Site of Ni-SOD_{red} (left), Ni-SOD_{ox} (right)

In 2005, Fiedler, A. T and co-workers optimized truncated models of Ni-SOD_{red} and Ni-SOD_{ox} and computed bond lengths that were similar to those observed in crystallographic studies,[39] except for the axial Ni-N bond. The Ni-N_{axial} bond was greatly underestimated; the computed bond length was 2.16 Å as opposed to the crystallographic value of 2.35 Å. In order to account for the discrepancy in Ni-N_{axial} bond length in oxidized state, residues (Glu17 and Arg47) capable of hydrogen-bonding with the imidazole N-H were introduced. A constrained optimization was performed to account for their natural positioning in the protein. This added interaction effected a lengthening of the Ni-N bond by 0.1 Å, still much

shorter than the experimentally determined value. Analysis of frontier molecular orbitals of Ni-SOD_{red} revealed 25 % Ni and 68 % S character in highest occupied molecular orbital (HOMO) and 37 % Ni and 44 % S character in HOMO-1, clearly showing sulfur dominated frontier molecular orbitals in the reduced state. Moreover, the HOMO is characterized by π-antibonding interactions between Ni (d_{xz}/d_{yz}) orbitals and S lone pairs. In the oxidized state, SOMO is 77 % Ni based and resides in the d_{z^2} orbital with bonding interaction with the imidazole-N lone pair, and not engaging in any S-antibonding interactions. The study suggests that binding of the axial N-donor also may serve to protect the coordinated cysteinates from oxidative modifications by almost completely removing S contributions from the SOMO of Ni-SOD_{ox}.

Hydrogen-bonding to the coordinated cysteinates has also been implicated in a protective role against S-oxidation via lowering the energy of S(p) lone pairs, effectively decreasing destabilizing Ni-S anti-bonding contributions to the HOMO.[38,40] In fact, a close inspection of the Ni-SOD active site reveals potential H-bonding interactions between the Cys6-S and the peptide-NH from Val8 and Gly7.[41] Recently, Gale and Harrop synthesized model complexes of Ni-SOD_{red} that incorporate H-bonds by a series of thiolate modifications. We performed electronic structure computations employing density functional theory on these model complexes to investigate the molecular level changes due to thiolate modification and hydrogen bonding. Composition of frontier molecular orbitals, natural charges on atoms and electrostatic potentials on Ni, N and S atoms were analyzed and the results are presented in chapter 3.

1.5 Density Functional Theory

Traditional wavefunctional methods which are very useful in achieving high chemical accuracies are limited to small systems, usually of the order of ten valence electrons. Density

functional theory (DFT) is a very powerful quantum mechanical tool for solving the many body problem and is an ideal method for system sizes as those of Ni-SOD. The success of DFT is due to the fact that it is based on electron density(ρ) of a system which is a function of only three variables, unlike the wavefunction which is a function of 3N variables (where N refers to the number of in the system). The total energy of a system is a unique functional of electron density of the system:

$$E = \hat{F}(\rho(x, y, z)). \tag{1.17}$$

If we know the exact mathematical form of the functional, we can compute the energy of the system exactly. However, the exact form of the functional or the way to systematically determine the functional is not known. Therefore, one has to resort to empirical results or compare against *ab initio* methods to construct the density functional. A number of density functional methods have been developed in the past and the most famous of them is the Becke's three parameter hybrid functional, B3LYP. In the Ni-SOD study, is the HandyCohen optimized exchange pure density functional, OLYP was employed to obtain geometries of Ni-SOD model complexes that were close to crystallographic values.

1.6 Role of Basis set in Density Functional Theory

Significant advances have been made in developing improved density functionals over the past years and the newly developed functionals are known for their favorable prediction of properties ranging from geometries to reaction energies. Most of the commonly used functionals have been determined by fitting the parameters in DFT to empirical data.[42–45] These DFT methods are developed by either using basis set free (numerical DFT) methods or by employing limited number of basis sets (usually, double or triple-ζ) quality for the fits.

In chapter 4, I have studied the basis set dependency of 35 DFT methods for predicting structures of mononuclear and binuclear transition metal compounds.

References

(1) Denissenko, M. F.; Pao, A.; Tang, M. S.; Pfeifer, G. P. *Science* **1996**, *174*, 430.

(2) Durant, J. L.; Busby, W. F.; Lafleur, A. L.; Penman, B. W.; Crespi, C. L. *Mutat. Res.* **1996**, *371*, 123.

(3) Richter, H.; Howard, J. B. *Phys. Chem. Chem. Phys.* **2002**, *4*, 2038–2055.

(4) Miller, J. A.; Pilling, M. J.; Troe, J. *Proc. Combust. Inst.* **2005**, *30*, 43–88.

(5) Frenklach, M.; Wang, H. *Proc. Combust. Inst.* **1991**, *23*, 1559.

(6) Hansen, N.; Miller, J. A.; Taatjes, C. A.; Wang, J.; Cool, T. A.; Law, M. E.; Westmoreland, P. R. *Proc. Combust. Inst.* **2007**, *31*, 1157–1164.

(7) Miller, J. A.; Melius, C. F. *Combust. Flame* **1992**, *91*, 21–39.

(8) Marinov, N. M.; Pitz, W. J.; K., W. C. *Combust. Flame* **1998**, *114*, 192.

(9) Marinov, N. M.; Pitz, W. J.; K., W. C. *Combust. Sci. Technol.* **1996**, *116*, 211–287.

(10) Marinov, N. M.; Castaldi, M. J.; Melius, C. F.; Tsang, W. *Combust. Sci. Technol.* **1997**, *128*, 295–432.

(11) Miller, J. A.; Klippenstein, S. J.; Georgievskii, Y.; Harding, L. B.; Allen, W. D.; Simmonett, A. C. *J. Phys. Chem. A* **2010**, *114*, 4881–4890.

(12) Whytock, D. A.; Payne, W. A.; Stief, L. J. *J. Chem. Phys.* **1976**, *65*, 191–195.

(13) Bentz, T.; Giri, B. R.; Hippler, H.; Olzmann, M.; Striebel, F.; Szöri, M. *J. Phys. Chem. A* **2007**, *111*, 3812–3818.

(14) Miller, J. A.; Klippenstein, S. J. *J. Phys. Chem. A* **2006**, *110*, 10528–10544.

(15) Miller, J. A.; Klippenstein, S. J.; Robertson, S. H. *J. Phys. Chem. A* **2000**, *104*, 7525–7536.

(16) Klippenstein, S. J.; Miller, J. A. *J. Phys. Chem. A* **2002**, *106*, 9267–9277.

(17) Miller, J. A.; Klippenstein, S. J. *J. Phys. Chem. A* **2003**, *107*, 2680–2692.

(18) Fernandes-Ramos, A.; Miller, J. A.; Klippenstein, S. J.; Truhlar, D. G. *Chem. Rev.* **2006**, *106*, 4518–4584.

(19) Miller, J. A.; Klippenstein, S. J. *J. Phys. Chem. A* **2003**, *107*, 7783–7799.

(20) Miller, J. A.; Klippenstein, S. J. *J. Phys. Chem. A* **2004**, *108*, 8296–8306.

(21) Miller, J. A.; Klippenstein, S. J. *2002* **106**, 4904–4913.

(22) Miller, J. A.; Senosiain, J. P.; Klippenstein, S. J.; Georgievskii, Y. *J. Phys. Chem. A* **2008**, *112*, 9429–9438.

(23) Čížek, J. *Adv. Chem. Phys.* **1969**, *14*, 35.

(24) Čížek, J.; Paldus, *J. Quantum Chem.* **1971**, *5*, 359.

(25) Dunning, T. H., Jr. *J. Chem. Phys.* **1989**, *90*, 1007.

(26) Wilson, A. K.; van Mourik, T.; Dunning, T. H., Jr. *Journal of Molecular Structure: THEOCHEM* **1996**, *388*, 339.

(27) Feller, D. *J. Chem. Phys.* **1993**, *98*, 7059.

(28) Helgaker, T.; Klopper, W.; Koch, H.; Noga, J. *J. Chem. Phys.* **1997**, *106*, 9639.

(29) Császár, A. G.; Allen, W. D.; Schaefer, H. F. *J. Chem. Phys.* **1998**, *108*, 9751.

(30) East, A. L. L.; Allen, W. D. *J. Chem. Phys.* **1993**, *99*, 4638.

(31) Gonzales, J. M.; Pak, C.; Cox, R. S.; Allen, W. D.; Schaefer, H. F.; Császár, A. G.; Tarczay, G. *Chem. -Eur. J.* **2003**, *9*, 2173.

(32) Allen, W. D.; East, A. L. L.; Császár, A. G. In *Structures and Conformations of Non-Rigid Molecules*; Laane, J., Dakkouri, M., van der Veken, B., Oberhammer, H., Eds.; Kluwer: Dordrecht, 1993; pp 343–373.

(33) Császár, A. G.; Tarczay, G.; Leininger, M. L.; Polyansky, O. L.; Tennyson, J.; Allen, W. D. In *Spectroscopy from Space*; Demaison, J., Sarka, K., Eds.; Kluwer: Dordrecht, 2001; pp 317–339.

(34) Schuurman, M. S.; Muir, S. R.; Allen, W. D.; Schaefer, H. F. *J. Chem. Phys.* **2004**, *120*, 11586.

(35) Choudhury, S. B.; Lee, J. W.; Davidson, G.; Yim, Y. I.; Bose, K.; Sharma, M. L.; Kang, S. O.; Cabelli, D. E.; Maroney, M. J. *Biochemistry* **1999**, *38*, 3788.

(36) Krüger, H.-J.; Peng, G.; Holm, R. H. *Inorg. Chem.* **1991**, *30*, 734.

(37) Jenney, F. E.; Verhagen, M.; Cui, X. Y.; Adams, M. W. W. *Science* **1999**, *286*, 306.

(38) Grapperhaus, C. A.; Darensbourg, M. Y. *Acc. Chem. Res.* **1998**, *31*, 451.

(39) Fiedler, A. T.; Bryngelson, P. A.; Maroney, M. J.; Brunold, T. C. *J. Am. Chem. Soc.* **2005**, *127*, 5449.

(40) Mullins, C. S.; Grapperhaus, C. A.; Kozlowski, P. M. *J. Biol. Inorg. J. Biol. Inorg. Chem.* **2006**, *11*, 617.

(41) Barondeau, D. P.; Kassmann, C. J.; Bruns, C. K.; Tainer, J. A.; Getzoff, E. D. *Biochemistry* **2004**, *43*, 8038.

(42) Becke, A. *J. Chem. Phys.* **1997**, *107*, 1997.

(43) Becke, A. *J. Chem. Phys.* **1998**, *109*, 2092.

(44) Becke, A. *Phys. Rev. A* **1998**, *38*, 3098.

(45) Becke, A. *J. Chem. Phys.* **1993**, *98*, 5648.

Chapter 2

Combustion Chemistry: Important Features of the C_3H_5 Potential Energy Surface, Including Allyl Radical, Propargyl + H_2, Allene + H, and Eight Transition States*

*Narendrapurapu, B. S.; Simmonett, A. C.; Schaefer, H. F., III *J. Phys. Chem A* **2011**, *115*, 14209. Reprinted here with the permission of the publisher.

2.1 Abstract

The C_3H_5 potential energy surface (PES) encompasses molecules of great significance to hydrocarbon combustion, including the resonantly stabilized free radicals propargyl (plus H_2) and allyl. In this work, we investigate the interconversions that take place on this PES, using high level coupled cluster methodology. Accurate geometries are obtained using coupled cluster theory with single, double and perturbative triple excitations [CCSD(T)], combined with Dunning's correlation consistent quadruple-ζ basis set cc-pVQZ. The energies for these stationary points are then refined by a systematic series of computations, within the focal point scheme, using the cc-pVXZ (X = D, T, Q, 5, 6) basis sets and correlation treatments as extensive as coupled cluster with full single, double, and triple excitation and perturbative quadruple excitations [CCSDT(Q)]. Our benchmarks provide a zero-point vibrational energy (ZPVE) corrected barrier of 10.0 kcal mol^{-1} for conversion of allene + H to propargyl + H_2. We also find that the barrier for H addition to a terminal carbon atom in allene, leading to propenyl is 1.8 kcal mol^{-1} lower than that for addition to a central atom to form the allyl radical.

2.2 Introduction

Resonantly stabilized free radicals (RSFRs) play an important role in the chemistry of fuel rich flames owing to their high formation and relatively low destruction rates, compared to reactive radicals not stabilized by resonance. The relatively high abundance of RSFRs elevates the significance of their reactions with closed- and open-shell hydrocarbons, leading to propagation and termination reactions.[1,2] Such reactions are primarily responsible for the rate-determining first aromatic ring formation of polycyclic aromatic hydrocarbons (PAHs), which are the major components of soot. Propargyl and allyl radicals have resonantly stabilized structures and are important precursors in soot formation, particularly in allene and propyne flames.[3] One important route to the formation of the first aromatic ring, which may be rate determining step for soot formation under certain conditions, is the odd-carbon-atom pathway ($C_3 + C_3$) which involves the recombination of propargyl radicals;[4–7] the analogous reaction of propargyl radical with allyl is well-known,[8] but is now believed to contribute less significantly to aromatic formation.[9] While the recombination of propargyl radicals can occur in one step, the reaction of propargyl with allyl to form benzene occurs in multiple steps wherein benzene is formed by H-atom assisted isomerization of fulvene.

Additional free radical constituents of fuel rich flames include 1-propenyl and 2-propenyl radicals, which are formed by H addition to propyne at the central and terminal carbons, respectively. Depending on the bond energies, the free radicals in combustion flames decompose by H abstraction or by a single or multiple bond fissions to produce radical fragments or other stable hydrocarbons.[2] Due to resonant stabilization in allyl, it has a C-C bond energy of 55 kcal mol^{-1} and hence decomposes via C-H bond fission. On the other hand, 1-propenyl and 2-propenyl dissociate via C-C bond fissions. All these reactions occur over multiple interconnected potential wells of the C_3H_5 potential energy

surface (PES), and the kinetics of these reactions have been studied both theoretically and experimentally in the past.[10–23] Other reactions that lie on the C_3H_5 PES include the isomerization reactions between allyl, 1-propenyl and 2-propenyl. Given the significance of these processes, Miller, Senosiain, Klippenstein and Georgievskii (MSKG) perfomed a detailed study of their kinetics.[24] The barrier heights of these reactions on the C_3H_5 PES were computed from electronic structure methods and used in conjunction with Master Equation (ME) methodology, offering detailed insight into the kinetics. The MSKG barrier heights were evaluated as differences between the extrema of the QCISD(T) single point energies computed along the B3LYP intrinsic reaction coordinate (IRC). Although the electronic structure methods accounted for basis set incompleteness, and the effects of triple excitations through quadratic configuration interaction theory, a correction to some barrier heights ranging from -0.63 to -2.34 kcal mol^{-1} was required to obtain quantitative agreement of calculated rate coefficients from the ME analysis with experimental values. There are numerous possible sources of this discrepancy, including deficiencies in experiments, the treatment of internal degrees of freedom and the electronic structure methods themselves. The present study aims to address the electronic structure aspects by providing precise energies for the stationary points on the C_3H_5 PES, carefully analyzing the effects of correlation energy and basis set size.

2.3 Methods

The varied electronic structure encountered across the C_3H_5 PES complicates the choice of methodology. Restricted open-shell Hartree-Fock (ROHF) based methods lead to spurious symmetry breaking in the allyl radical, perhaps the most important of the stationary points, due to artifactual localization of the radical on one of the terminal carbon atoms. This can be averted using multi-reference methods with an active space spanning the

$1a_2, 1b_1, 2b_1$ orbitals, but such an active space cannot easily be generalized to the other bonding patterns encountered across the PES. Motivated by this, we opted to use coupled cluster theory with an unrestricted Hartree-Fock reference function. It has been shown that, even with severely contaminated reference wavefunctions, the powerful correlation treatment provided by coupled cluster theory results in negligible deviations from spin purity.[25,26] In order to show that the coupled cluster method is insensitive to the choice of the reference wavefunction, $\langle \hat{S}^2 \rangle$ values at the unrestricted coupled cluster with single and double excitations (UCCSD) level of theory were computed for all open shell structures.

All geometries were optimized using the UCCSD method with perturbative triple excitations [UCCSD(T)][27,28] and Dunning's correlation consistent cc-pVQZ basis set;[29] the corresponding restricted Hartree-Fock (RHF) based approach was used for closed shell systems. To further refine the relative energies, a series of single point energies was computed using Dunning's correlation consistent family of basis sets, cc-pVXZ (X=D,T,Q,5,6)[29,30] and correlation treatments as extensive as coupled cluster with single, double and full triple excitations (CCSDT)[27,28,31–34] and CCSDT with perturbative quadruple excitations [CCSDT(Q)],[35,36] within the focal point scheme of Allen and co-workers.[37–42] The focal point analysis seeks the complete basis set limit result by extrapolation of a hierarchy of results with various bases, while monitoring the convergence of each successive correlation treatment up to CCSDT(Q), to gauge how close the result is to the full configuration interaction (FCI) limit. The Hartree-Fock (HF) energies were extrapolated according to the equation[43]

$$E_{HF}(X) = E_{HF}^{\infty} + A \exp(-BX), \tag{2.1}$$

where X is the cardinal number of the correlation consistent cc-pVXZ basis; in this work, the Hartree-Fock (HF) energies were extrapolated using the series X=Q,5,6. Likewise, the

correlation energies were extrapolated using the functional form[44]

$$E_{corr}(X) = E_{corr}^{\infty} + CX^{-3} \tag{2.2}$$

and the cc-pVXZ (X=5,6) basis sets. In this work, second order Møller -Plesset perturbation theory (MP2) energies were extrapolated, and all post-MP2 correlation treatments were applied additively. The additive approximation is invoked by explicitly computing the difference between successive correlation treatments using the largest feasible basis set, and assuming this difference is constant for all basis sets larger than that explicitly computed. The additivity approach is a manifestation of the well-calibrated assumption that higher order excitations are less basis set dependent than lower-order terms, particularly doubles. In our focal point tables, any results displayed in square brackets have been obtained by either extrapolation or the assumption of additivity. For efficiency, the single point energies were computed within the frozen core approximation, with core correlation effects later accounted for using the following equation:

$$\Delta E_{\rm core} \approx E_{\rm cc-pCVTZ}^{\rm AE-CCSD(T)} - E_{\rm cc-pCVTZ}^{\rm FC-CCSD(T)} \tag{2.3}$$

In Eqn. (2.3), the terms AE and FC refer to all-electron and frozen-core computations, respectively. Relativistic effects were considered by appending mass velocity and Darwin one-electron terms, computed at the cc-pVQZ CCSD(T) level of theory.[45,46] Finally, zero point vibrational energy corrections were computed from cc-pVTZ CCSD(T) harmonic vibrational frequencies. The Mainz-Austin-Budapest (MAB) version of ACESII,[47] PSI3,[48] MOLPRO2009.1[49] and Kállay's MRCC[50,51] programs (interfaced to MAB-ACESII) were used for the computations.

2.4 Results and Discussion

Our computed relative energies are shown in 2.1, along with the MSKG's results for comparison. In order to simplify this comparison, we have adopted MSKG's structure naming convention, which is shown graphically in 2.2, and the values are tabulated with and without inclusion of zero point vibrational energies (ZPVE), to better account for any deviations. The relative energies from the MSKG study agree well with our benchmarked values, deviating by less than 1 kcal mol^{-1}; the more important interconversions will be discussed in more detail below. Predictably, the largest discrepancies are observed for barrier heights, where the elongated bonds in the transition states present a significant challenge for electronic structure theory in general. Also shown in 2.1 are the $\langle \hat{S}^2 \rangle$ values for open shell structures computed at the UHF and UCCSD levels of theory, using the cc-pVTZ basis set. A number of the open shell species have UHF wavefunctions that exhibit severe spin contamination with $\langle \hat{S}^2 \rangle$ values as high as 1.11 (*c.f.* 0.75 for a pure doublet electronic state), but the UCCSD values never deviate by more than 0.012 from the ideal value. We can expect that the spin contamination will be further removed with the inclusion of higher order correlation effects, giving us confidence in the UCCSD(T) methodology. For clarity, the forward and reverse barrier heights for the various interconversions considered here are also shown in 2.1.

The allene + H entrance channel can proceed over **ts1**, yielding the allyl radical, or over **ts3** to form the 2-propenyl radical. Both experiment and theory agree that the latter is faster, which is consistent with our finding that the **ts3** barrier is lower than **ts1** by 1.8 kcal mol^{-1}. However, MKSG noted a discrepancy between their computed rate for the allyl channel, and the experimental value of Wagner and Zellner, which was lower by a factor of 4.[17] As shown in 2.1, our barrier height for **ts1** is 0.1 kcal mol^{-1} greater than MSKG's without zero point vibrational corrections, and 0.5 kcal mol^{-1} greater with the consideration of ZPVE. . But the correction applied in the MSKG study results in a 2.01 kcal mol^{-1} lower

barrier height compared to ours. The focal point analysis of the **ts1** barrier is shown in 2.2. Little basis set sensitivity is observed for this barrier, with the cc-pVQZ and complete basis set limit (CBS) MP2 values differing by less than 0.1 kcal mol^{-1}. The addition of perturbative quadruple excitations reduces the predicted barrier height by just 0.07 kcal mol^{-1}, giving us confidence in the reliability of our final prediction. The monotonic reduction of our predicted barrier height, with increasing correlation treatment, suggests that our value represents an upper bound. While it is beyond the scope of this work to pinpoint the exact source of discrepancies between the kinetics studies, our benchmarks indicate that the MSKG barrier for **ts1** is slightly too low, due to the absence of higher-order correlation effects, which will contribute to an increased predicted rate. It is worth noting that the experiments of Tsang and Walker[20] predicted a higher rate coefficient than that of Wagner and Zellner; this higher rate is consistent with a lower barrier.

Our barrier height for **ts3** is greater than MSKG's by 0.5 kcal mol^{-1} when ZPVE is neglected, and 1 kcal mol^{-1} when ZPVE is included; the corresponding focal point analysis is shown in 2.3. As with the **ts1** barrier, a monotonic decrease of the barrier is observed upon increasing correlation treatment. If oscillatory behavior were observed upon introducing higher excitations, we would see some degree of error cancellation among higher-order terms; because the pattern is monotonic in this case, the higher order effects become important for precise energetics. Indeed, the post CCSD(T) correlation treatments effect a 0.6 kcal mol^{-1} reduction in the barrier height for **ts3**, relative to allene + H. The **ts3** barrier height, like **ts1**, is not particularly sensitive to the basis set used, and appears converged close to the full configuration interaction (FCI) limit, with a perturbative quadruples contribution of just -0.05 kcal mol^{-1}.

The barrier height for transition state **ts6**, which connects CH_3CHCH-*trans* (hydrogens in trans configuration) to the dissociation products methyl radical and acetylene, had to be reduced by a sizeable 2.34 kcal mol^{-1} in the MSKG study, in order to reproduce the

experimentally observed kinetics. Our focal point analysis for this barrier is shown in 2.4. As with the barrier heights discussed previously, our value for the **ts6** is well converged towards the CBS and FCI limits. However, an oscillatory trend appears when progressing from Hartree-Fock theory, towards FCI. Consequently, there is partial cancellation of the post CCSD(T) correlation effects and our final value for the barrier agrees with the uncorrected MSKG barrier within 0.2 kcal mol^{-1}. This close level of agreement between our accurate benchmark values and MKSG's uncorrected result further reaffirms Diau and Lin's suspicion[13] that the experimental values of Holt and Kerr,[15] used to derive the MSKG correction, may not be reliable.

Our relative energy for the stationary point corresponding to the dissociated products of CH_3CHCH-*trans* isomer – namely CH_3+C_2H_2, connected by **ts6** – is 0.78 kcal mol^{-1} higher than that obtained in the MSKG study. This deviation is mainly due to differences in the ZPVEs. The valence focal point analysis, shown in 2.5, shows that neither basis set error nor post-CCSD(T) effects contribute appreciably to this energy difference, which explains the good performance of MSKG's QCISD(T) methodology for the relative energies.

In the above analysis, we have focused mainly on the reactions where discrepancies were observed between theoretical and experimental rate computations. We should note that in general, the agreement between our barriers and the MSKG values are very good. Furthermore, most of the MSKG barrier heights did not require any adjustment to match the experimental data. For brevity, we have omitted the focal point analyses for the remaining stationary points in 2.1 but have provided them as supplementary material in appendix A.

2.5 Conclusions

The C_3H_5 potential energy surface includes many interesting species of critical importance in hydrocarbon combustion. Using state-of-the-art quantum chemical methods, we have

provided accurate energetic data for a number of C_3H_5 stationary points, which should enable future studies of C_3H_5 species, and related systems. While MSKG had to lower some barrier heights in their theoretical kinetics study, to match the experiments, our results exonerate their electronic structure methods as the source of discrepancy; for example, their ZPVE-corrected **ts6** barrier was lower than our benchmark value by 0.2 kcal mol^{-1} and a further reduction to match experiment only increases this gap. Our focal point decompositions of the relative energies yield understanding into the importance of the various excitation levels encountered in the coupled cluster hierarchy, and should act as a guide for methodology choice in related combustion chemistry studies.

2.6 Acknowledgements

This research was supported by the Department of Energy, Basic Energy Sciences, Division of Chemical Sciences, Fundamental Interactions Team, Grant No. DEFG02-97-ER14748. This research used the resources of the National Energy Research Scientific Computing Center (NERSC), supported by the Office of Science of the U.S. Department of Energy under Contract No. DE-AC02-05CH11231.

2.7 Figures

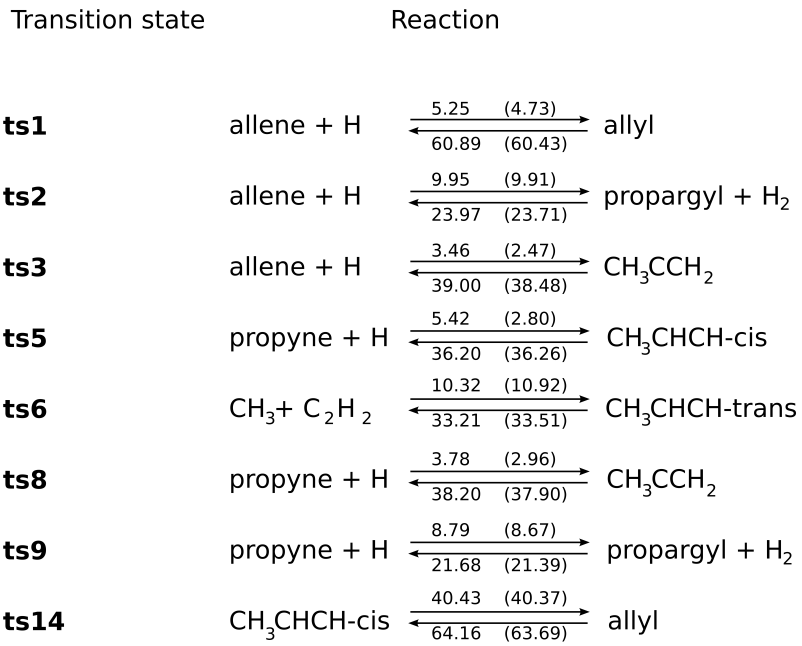

Figure 2.1: Barrier heights (kcal mol^{-1}) for forward and backward reactions on the C_3H_5 potential energy surface. The values in parentheses are from the related study by MSKG.[24]

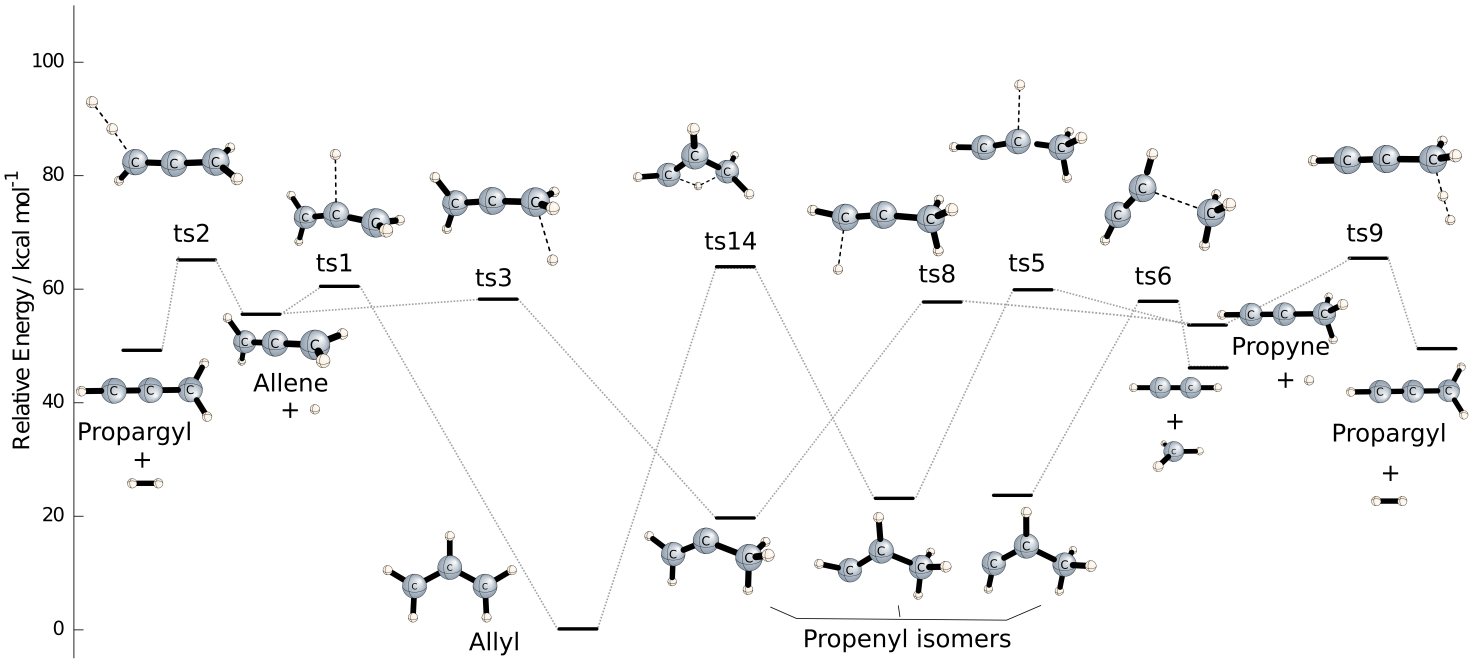

Figure 2.2: A sketch of the C_3H_5 potential energy surface, depicting the nomenclature adopted for each stationary point, and their relative energies.

2.8 Tables

Table 2.1: Hartree-Fock and coupled cluster $\langle \hat{\mathbf{S}}^{\mathbf{2}} \rangle$ expectation values and energies (kcal mol^{-1}), relative to the allene + H entrance channel, for the species considered herein.

	This work			MSKG[a]
	cc-pVTZ UHF $\langle \hat{S}^2 \rangle$	cc-pVTZ UCCSD $\langle \hat{S}^2 \rangle$	E_∞ , (E_∞+ZPVE)[b]	E_∞ , (E_∞+ZPVE)[c]
allene+H	- , 0.75	- , 0.75	0.00 (0.00)	0.00 (0.00)
propyne+H	- , 0.75	- , 0.75	−1.42 (−1.13)	−1.47 (−1.08)
CH_3+C_2H_2	0.762 , -	0.75 , -	−9.32 (−8.52)	−9.34 (−9.30)
C_3H_3+H_2	0.965 , -	0.756 , -	−11.53 (−14.02)	−11.44 (−13.80)
allyl	0.955	0.759	−62.61 (−55.65)	−62.59 (−55.70)
CH_3CCH_2	0.924	0.755	−42.37 (−35.54)	−42.43 (−36.02)
CH_3CHCH-*trans*	0.944	0.755	−38.43 (−31.41)	−38.58 (−31.90)
CH_3CHCH-*cis*	0.941	0.755	−38.80 (−31.91)	−38.96 (−32.38)
ts1	1.048	0.758	3.92 (5.25)	3.82 (4.73)
ts2	1.111	0.762	11.56 (9.95)	11.61 (9.91)
ts3	1.021	0.757	2.25 (3.46)	1.75 (2.47)
ts5	0.945	0.754	2.85 (4.29)	2.54 (3.87)
ts6	1.049	0.759	−0.99 (1.81)	−1.13 (1.62)
ts8	0.922	0.753	1.53 (2.66)	0.97 (1.88)
ts9	0.884	0.753	8.94 (7.66)	8.74 (7.59)
ts14	1.011	0.757	4.94 (8.52)	4.71 (7.99)

[a] Miller, Senosiain, Klippenstein and Georgievskii (Ref. 24).

[b] Complete basis set limit energies, from our focal point analyses, with core correlation and relativistic corrections appended.

[c] Quadratic configuration interaction theory with single, double, and perturbative triple excitations energies, extrapolated to the complete basis set limit.

Table 2.2: Valence focal point analysis of the relative energy (in kcal mol^{-1}) of **ts1** with respect to allene+H.[a]

	HF	+δMP2	+δCCSD	+δCCSD(T)	+δCCSDT	+δCCSDT(Q)	ΔE_e[CCSDT(Q)]
cc-pVDZ	+6.78	+9.68	−10.01	−0.17	−0.64	−0.07	[+5.56]
cc-pVTZ	+6.84	+8.96	−10.56	−0.25	−0.69	[−0.07]	[+4.23]
cc-pVQZ	+6.89	+8.83	−10.77	−0.31	[−0.69]	[−0.07]	[+3.87]
cc-pV5Z	+6.91	+8.79	[−10.77]	[−0.31]	[−0.69]	[−0.07]	[+3.85]
cc-pV6Z	+6.91	+8.80	[−10.77]	[−0.31]	[−0.69]	[−0.07]	[+3.86]
∞	[+6.91]	[+8.81]	[−10.77]	[−0.31]	[−0.69]	[−0.07]	[+**3.88**]
ΔE_0(final)	=	ΔE_e[CBS CCSDT(Q)] + $\Delta E_{\rm core}$ + $\Delta E_{\rm relativity}$ + $\Delta E_{\rm ZPVE}$					
	=	3.88 +0.06 -0.01 +1.33 = **5.26 kcal mol^{-1}**					

[a]The symbol δ denotes the increment in the relative energy (ΔE_e) with respect to the preceding level of theory in the hierarchy RHF→ MP2→ CCSD→ CCSD(T)→ CCSDT → CCSDT(Q). Square brackets signify results obtained from basis set extrapolations or additivity assumptions. Final predictions are boldfaced.

Table 2.3: Valence focal point analysis of the relative energy (in kcal mol^{-1}) of **ts3** with respect to allene+H.[a]

	HF	+δMP2	+δCCSD	+δCCSD(T)	+δCCSDT	+δCCSDT(Q)	ΔE_e[CCSDT(Q)]
cc-pVDZ	+4.74	+8.86	−9.04	−0.09	−0.55	−0.05	[+3.87]
cc-pVTZ	+4.75	+8.25	−9.65	−0.16	−0.60	[−0.05]	[+2.54]
cc-pVQZ	+4.81	+8.14	−9.86	−0.21	[−0.60]	[−0.05]	[+2.23]
cc-pV5Z	+4.83	+8.11	[−9.86]	[−0.21]	[−0.60]	[−0.05]	[+2.22]
cc-pV6Z	+4.83	+8.12	[−9.86]	[−0.21]	[−0.60]	[−0.05]	[+2.23]
∞	[+4.83]	[+8.13]	[−9.86]	[−0.21]	[−0.60]	[−0.05]	[+**2.24**]
ΔE_0(final)	=	ΔE_e[CBS CCSDT(Q)] + $\Delta E_{\rm core}$ + $\Delta E_{\rm relativity}$ + $\Delta E_{\rm ZPVE}$					
	=	+2.24 +0.02 -0.01 +1.21 = **+3.46 kcal mol^{-1}**					

[a]See footnote of Table 2.2 for an explanation of the notation used.

Table 2.4: Valence focal point analysis of the relative energy (in kcal mol^{-1}) of **ts6** with respect to allene+H.[a]

	HF	+δMP2	+δCCSD	+δCCSD(T)	+δCCSDT	+δCCSDT(Q)	ΔE_e[CCSDT(Q)]
cc-pVDZ	+2.43	+12.89	−13.32	+0.60	−0.62	−0.10	[+1.87]
cc-pVTZ	+0.95	+11.80	−13.78	+0.59	−0.71	[−0.10]	[−1.25]
cc-pVQZ	+0.99	+11.91	−13.99	+0.55	[−0.71]	[−0.10]	[−1.35]
cc-pV5Z	+1.03	+11.89	[−13.99]	[+0.55]	[−0.71]	[−0.10]	[−1.33]
cc-pV6Z	+1.03	+11.92	[−13.99]	[+0.55]	[−0.71]	[−0.10]	[−1.29]
∞	[+1.03]	[+11.97]	[−13.99]	[+0.55]	[−0.71]	[−0.10]	[−**1.24**]
ΔE_0(final)	=	ΔE_e[CBS CCSDT(Q)] + $\Delta E_{\rm core}$ + $\Delta E_{\rm relativity}$ + $\Delta E_{\rm ZPVE}$					
	=	-1.24 +0.28 -0.03 +2.80 = **+1.81 kcal mol^{-1}**					

[a]See footnote of Table 2.2 for an explanation of the notation used.

Table 2.5: Valence focal point analysis of the relative energy (in kcal mol^{-1}) of $\mathbf{CH_3}$+ $\mathbf{C_2H_2}$ with respect to allene+H.[a]

	HF	+δMP2	+δCCSD	+δCCSD(T)	+δCCSDT	+δCCSDT(Q)	ΔE_e[CCSDT(Q)]
cc-pVDZ	−11.13	+5.87	−3.18	+1.62	+0.02	+0.01	[−6.78]
cc-pVTZ	−13.47	+5.70	−3.67	+1.91	−0.07	[+0.01]	[−9.59]
cc-pVQZ	−13.57	+5.88	−3.74	+2.00	[−0.07]	[+0.01]	[−9.49]
cc-pV5Z	−13.59	+5.86	[−3.74]	[+2.00]	[−0.07]	[+0.01]	[−9.52]
cc-pV6Z	−13.58	+5.87	[−3.74]	[+2.00]	[−0.07]	[+0.01]	[−9.51]
∞	[−13.58]	[+5.89]	[−3.74]	[+2.00]	[−0.07]	[+0.01]	[−**9.49**]
ΔE_0(final)	=	ΔE_e[CBS CCSDT(Q)] + $\Delta E_{\rm core}$ + $\Delta E_{\rm relativity}$ + $\Delta E_{\rm ZPVE}$					
	=	-9.49 +0.20 -0.03 +0.81 = **-8.51 kcal mol^{-1}**					

[a]See footnote of Table 2.2 for an explanation of the notation used.

References

(1) Marinov, N. M.; Pitz, W. J.; Westbrook, C. K.; Castaldi, M. J.; Senkan, S. M. *Combust. Sci. Technol.* **1996**, *116-117*, 211–287.

(2) McEnally, C. S.; Pfefferle, L. D.; Atakan, B.; Kohse-Höinghaus, K. *Prog. Energy Combsut. Sci.* **2006**, *32*, 247–294.

(3) Hansen, N.; Miller, J. A.; Taatjes, C. A.; Wang, J.; Cool, T. A.; Law, M. E.; Westmoreland, P. R. *Proc. Combust. Inst.* **2007**, *31*, 1157–1164.

(4) Miller, J. A.; Klippenstein, S. J. *J. Phys. Chem. A* **2003**, *107*, 7783–7799.

(5) Georgievskii, Y.; Miller, J. A.; Klippenstein, S. J. *Phys. Chem. Chem. Phys.* **2007**, *9*, 4259–4268.

(6) Hansen, N.; Miller, J. A.; Kasper, T.; Kohse-Höinghaus, K.; Westmoreland, P. R.; Wang, J.; Cool, T. A. *Proc. Combust. Inst.* **2009**, *32*, 623.

(7) Miller, J. A.; Melius, C. F. *Combust. Flame* **1992**, *91*, 21–39.

(8) Marinov, N. M.; Castaldi, M. J.; Melius, C. F.; Tsang, W. *Combust. Sci. Technol.* **1997**, *128*, 295–432.

(9) Miller, J. A.; Klippenstein, S. J.; Georgievskii, Y.; Harding, L. B.; Allen, W. D.; Simmonett, A. C. *J. Phys. Chem. A* **2010**, *114*, 4881–4890.

(10) Davis, S. G.; Law, C. K.; Wang, H. *J. Phys. Chem. A* **1999**, *103*, 5889–5899.

(11) Fernandes, R. X.; Giri, B. R.; Hippler, H.; Kachiani, C.; Striebel, F. *J. Phys. Chem. A* **2005**, *109*, 1063–1070.

(12) Hidaka, Y.; Nakamura, T.; Tanaka, H.; Inami, K.; Kawano, H. *Int. J. Chem. Kinet.* **1990**, *22*, 701–709.

(13) Diau, E. W.; Lin, M. C. *Int. J. Chem. Kinet.* **1995**, *27*, 855–866.

(14) Diau, E. W.; Lin, M. C.; Melius, C. F. *J. Chem. Phys.* **1994**, *101*, 3923–3927.

(15) Holt, P. M.; Kerr, J. A. *Int. J. Chem. Kinet.* **1977**, *9*, 185–200.

(16) Hidaka, Y.; Nakamura, T.; Miyauchi, A.; Shiraishi, T.; Kawano, H. *Int. J. Chem. Kinet.* **1989**, *21*, 643–666.

(17) Wagner, H. G.; Zellner, R. *Ber. Bunsen-Ges. Phys. Chem.* **1972**, *76*, 667–672.

(18) Wagner, H. G.; Zellner, R. *Ber. Bunsen-Ges. Phys. Chem.* **1972**, *76*, 518–.

(19) Brown, J. M.; Thrush, B. A. *Trans. Faraday Soc.* **1967**, *63*, 630–642.

(20) Tsang, W.; Walker, J. A. *J. Phys. Chem.* **1992**, *96*, 8378–8384.

(21) Garcia-Dominguez, J. A.; Trotman-Dickenson, A. F. *J. Chem. Soc.* **1962**, 940–944.

(22) Bentz, T.; Giri, B. R.; Hippler, H.; Olzmann, M.; Striebel, F.; Szöri, M. *J. Phys. Chem. A* **2007**, *111*, 3812–3818.

(23) Whytock, D. A.; Payne, W. A.; Stief, L. J. *J. Chem. Phys.* **1976**, *65*, 191–195.

(24) Miller, J. A.; Senosiain, J. P.; Klippenstein, S. J.; Georgievskii, Y. *J. Phys. Chem. A* **2008**, *112*, 9429–9438.

(25) Stanton, J. F. *J. Chem. Phys.* **1994**, *101*, 371–374.

(26) Krylov, A. I. *Annual review of physical chemistry* **2008**, *59*, 433–462.

(27) Raghavachari, K.; Trucks, G. W.; Pople, J. A.; Head-Gordon, M. *Chem. Phys. Lett.* **1989**, *157*, 479.

(28) Stanton, J. F. *Chem. Phys. Lett.* **1997**, *281*, 130.

(29) Dunning, T. H., Jr. *J. Chem. Phys.* **1989**, *90*, 1007.

(30) Wilson, A. K.; van Mourik, T.; Dunning, T. H., Jr. *Journal of Molecular Structure: THEOCHEM* **1996**, *388*, 339.

(31) Watts, J. D.; Gauss, J.; Bartlett, R. J. *Chem. Phys. Lett.* **1992**, *200*, 1.

(32) Watts, J. D.; Gauss, J.; Bartlett, R. J. *J. Chem. Phys.* **1993**, *98*, 8718.

(33) Hampel, C.; Peterson, K. A.; Werner, H.-J. *Chem. Phys. Lett.* **1992**, *190*, 1.

(34) Deegan, M. J. O.; Knowles, P. J. *Chem. Phys. Lett.* **1994**, *227*, 321.

(35) Bomble, Y. J.; Stanton, J. F.; Kállay, M.; Gauss, J. *J. Chem. Phys.* **2005**, *123*, 054101.

(36) Kállay, M.; Gauss, J. *J. Chem. Phys.* **2005**, *123*, 214105.

(37) Császár, A. G.; Allen, W. D.; Schaefer, H. F. *J. Chem. Phys.* **1998**, *108*, 9751.

(38) East, A. L. L.; Allen, W. D. *J. Chem. Phys.* **1993**, *99*, 4638.

(39) Gonzales, J. M.; Pak, C.; Cox, R. S.; Allen, W. D.; Schaefer, H. F.; Császár, A. G.; Tarczay, G. *Chem. -Eur. J.* **2003**, *9*, 2173.

(40) Allen, W. D.; East, A. L. L.; Császár, A. G. In *Structures and Conformations of Non-Rigid Molecules*; Laane, J., Dakkouri, M., van der Veken, B., Oberhammer, H., Eds.; Kluwer: Dordrecht, 1993; pp 343–373.

(41) Császár, A. G.; Tarczay, G.; Leininger, M. L.; Polyansky, O. L.; Tennyson, J.; Allen, W. D. In *Spectroscopy from Space*; Demaison, J., Sarka, K., Eds.; Kluwer: Dordrecht, 2001; pp 317–339.

(42) Schuurman, M. S.; Muir, S. R.; Allen, W. D.; Schaefer, H. F. *J. Chem. Phys.* **2004**, *120*, 11586.

(43) Feller, D. *J. Chem. Phys.* **1993**, *98*, 7059.

(44) Helgaker, T.; Klopper, W.; Koch, H.; Noga, J. *J. Chem. Phys.* **1997**, *106*, 9639.

(45) Perera, S. A.; Bartlett, R. J. *Chem. Phys. Lett.* **1993**, *216*, 606.

(46) Cowan, R. D.; Griffin, D. C. *J. Opt. Soc. Am.* **1976**, *66*, 1010.

(47) Stanton, J. F.; Gauss, J.; Watts, J. D.; Szalay, P. G.; Bartlett, R. J.; with contributions from Auer, A. A.; Bernholdt, D. E.; Christiansen, O.; Harding, M. E.; Heckert, M.; Heun, O.; Huber, C.; Jonsson, D.; Jusélius, J.; Lauderdale, W. J.; Metzroth, T.; Michauk, C.; O'Neill, D. P.; Price, D. R.; Ruud, K.; Schiffmann, F.; Tajti, A.; Varner, M. E.; Vázquez, J.; and the integral packages: MOLECULE (Almlöf, J.; Taylor, P. R.), PROPS (Taylor, P. R.), and ABACUS (Helgaker, T.; Jensen, H. J. Aa.; Jørgensen, P.; Olsen, J.;). Current version see http://www.aces2.de.

(48) Crawford, T. D.; Sherrill, C. D.; Valeev, E. F.; Fermann, J. T.; King, R. A.; Leininger, M. L.; Brown, S. T.; Janssen, C. L.; Seidl, E. T.; Kenny, J. P.; Allen, W. D. *J. Comp. Chem.* **2007**, *28*, 1610–1616.

(49) Werner, H.-J.; Knowles, P. J.; Lindh, R.; Manby, F. R.; Schu tz, M.; Celani, P.; Korona, T.; Mitrushenkov, A.; Rauhut, G.; Adler, T. B.; Amos, R. D.; Bernhardsson, A.; Berning, A.; Cooper, D. L.; Deegan, M. J. O.; Dobbyn, A. J.; Eckert, F.; Goll, E.; Hampel, C.; Hetzer, G.; Hrenar, T.; Knizia, G.; Ko ppl, C.; Liu, Y.; Lloyd, A. W.;

Mata, R. A.; May, A. J.; McNicholas, S. J.; Meyer, W.; Mura, M. E. ; Nicklass, A.; Palmieri, P.; Pflu ger, K.; Pitzer, R.; Reiher, M.; Schumann, U.; Stoll, H.; Stone, A. J.; Tarroni, R.; Thorsteinsson, T.; Wang, M.; Wolf, A. *Molpro2009.1*; Cardiff University; Cardiff, U. K., 2009.

(50) Kállay, M.; Gauss, J. *J. Chem. Phys.* **2005**, *123*, 214105.

(51) Kállay, M.; Surján, P. R. *J. Chem. Phys.* **2001**, *115*, 2945.

Chapter 3

Exploring the Effects of H-Bonding in Synthetic Analogues of Nickel Superoxide Dismutase (Ni-SOD): Experimental and Theoretical Implications for Protection of the Ni–SCys Bond*

*Gale, E. M.; Narendrapurapu, B. S.; Simmonett, A. C.; Schaefer, H. F., III; Harrop, T. C. *Inorg. Chem.* **2010**, *49*, 7080. Reprinted here with the permission of the publisher.

3.1 Abstract

Nickel superoxide dismutase (Ni-SOD) is a recently discovered SOD obtained from soil microbes and cyanobacteria that shares no structural or spectroscopic similarities with other isoforms of SOD. The enzyme is found in both the Ni^{II} (Ni-SOD_{red}) and Ni^{III} (Ni-SOD_{ox}) oxidation states in "as isolated" preparations of the enzyme from two separate and independently crystallized Streptomyces strains. Ni-SOD contains an unusual and unprecedented biological coordination sphere comprised of Cys-S and peptido-N donors. To understand the role of these donors, our collaborators, Gale and Harrop, have synthesized the monomeric $Ni^{II}N_2S_2$ complexes, (Et_4N)[Ni(nmp)(SC_6H_4-p-Cl)] **(2)** and (Et_4N)[Ni(nmp)(S^tBu)] **(3)** as Ni-SOD_{red} models arising from the S,S-bridged precursor molecule, $[Ni_2(nmp)_2]$ **(1)** (where nmp^{2-} = doubly deprotonated form of N-2-(mercaptoethyl)picolinamide). In addition to **2** and **3**, three new complexes, (Et_4N)[Ni(nmp)(S-o-babt)] **(4)**, (Et_4N)[Ni(nmp)(S-meb)] **(5)**, and K[Ni(nmp)(S-NAc)] **(6)** (where –S-o-babt = thiolate of o-benzoylaminobenzene thiol; –S-o-meb = thiolate of N-(2-mercaptoethyl)benzamide; and –SNAc = thiolate of N-acetyl-L-cysteine methyl ester); that provide a unique comparison as to the structural and reactivity effects imparted by H-bonding in square planar asymmetrically-coordinated $Ni^{II}N_2S_2$ complexes, are also synthesized. X-ray structural analysis in combination with cyclic voltammetry (CV), spectroscopic measurements, density functional theory (DFT) calculations and reactivity studies with O2 and various ROS were employed in order to gain insight into the role that H-bonding plays in NiN_2S_2 complexes related to Ni-SOD. The experimental results coupled with our theoretical analysis demonstrate that H-bonding to coordinated thiolates stabilizes S-based molecular orbitals relative to those arising from Ni^{II}, allowing for enhanced Ni contribution to the highest occupied molecular orbital (HOMO), which is predominantly of S-Ni π^* character. These studies provide a unique perspective on the role played by electronically different thiolates regarding the intimately coupled

interplay and delicate balance of Ni- versus S-based reactivity in Ni-SOD model complexes. The reported results have offered new insight into the chemistry that H-bonding/thiolate protonation imparts upon the Ni-SOD active site during catalysis, in particular as a protective mechanism against oxidative modification/degradation.

3.2 Introduction

The superoxide anion radical ($O_2^{\bullet-}$) is an inevitable and cytotoxic byproduct of aerobic metabolism.[1–3] If this reactive oxygen species (ROS) is not eliminated, significant damage to surrounding cells will occur, leading to a variety of disease states.[4] Indeed, the formation of ROS such as superoxide have been implicated in diseases such as diabetes,[2] cancer,[5,6] neurodegenerative disorders like Alzheimer's[3,7] and Parkinson's,[4,8] and the cell death and tissue damage that occurs following stroke or heart attack.[3,9] To combat the adventitious production of this ROS, all aerobes possess metalloenzyme defense systems known as superoxide dismutases (SODs)[4,10] that catalyze the disproportionation of ($O_2^{\bullet-}$) to H_2O_2 and O_2 through alternate oxidation and reduction of their respective metal centers (Equations 3.1 and 3.2). Several distinct types of SOD are known and each is classified by the first-row transition-metal utilized to carry out the chemistry. The more widely studied SODs include the mononuclear Mn-SOD[11] and Fe-SOD,[12,13] and the dinuclear Cu/Zn-SOD,[14] which have been extensively characterized by numerous biochemical, structural and theoretical studies.

$$\boldsymbol{M^{ox}} + O_2^{\bullet-} \rightarrow \boldsymbol{M^{red}} + O_2 \tag{3.1}$$

$$\boldsymbol{M^{red}} + O_2^{\bullet-} + 2H^+ \rightarrow \boldsymbol{M^{ox}} + H_2O_2 \tag{3.2}$$

Recently, a distinct class of SOD has been discovered from Streptomyces soil microbes and cyanobacteria that contain Ni at the active site.[15–18] These new SODs show no sequence

homology with other SODs, have different and unusual primary coordination spheres, and utilize a metal not normally associated with the binding or activation of O_2 (or its derivatives). Structural studies on Ni-SOD reveal a homo-hexameric protein comprised of four-helix bundle subunits that contain the Ni center.[15] The Ni ion in each subunit is located within a "Ni-hook" binding motif consisting of residues one through nine starting at the N-terminus. The "Ni-hook" motif is disordered in the apo protein and in the reduced resting state (Ni-SOD_{red}) houses the Ni^{II} ion in a square planar coordination environment ligated by the thiolates of Cys2 and Cys6 in a cis arrangement. The deprotonated carboxamide from Cys2 and primary amine from His1 complete the N_2S_2 coordination sphere (Figure 3.1). In the oxidized Ni^{III} form (Ni-SOD_{ox}), the geometry changes to square pyramidal via ligation of the imidazole-Nδ side chain of His1 occupying an apical position (Chart 1).[15] The primary coordination sphere of Ni-SOD is distinct from any other metalloenzyme. In fact, there are few known metal sites in biology with an N-terminal amine-N[19] and/or anionic carboxamido-N incorporated within the ligand framework.[20] Additionally, the Ni-SCys bond is a reoccurring theme for redox-active Ni in biology,[21,22] likely present to modulate the redox potential of the Ni ion in order to facilitate electron transfer under physiological conditions.[23] The redox activity of Ni-SOD, however, reacts with $O_2^{\bullet -}$ at a diffusion controlled rate (10^9 M^{-1} s^{-1}) to form O_2 and H_2O_2.[24] Ni-SOD thus catalyzes the (trans)formation of molecular species typically associated with the oxidative modification of thiolate ligands.[25] This activity is in stark contrast to metalloenzymes with redox active Ni centers ligated by Cys-S, such as acetyl coenzyme A synthase/carbon monoxide dehydrogenase[21] and NiFe hydrogenase,[26] which function under reducing environments. It has also been well documented that coordination of thiolates to square planar Ni^{II} centers markedly enhances their sensitivity to O_2 and ROS, due in part to a destabilization of the thiolate -orbitals via a repulsive p(π)-d(π) interaction between the S(p) and Ni(d) orbitals.[27,28] It should be of no surprise then that the stated observations have made Ni-SOD an enzyme of particular interest.[29–41]

This novel class of SODs provides the bioinorganic community a new test-system to understand the features required for SOD's crucial biological function in ROS regulation. To date, there is a paucity of information on small-molecule analogues (low MW, non-peptide-based) of Ni-SOD. Recently, a series of peptide-based maquettes consisting of seven to twelve amino acid residues that are present in the "Ni-hook" region have been synthesized,[32,35,42–44] affording the first examples of functional Ni-SOD analogues. For example, studies by Shearer and co-workers employing [Ni(SOD^{M2})] (where SOD^{M2} = HCDLPCG), which catalytically disproportionates $O_2^{\bullet-}$, provide evidence suggestive of an outer-sphere mechanism for the enzyme.[32] A contradictory study using a similar maquette with the nonapeptide HCDLPCGVY was shown to bind one CN^- at the Ni site supporting an inner-sphere mechanism.[42] It is difficult to delineate the differences between these two very similar systems and the noted differences could be due to the relative instability of some of the maquettes. For example, the nonapeptide Ni-maquette is shown to exist in equilibrium with a 2:1 Ni/peptide and a 1:1 Ni/peptide species in solution.[44] This observation alone warrants the need for more discrete and crystallizable small molecule analogues. One small-molecule analogue directly related to Ni-SOD, namely [Ni^{II}(BEAAM)]$^-$, has been structurally characterized and consists of an $N_{amine}N_{carboxamide}S_2$ primary coordination sphere.[37] The quasi-reversible $Ni^{III/II}$ couple at 120 mV (vs. Ag/AgCl in MeCN) is within the potential window for SOD chemistry but the complex does not disproportionate $O_2^{\bullet-}$.[45] For all known analogue systems, the Ni^{III} state was transiently observed by EPR in only one case[32] and all maquette systems were shown to degrade under aerobic conditions. The synthesis and properties of related $Ni^{II}N_3S$[31,46,47] and $Ni^{II}N_2S_2$[48–50] systems have also been reported to replicate some features of the enzyme. At present, however, no model has been studied which incorporates additional second-sphere effects such as hydrogen-bonding (H-bonding). A close inspection of the Ni-SOD active site reveals potential H-bonding interactions between the Cys6-S and the peptide-NH from Val8 and Gly7.[15] An in silico study

on $Ni^{II}N_2S_2$ Ni-SOD models demonstrated that the incorporation of one H-bond diminished the reactivity/nucleophilicity of the coordinated-S, placing the greatest electron density at the Ni center, consistent with less S-contribution to the HOMO.[25] However, this effect has yet to be tested experimentally.

Previously, Glae *et al.* reported a general methodology towards the preparation of asymmetric square planar $Ni^{II}N_2S_2$ complexes as synthetic analogues of the Ni-SOD_{red} active site.[51] Addition of *para*-chlorobenzene thiolate ($^{-}SC_6H_4$-*p*-Cl) or tert-butyl thiolate ($^{-}S^tBu$) to the dinuclear metallosynthon $[Ni_2(nmp)_2]$ **(1)** (where $nmpH_2$ = N-2-(mercaptoethyl)picolinamide and Hs represent dissociable protons) resulted in S,S-bridge splitting and the formation of the monomeric complexes, $(Et_4N)[Ni(nmp)(SC_6H_4$-*p*-Cl)] **(2)** and $(Et_4N)[Ni(nmp)(S^tBu)]$ **(3)** in high yields, respectively. Both complexes conform as good structural analogues with the pyridyl-N, carboxamido-N and thiolato-S of the nmp^{2-} ligand modeling the contributions of His-1 and Cys-2 in Ni-SOD. The exogenously added thiolate allows for variable (to probe second-sphere effects) and unconstrained modeling of Cys-6 in Ni-SOD utilizing electronically different thiolate ligands. Inspired by the structural and spectroscopic similarities demonstrated by **2** and **3** with Ni-SOD_{red}, viz. their proton accepting capabilities, Gale and Harrop set out to synthesize complexes building off of the Ni(nmp) framework with a peptide functionality capable of engaging in H-bonding with the coordinated thiolates. Indeed, results by Solomon suggest that cysteine thiolates may be protonated during catalysis[52] and theoretical accounts regarding the role played by H-bonding to Ni-coordinated thiolates,[25,53] as well as other metal-bound thiolates in biology,[54–56] have been suggested as mechanisms to protect the CysS donors from oxidative damage. Thus, the objective of the present work was to incorporate key H-bonding functionalities into the model systems and gain a fundamental understanding of what electronic properties they impart on the Ni center germane to SOD catalysis. Herein, we present the electronic structure of five $Ni^{II}N_2S_2$ complexes

which are part of $[Ni(nmp)(SR)]^-$ series, namely $(Et_4N)[Ni(nmp)(SC_6H_4\text{-}p\text{-}Cl)]$ **(2)** and $(Et_4N)[Ni(nmp)(S^tBu)]$ **(3)**, (Et_4N)[Ni(nmp)(S-o-babt)] **(4)** (HS-o-babt = o-benzoylamino benzenethiol), (Et_4N)[Ni(nmp)(S-meb)] **(5)** (HS-meb = N-(2-mercaptoethyl)benzamide), and K[Ni(nmp)(S-NAc)] **(6)** (HS-NAc = N-acetyl-L-cysteine methyl ester) (Chart 1). The synthesis of properties of the newly synthesized compounds, **4**, **5** and **6** will also be discussed briefly.

3.3 Summary of Experimental Results

Complexes **2**-**6** were constructed via three chemically distinct synthetic procedures: (i) direct S,S-bridge splitting of dimer **1**; (ii) a disulfide/coordinated thiolate exchange reaction via the addition of 0.5 mol-equiv of a weaker S_{exo}-donor in its disulfide form; and (iii) thiol/coordinated thiolate exchange through addition of 1 mol-equiv of a less basic S_{exo}-donor in its thiol form (see Figure 3.2). These methodologies provide a facile means to incorporate thiolate ligands of variant donor strength and, in the present account, to introduce secondary sphere interactions such as H-bonding. These ligand variations, along with other types of modifications, have opened up an expansive library of complexes built off of one common metallosynthon, namely the Ni(nmp) fragment. This approach provides a unique opportunity to probe the role played by the cysteine thiolates and the influence of the immediate chemical environment in Ni-SOD, and by analogy, other biomolecules employing Ni-thiolate coordination.[21,22] The existence of intramolecular NH$\cdots$S bonding in the solution-state of complexes **4**-**6** was corroborated by the large downfield chemical shifts observed in the ^{1}H NMR and the red-shifts in ν_{NH} and ν_{CO} in the FTIR spectra compared to those of the disulfide or thiol form of the variable S_{exo} ligand. The intramolecular H-bond is also visible in the X-ray structure of **4**, resulting in a $\sim$0.03 Å contraction of the Ni–S_{exo} bond. Electrochemical measurements revealed significant cathodic shifts in the H-bonded

complexes by 40 mV in the aryl systems **2** and **4** and ∼150-200 mV among the alkyl systems **3**, **5** and **6**. By separately analyzing the complexes featuring aryl- and alkyl-S_{exo} ligands, it becomes clear that the oxidation potentials of the $Ni^{II}N_2S_2$ complexes increase as the donor strength of S_{exo} decreases. Analysis of the trends observed suggests that H-bonding to coordinated thiolates plays a significant role in modulating these potentials much like what has been observed in other synthetic analogue systems.[57] Complexes **2-6** were shown to react with ROS and O_2(g), revealing for the first time, quantitative kinetic information regarding the oxidative stability of Ni-SOD_{red} models. Reaction with O_2(g) under pseudo first-order conditions is a relatively slow process and afforded selective S_{exo} modification at rates on the order of 10^{-5}-10^{-4} s^{-1} in MeCN at 298 K. Reactions with excess H_2O_2 under similar conditions were less discriminate, affording mixtures of species and a rate of decay (10^{-2} s^{-1}) that was several orders of magnitude faster than reaction with O_2(g), although approximately six-fold decrease in k_{obs} was noted for the H-bonded systems **5** and **6**, suggestive of some degree of protection from the H-bonds. Furthermore, addition of excess $O_2^{\bullet -}$ effects no defined changes in the UV spectra (in MeCN) of the complexes and thus does not disproportionate $O_2^{\bullet -}$ under these conditions even in the presence of a potential axial N-donor. These results have provided initial insight into the reactivity trends observed via manipulation of the S_{exo} appended to the Ni(nmp) framework and into how this effect translates into oxidative stability of the Ni-SOD active site.

3.4 Electronic Structure Methods

Supporting theoretical studies were performed by optimizing the geometries of **2-6** using density functional theory (DFT). The OPTX pure exchange functional of Handy and Cohen[58] was used in conjunction with the Lee-Yang-Parr correlation functional;[59] this method is commonly denoted as OLYP. To correctly describe the more diffuse regions

of the charge density within each molecule, where the negative charge resides, the large def2-TZVPP basis set[60] was used. In addition to geometry optimizations, the atomic charges and the contributions from each atom to the highest occupied molecular orbital (HOMO) were computed. The geometry optimizations were performed using the QChem3.2[61] package, which also provided atomic charges via its implementation of the natural bond orbital theory software NBO 5.0.[62] The ORCA[63] program was used to obtain orbital compositions within the Löwdin and Mulliken population analysis (MPA) definitions, which yielded essentially identical compositions; for this reason only the Löwdin compositions are reported. Electrostatic potentials were also computed with the ORCA package.

3.5 Results and Discussion

DFT computations were employed in order to obtain electronic descriptions of the Ni-SOD model complexes. Previous DFT accounts on Ni-SOD models have focused on the role of the mixed amine/carboxamido-N coordination sphere, where it was concluded that the presence of the mixed N-ligands supports Ni-based redox chemistry to protect the active site from S-based oxidation.[30,34] Other DFT studies have focused on the impact of H-bonded H_2O molecules (absent in Ni-SOD) in $Ni^{II}N_2S_2$ and $Fe^{II}N_4S$ complexes establishing the passive versus active nature of H-bonding in these discrete systems.[64] The present research therefore offers the first opportunity to look at S-based modification (H-bonding) of synthesized small molecule analogues directly related to Ni-SOD from both an experimental and theoretical approach. The initial coordinates for complexes **2**-**5** were obtained from the X-ray structures (that of **6** from an estimate utilizing coordinates from **2**) and the geometries were optimized with the OLYP functional (def2-TZVPP basis set). A full summary of the optimized structures including NBO atomic charges, electrostatic potentials, and relevant atomic coordinates can be found in Table 5 and with complete detail in appendix B. The geometry

optimization of **2-6** compare well with the experimentally determined metric parameters (Figure 3.3 for **3** and **5**, Figures S17-S21 and Tables S7-S8 in the supplementary material for the rest). The optimized models reproduce the coordination geometry with small overestimates in the Ni–L bond lengths, providing bond distances within 0.05 Å of the experimental values. The overestimate in bond lengths is well within the accuracy of the OLYP functional. It is important to note that DFT replicates the asymmetric nature of the different N-donors in **2-6** and is consistent with the strong ligand-field of the carboxamido-N versus the pyridine-N donor. Additionally, the optimized models accurately replicate the longer Ni–S bond length from the monodentate S_{exo}-donor. The only noteworthy divergence is found for **5**, which DFT optimizes to include the presence of an intramolecular NH$\cdots$S H-bond (3.3). The latter result is not too surprising considering this H-bond interaction has been established in solution (vide supra). Collectively, the accuracy with which the structures generated by DFT replicate the experimental metric parameters validates the computations employed in the present work. Insights into the influence of H-bonding on the metric parameters of **4-6** are observed in the DFT calculated structures. Optimized models of **5** and **6** reveal a contraction of the Ni–S_{exo} bond by $\sim$0.03 Å versus **3** upon formation of intramolecular H-bonds with concurrent shortening of the Ni–$N_{carboxamide}$ bond by $\sim$0.10 Å, which is reflective of charge neutralization of the trans thiolate (3.3, 3.1, and Figure S21). The Ni–S_{exo} bond contraction observed by DFT and in the structure of **4** has been postulated to be due to a decrease in the filled/filled repulsive interaction between the Ni(dπ) and S(pπ) orbitals upon H-bond formation. A study of *in silico* Ni-SOD_{red} models revealed a similar contraction in an H-bonded S-ligand of the same magnitude.[25] Additionally, a DFT study on a truncated model of the Ni-SOD_{red} active site reveals contraction of the Ni–S bond distance upon protonation of Cys6 or Cys2 by $\sim$0.03 Å.[30] All H-bonding interactions observed in the DFT generated structures are clearly directed towards S_{exo}, as a result of the strong trans influence of the carboxamido-N, in addition to the orientation and proximity of the

NH to S_{exo}. The distances between S_{exo} and the N of the appended carboxamide range from 2.935 Å (**4**) to 3.209 Å (**5**) and are slightly less than the N$\cdots$S distances between Cys6 with Val8 (3.35 Å) and Gly7 (3.45 Å) in Ni-SOD.[15] This result is likely due to the absence of other secondary interactions present in the enzyme. However, a similar N–S_{exo} of 2.954 Å is observed in the X-ray crystal structure of **4** (Figure 1, Table 1).

The important issues to address regarding Ni-SOD function is how the enzyme avoids S-based oxygenation in the presence of O_2 and ROS and how Ni^{III} is stabilized during catalytic turnover without resulting in S-oxidation. A partial solution lies in the electronic structural description of the active site and relevant synthetic analogues. A number of descriptors, such as HOMO composition,[30] atomic charges and electrostatic potentials[25] can be envisaged to determine the preference for oxidation at the Ni center or the ligands. The key bonding features of the frontier MOs, as well as the percent Ni- and S-contribution to these MOs, are displayed in Figure 3.4, Tables B2 –3.4, and in the supporting information presented in appendix B. For all complexes, the LUMO remains π-antibonding between the C(pπ) orbitals on the pyridine ring of the nmp ligand. The nature of the HOMO and HOMO-1 principally involve π-antibonding interactions between the S-π-orbitals and the Ni d-π-orbitals, reflecting the high degree of covalency in the Ni–S bond of these complexes. If we separately analyze the series containing *alkyl* S_{exo} ligands, ordered by decreasing electron releasing capability, a clear trend emerges amongst the HOMO compositions. Within this series, the Ni contributions of **3**, **5** and **6** increase to 48.6%, 58.4% and 61.2%, respectively, accompanied by a decrease in contributions from S_{exo} (and total S) to 29.2% (39.0% total S), 21.0% (26.3% total S) and 17.9% (22.0% total S), respectively (Figure 7, Tables 6-8). The close lying HOMO-1 for **3** (46.7% Ni; 32.4% total S), 5 (48.0% Ni; 31.0% total S) and 6 (47.0 % Ni, 32.9% total S) also contains mostly Ni-character. *This trend implies that decreased electron density at the coordinated alkyl thiolate increases the feasibility of metal-based redox.* Surprisingly, the NBO atomic charges on the exogenous thiolates of **3**, **5**

and **6** correspond to -0.36, -0.39 and -0.36, respectively, and do not reflect this trend. The charges on the Ni center remain essentially constant as well and correspond to 0.65, 0.66 and 0.66, respectively. Electrostatic potential (ESP) maps have been used to rationalize the susceptibility of attack by an electrophile/oxidant,[25] however, they can be computationally expensive without resorting to a point-charge approximation. A simpler approach, which affords a more quantitative comparison, is to compute the ESP analytically at the positions of the nuclei, which has been advocated as a powerful reactivity index by Galabov and coworkers.[65,66] Using this method, we obtain ESPs (in a.u.) at the S_{exo} of -59.4518, -59.4280 and -59.4245 for **3**, **5** and **6**, respectively (Figure 6, and the supporting information in appendix B). The ∼0.03 a.u. difference of the ^{t}BuS-derivative **3** implies stabilization of an oxidizing agent at that S-atom's position by ∼0.65 eV or 15 kcal/mol relative to the H-bonded derivatives **5** and **6**. These values are more consistent with the electron releasing properties of the ligands and they accurately correlate the donor strength of the ligand with the nucleophilicity of the S_{exo}-donor. The negative of the HOMO orbital energies of **3**, **5** and **6** correspond to -0.34 eV, -0.52 eV and -0.57 eV, respectively (Figure 7, Tables 6-8), and the trend correlates well with the experimentally determined oxidation potentials (vide supra) in keeping with Koopmans' theorem.[67] The atomic charges on the aryl-S_{exo} of **2** and **4** are -0.18 and -0.26, respectively, (see Figures S17 and S19 in appendix B) and, as expected, reflect significantly depleted electron density relative to their alkyl congeners. This decrease in electron density is matched by reduced contributions from the S_{exo} to the HOMO, with S_{exo} of **2** and **4** contributing only 0.5% (40.3% total S) and 0.4% (41.8% total S), respectively. In contrast to **3**, **5** and **6**, the differences between the Ni contributions to the HOMO arising from **2** and **4** vary much less, ranging from 42.3% to 41.3% for **2** and **4**, respectively. The HOMO energies tend to be lower than those in the alkyl S_{exo} systems, which possess less contracted lone pairs on S, consistent with the conjecture that repulsive d(π)-p(π) interactions between Ni and S raise the energy of the HOMO.[25,27,28,30] As before,

the experimental oxidation potentials of **2** and **4** match the relative trends in the negative of the HOMO energies which are found to be -0.73 eV and -0.88 eV, respectively. Previous computational studies suggest that the effects of protonation or H-bonding to coordinated thiolates impart profound effects on the electronic structures of some analogous NiN_2S_2–SOD model systems.[25,30] Our results reveal that the atomic charges on the thiolato-S of **2**-**6** do not reflect the presence of the H-bond; as the atomic charges on the S-atoms of **3**, **5** and **6** are relatively invariant. These values are rather unexpected, given that H-bonding is expected to deplete the electron density at S. Thus, H-bonding does not appear to shift charge away from S to a significant extent, however, evidence of charge neutralization at S is reflected in the more positive ESP. Even though charge density is polarized away from a particular nucleus it is still assigned to the same atom if it is closest to that nucleus. Therefore, the positive induced dipole is not reflected in charge if polarization is small, as in H-bonding. Notwithstanding the fact that ligand donor strength also plays a role, we can see that the ESPs of the monodentate thiolate ligands of **5** and **6**, which possess intramolecular H-bonds, are lower than that of **3** (Figure 6). The same effect is observed for the monodentate thiolate of **4**, which possesses a lower ESP than that of **2** (see the supporting information in appendix B). Thus, it appears that H-bonding to coordinated thiolates is manifested in a decreased ESP, and not the atomic charges. *This effect, coupled with the decrease in thiolato-S contribution to the HOMO and concurrent increase in that arising from Ni, strongly suggests that H-bonding to Ni-bound thiolates results in a reduced propensity for ligand-based oxidation.* Taken together, the presence of intramolecular H-bonds in Ni-SOD may, *in combination* with the unique set of N-donor ligands present, provide a means of protecting the coordinated Cys-S donors during catalysis.

3.6 Conclusions

In summary, we have performed electronic structure computations on five $Ni^{II}N_2S_2$ complexes of the general formula $[Ni^{II}(nmp)(SR)]^-$ which conform nicely as structural biomimetics of the Ni-SOD_{red} active site. DFT optimized models of **2-6** were generated and reflect those determined experimentally by crystallography. The effect of H-bond incorporation is clearly demonstrated in the frontier MOs of the Ni^{II} complexes. In the alkyl-S_{exo} systems, H-bonding serves to stabilize both the LUMO and HOMO by ∼0.30 and 0.20 eV, respectively. Additionally, H-bonding results in significantly more Ni- and less S-character in the HOMO and low-lying HOMO-1 of **5** and **6** compared to the non-H-bonded complex **3**. ESP calculations of the H-bonded S_{exo} in **5** and **6** also reveal a 15 kcal/mol stabilization against oxidants with respect to **3**. Thus, H-bonding to coordinated thiolates reveals multiple degrees of systemic changes reflected in the solid-state structures, redox potentials, spectroscopic properties and electronics. These observations advocate an approach whereby the H-bonded cysteine thiolates found in the Ni-SOD active site may be protected from oxidative modification. This degree of protection may be more significant in Ni-SOD_{red} as the principle bonding interactions are defined by the highly covalent nature of the π-based HOMO and HOMO-1, containing a large amount of both Ni- and CysS-character.[30] Upon coordination of the His1 N_{Im} in Ni-SOD_{ox}, the MOs rearrange to define a principally Ni-based (d_{z^2}) σ-bonding feature in the HOMO.[30] The different character in Ni-SOD_{ox} provides the rationale for Ni- versus S-based redox chemistry in this state of the enzyme, since no significant S-character is observed in the HOMO. Site-directed mutagenesis studies confirm the necessity of this bond[68] and some suggest that the Ni–N_{His1} bond remains throughout catalysis.[32] Obviously, this interaction is presently absent in our models systems; however, efforts are underway to further elucidate this crucial interaction in our laboratory.

3.7 Acknowledgements

T. C. H. acknowledges support from an NSF CAREER Award (CHE-0953102), the Department of Chemistry at the University of Georgia (UGA) for startup funds, and the UGA Research Foundation (UGARF) for a faculty research award. H. F. S. acknowledges support from the NSF (CHE-0749868). We wish to thank Franklin E. Leach III and Prof. I. Jonathan Amster for assistance with the high resolution ESI-MS measurements. We also wish to thank Dr. Ashis K. Patra for assistance with X-ray crystallography.

3.8 Supporting Information

X-ray crystallographic data including CIF files, high-resolution ESI-MS of 6, computational results including Cartesian coordinates, optimized geometries and MO diagrams of 2 and 4, UV-vis and ESI-MS results of the O_2(g), H_2O_2, and superoxide studies and complete reference.[?] This material is available free of charge via the Internet at http://pubs.acs.org.

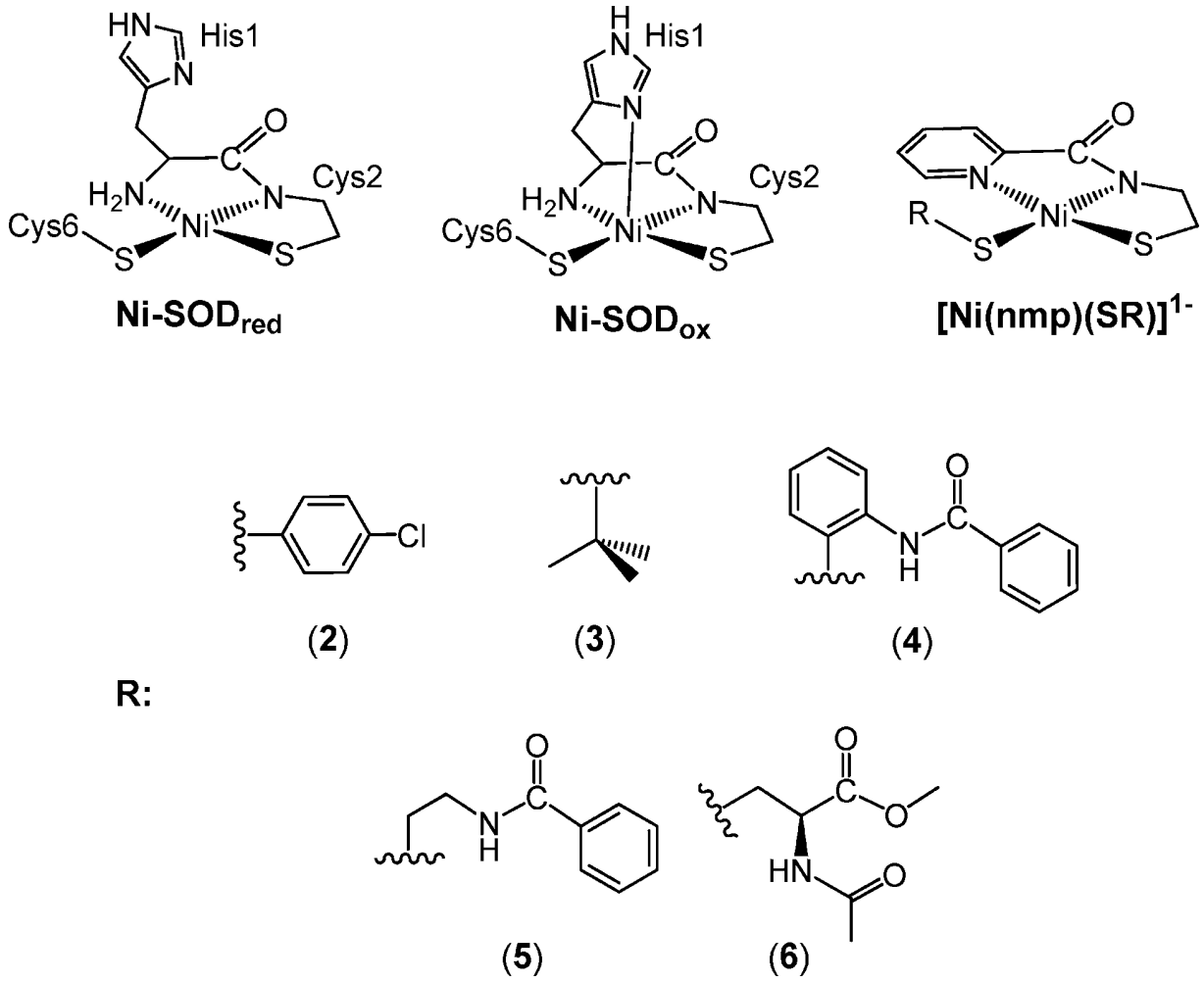

Figure 3.1: Chart 1. (Top): Active Site of Ni-SOD$_{\text{red}}$ (left), Ni-SOD$_{\text{ox}}$ (middle) and Ni-SOD model systems described in the present work, $[\text{Ni(nmp)(SR)}]^{-}$ (right). (Bottom): R groups used in this study [RSH = HSC_6H_4-p-Cl (2), HS^tBu **(3)**, o-benzoylaminobenzene thiol **(4)**, N-(2-mercaptoethyl)benzamide **(5)** and N-acetyl-L-cysteine methyl ester (6)].

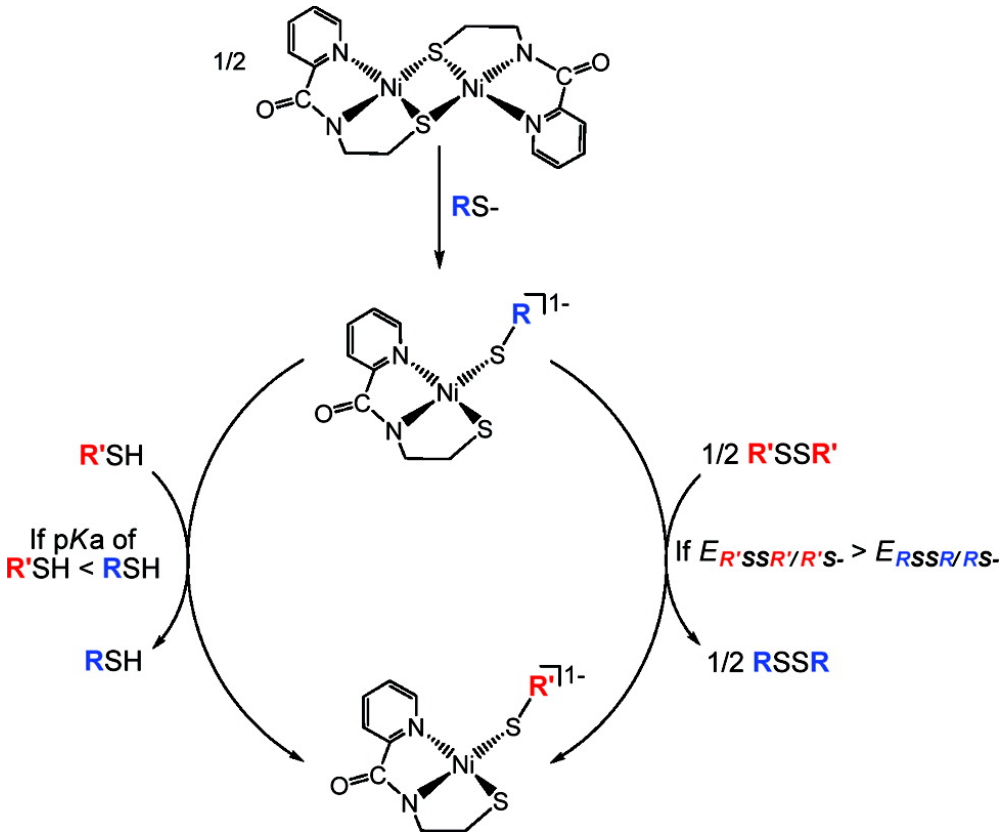

Figure 3.2: Synthetic protocols by which complexes of general formula $[Ni(nmp)(SR)]^-$ were obtained.

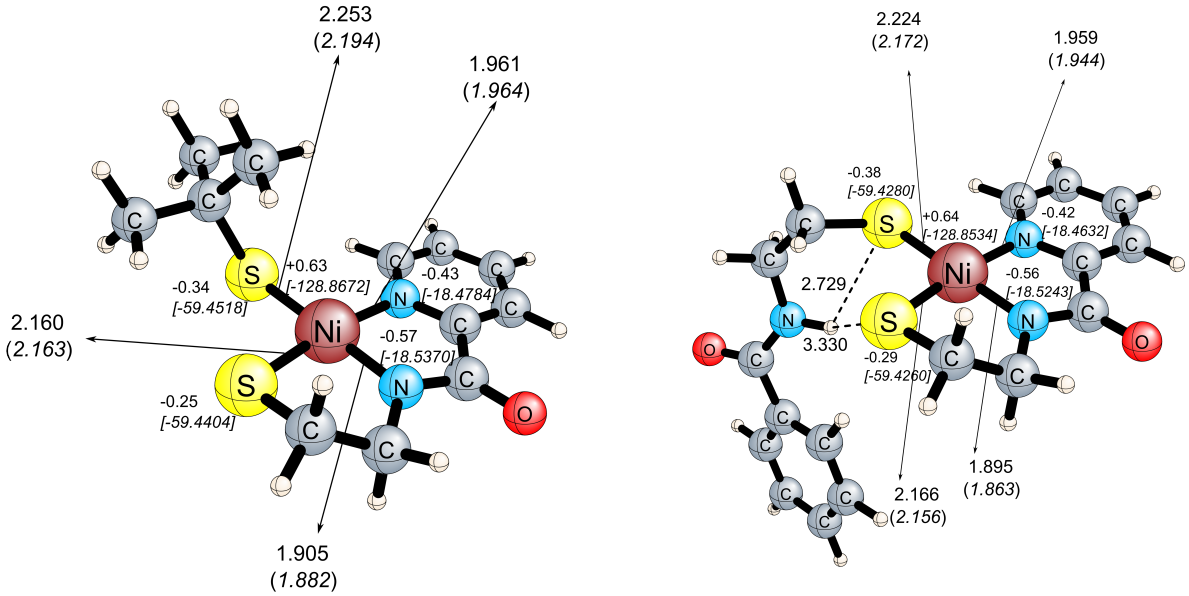

Figure 3.3: Geometry optimized structures of complexes **3** (left) and **5** (right) featuring relevant bond distances (crystallographically-determined distances shown in parentheses), NBO atomic charges and electrostatic potentials at relevant nuclei [in a.u. shown in brackets].

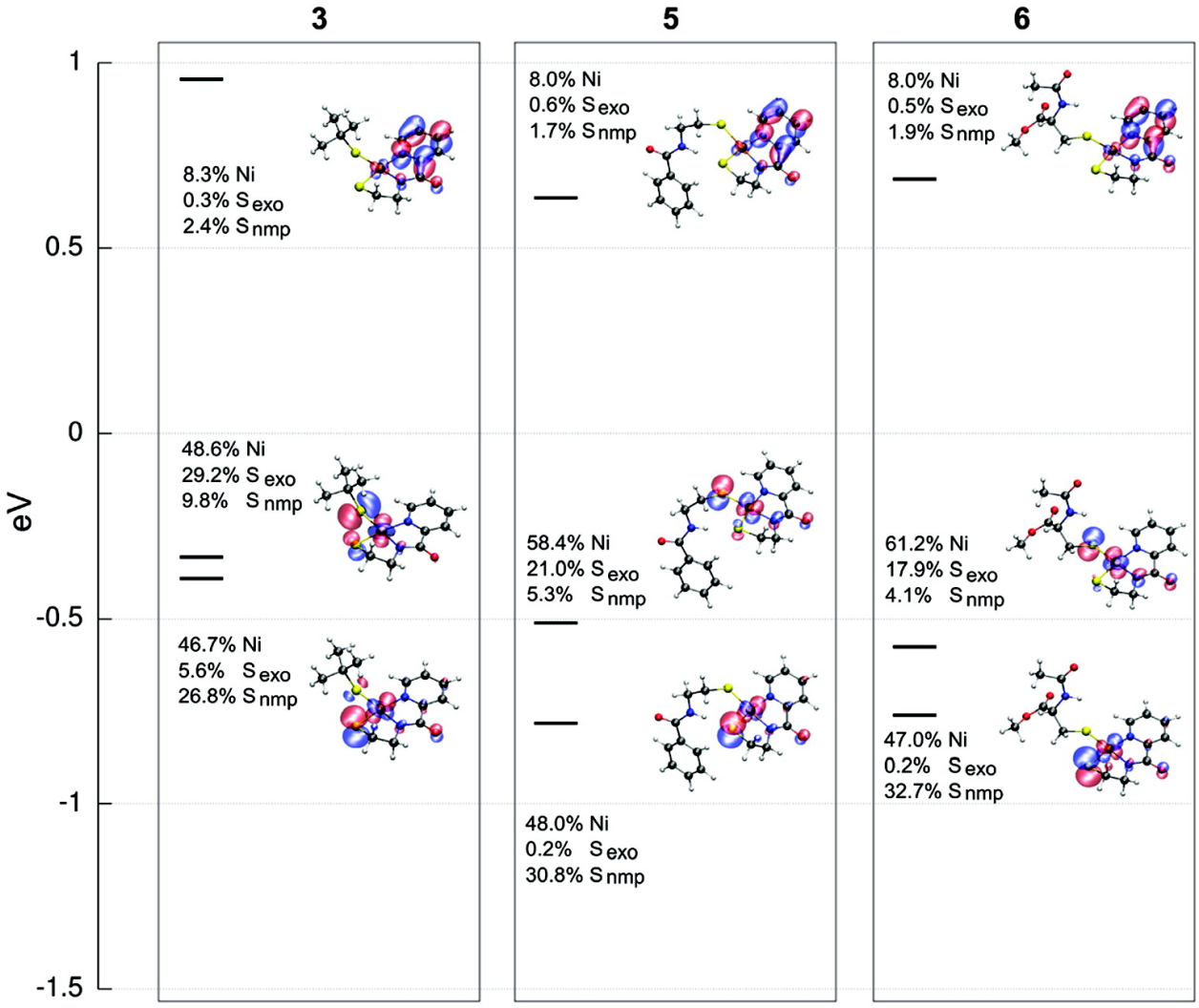

Figure 3.4: DFT generated isosurface plots of the frontier MOs of the geometry optimized structures of the alkyl S_{exo} complexes **3**, **5** and **6**. In each column, the orbitals descend in the order LUMO, HOMO, and HOMO-1.

Table 3.1: Relevant bond lengths (Å), bond angles (deg), atomic charges and electrostatic potentials (ESPs) (a.u.) of DFT geometry optimized structures of complexes **2**-**6**.

	2	**3**	**4**	**5**	**6**
Ni-N_{am}	1.891	1.905	1.891	1.895	1.897
Ni-N_{py}	1.955	1.961	1.955	1.959	1.960
Ni-S_{nmp}	2.156	2.160	2.156	2.166	2.167
Ni-S_{exo}	2.239	2.253	2.253	2.224	2.228
$N_{pep}\cdots S_{exo}$			2.935	3.209	3.106
N_{pep}-H			1.022	1.012	1.018
N-$H_{pep}\cdots$Sexo			2.271	2.729	2.533
N_{am}-Ni-N_{py}	82.7	82.3	82.8	82.7	82.6
N_{am}-Ni-S_{nmp}	88.7	88.4	88.5	87.9	87.7
N_{am}-Ni-S_{exo}	173.9	178.3	175.2	175.2	176.4
N_{py}-Ni-S_{nmp}	170.7	170.6	171.2	170.3	170.2
N_{py}-Ni-S_{exo}	98.6	97.0	97.9	93.5	94.3
S_{nmp}-Ni-S_{exo}	90.3	92.3	90.9	96.1	95.4
Ni-S_{nmp}-Cα	98.1	97.8	98.0	98.2	97.8
Ni-S_{exo}-Cα	111.9	113.5	112.1	117.4	113.1
N-$H_{pep}\cdots S_{exo}$			121.3	109.4	115.2
Atomic Charge N_{am}	−0.56	−0.57	−0.56	−0.56	−0.56
Atomic Charge N_{py}	−0.43	−0.43	−0.43	−0.42	−0.42
Atomic Charge S_{nmp}	−0.23	−0.25	−0.24	−0.29	−0.28
Atomic Charge S_{exo}	−0.18	−0.34	−0.26	−0.38	−0.35
Atomic Charge Ni	0.62	0.63	0.63	0.64	0.64
ESP S_{nmp} (a.u.)	−59.4286	−59.4404	−59.4237	−59.4260	−59.4277
ESP S_{exo} (a.u.)	−59.4201	−59.4518	−59.4114	−59.4280	−59.4245

Table 3.2: Löwdin Orbital Compositions Derived from the DFT Calculations for Selected Molecular Orbitals of Complex **3**.

MO label	MO	E (eV)	%Ni[a]	%N[b]	%S[c]	Orbital Composition
LUMO[d]	86	0.95	8.3	18.8	2.7	$Ni(d_{xz})$ – $N_{py}(p_z)$, $N_{am}(p_z)$
HOMO	85	−0.34	48.6	1.9	39.0	$Ni(d_{yz})/Ni(d_{xz})$ – $S_{exo}(p_x)$, $S_{nmp}(p_z)$
HOMO-1	84	−0.40	46.7	2.7	32.4	$Ni(d_{xz})/Ni(d_{yz})$ – $S_{nmp}(p_z)$
HOMO-2	83	−0.59	88.7	2.7	3.6	$Ni(d_{z^2})$
HOMO-3	82	−0.68	54.0	5.4	26.7	$Ni(d_{yz})/Ni(d_{xy})$ – $N_{am}(p_z)$, $S_{exo}(p_x)$
HOMO-4	81	−1.58	32.8	4.9	38.2	$Ni(d_{xz})$, $N_{am}(p_y)/N_{am}(p_z)$, $S_{nmp}(p_z)/S_{nmp}(p_y)$, $S_{exo}(p_y)/S_{exo}(p_z)/S_{exo}(p_x)$
HOMO-5	80	−1.73	32.7	3.7	30.6	$Ni(d_{xy})$ + $N_{am}(p_y)/N_{am}(p_x)$, $S_{exo}(p_x)/S_{exo}(p_z)$
HOMO-6	79	−1.90	30.4	9.2	13.9	$Ni(d_{xy})/Ni(d_{yz})$ + $N_{am}(p_z)/N_{am}(p_x)$, $S_{nmp}(p_z)/S_{nmp}(p_y)$

[a]MO contribution from the Ni AOs. [b]MO contribution from the N AOs of N_{py} and the coordinated $N_{carboxamide}$. [c]MO contribution from the S AOs. The composition is given in order of AO contribution to the MO. [d]The major contributions to the LUMO involves C(pπ) AOs from the pyridine ring of nmp (56.2%). Bonding interactions are represented with a + and antibonding interactions are denoted with a −. The coordinate system used for figuring out the type of AO on Ni, N and S are as follows: z-axis is normal to the square planar ligand field; x-axis is parallel to S_{nmp}–Ni–N_{py}; y-axis is parallel to S_{exo}–Ni–$N_{carboxamide}$.

Table 3.3: Löwdin Orbital Compositions Derived from the DFT Calculations for Selected Molecular Orbitals of Complex **5**.

MO label	MO	E (eV)	%Ni[a]	%N[b]	%S[c]	Orbital Composition
LUMO[d]	109	0.64	8.0	19.4	2.3	$Ni(d_{xz}) - N_{py}(p_z)$, $N_{am}(p_z)$
HOMO	108	-0.51	58.4	3.4	26.3	$Ni(d_{yz}) - N_{am}(p_z) - S_{exo}(p_z)$
HOMO-1	107	-0.78	48.0	2.6	31.0	$Ni(d_{xz}) - S_{nmp}(p_z)$
HOMO-2	106	-0.93	93.5	1.7	3.1	$Ni(d_{z^2})$
HOMO-3	105	-1.66	48.8	6.5	25.3	$Ni(d_{xy})/Ni(d_{xz})$, $N_{am}(p_z)$, $S_{exo}(p_z)/S_{exo}(p_x)$
HOMO-4	104	-1.85	29.9	8.4	35.8	$Ni(d_{xy})/Ni(d_{xz})$, $N_{am}(p_z)/N_{am}(p_y)$, $S_{exo}(p_z)$
HOMO-5	103	-2.10	20.4	5.4	19.5	$Ni(d_{xy})/Ni(d_{xz})$, $N_{am}(p_x)/N_{am}(p_y)/N_{am}(p_z)$, $S_{nmp}(p_z)/S_{nmp}(p_y)$
HOMO-6	102	-2.30	34.3	1.1	42.4	$Ni(d_{xz})/Ni(d_{yz})/Ni(d_{x^2-y^2}) + S_{nmp}(p_z)$, $S_{exo}(p_z)$

[a]MO contribution from the Ni AOs. [b]MO contribution from the N AOs of N_{py} and the coordinated $N_{carboxamide}$. [c]MO contribution from the S AOs. The composition is given in order of AO contribution to the MO. [d]The major contributions to the LUMO involves C($p\pi$) AOs from the pyridine ring of nmp (56.9%). Bonding interactions are represented with a + and antibonding interactions are denoted with a –. The coordinate system used for figuring out the type of AO on Ni, N and S are as follows: z-axis is normal to the square planar ligand field; x-axis is parallel to S_{nmp}–Ni–N_{py}; y-axis is parallel to S_{exo}–Ni–$N_{carboxamide}$.

Table 3.4: Löwdin Orbital Compositions Derived from the DFT Calculations for Selected Molecular Orbitals of Complex **6**.

MO label	MO	E (eV)	%Ni[a]	%N[b]	%S[c]	Orbital Composition
LUMO[d]	108	0.69	8.0	19.6	2.4	Ni(dxz) – Npy(pz), Nam(pz)
HOMO	107	-0.57	61.2	4.0	22.0	Ni(dyz) – Nam(pz) – Sexo(pz)
HOMO-1	106	-0.75	47.0	2.5	32.9	Ni(dxz), Nam(pz), Snmp(pz)
HOMO-2	105	-0.91	93.2	1.6	3.5	Ni(dz2)
HOMO-3	104	-1.62	50.3	6.1	25.1	Ni(dxy), Nam(pz), Sexo(pz)/Sexo(px)
HOMO-4	103	-1.93	23.1	8.6	31.1	Ni(dxy)/Ni(dxz), Nam(pz)/Nam(py), Sexo(pz)/Sexo(py)
HOMO-5	102	-2.09	24.7	5.6	33.5	Ni(dxy)/Ni(dxz), Nam(pz)/Nam(px), Snmp(pz)/Snmp(py), Sexo(pz)
HOMO-6	101	-2.22	34.3	2.6	29.4	Ni(dxz)/Ni(dxy)/Ni(yz), Nam(pz)/Nam(py)/Nam(px), Snmp(pz)

[a]MO contribution from the Ni AOs. [b]MO contribution from the N AOs of N_{py} and the coordinated $N_{carboxamide}$. [c]MO contribution from the S AOs. The composition is given in order of AO contribution to the MO. [d]The major contributions to the LUMO involves C(pπ) AOs from the pyridine ring of nmp (56.7%). Bonding interactions are represented with a + and antibonding interactions are denoted with a –. The coordinate system used for figuring out the type of AO on Ni, N and S are as follows: z-axis is normal to the square planar ligand field; x-axis is parallel to S_{nmp}–Ni–N_{py}; y-axis is parallel to S_{exo}–Ni–$_{Ncarboxamide}$.

References

(1) Beyer, W.; Imlay, J.; Fridovich, I. *Prog. Nucleic Acid Res. Mol. Biol.* **1991**, *40*, 221–253.

(2) Maritim, A.; Sanders, R.; Watkins, J. *J. Biochem. Mol. Toxicol.* **2003**, *17*, 24–38.

(3) Valentine, J.; Wertz, D.; Lyons, T.; Liou, L.; Goto, J.; Gralla, E. *Curr. Opin. Chem. Biol.* **1998**, *2*, 253–262.

(4) Riley, D. *Chem. Rev.* **1999**, *99*, 2573–2587.

(5) Kumar, B.; Koul, S.; Khandrika, L.; Meacham, R. B.; Koul, H. K. *Cancer Res.* **2008**, *68*, 1777–1785.

(6) Ishikawa, K.; Takenaga, K.; Akimoto, M.; Koshikawa, N.; Yamaguchi, A.; Imanishi, H.; Nakada, K.; Honma, Y.; Hayashi, J.-I. *Science* **2008**, *320*, 661–664.

(7) De Leo, M.; Borrello, S.; Passantino, M.; Palazzotti, B.; Mordente, A.; Daniele, A.; Filippini, V.; Galeotti, T.; Masullo, C. *Neurosci. Lett.* **1998**, *250*, 173–176.

(8) Kocatürk, P.; Akbostanci, M.; Tan, F.; Kavan, G. *Pathophysiology* **2000**, *7*, 63.

(9) Fortunato, G.; Pastinese, A.; Intrieri, M.; Lofrano, M.; Gaeta, G.; Censi, M.; Boccalatte, A.; Salvatore, F.; Sacchetti, L. *Clin. Biochem.* **1997**, *30*, 569–571.

(10) Miller, A. *Curr. Opin. Chem. Biol.* **2004**, *8*, 162–168.

(11) Borgstahl, G.; Parg, H.; Hickey, M.; Beyer, W.; Hallewell, R.; Tainer, J. *Cell* **1992**, *71*, 107–118.

(12) Miller, A.-F. *Acc. Chem. Res.* **2008**, *41*, 501–510.

(13) Tierney, D.; Fee, J.; Ludwig, M.; Pennerhahn, J. *Biochemistry* **1995**, *34*, 1661–1668.

(14) Tainer, J.; Getzoff, E.; Richardson, J.; Richardson, D. *Nature* **1983**, *306*, 284–287.

(15) Barondeau, D.; Kassmann, C.; Bruns, C.; Tainer, J.; Getzoff, E. *Biochemistry* **2004**, *43*, 8038–8047.

(16) Wuerges, J.; Lee, J.; Yim, Y.; Yim, H.; Kang, S.; Carugo, K. *Proc. Natl. Acad. Sci. U.S.A* **2004**, *101*, 8569–8574.

(17) Youn, H.; Kim, E.; Roe, J.; Hah, Y.; Kang, S. *Biochem. J.* **1996**, *318*, 889–896.

(18) Youn, H.; Youn, H.; Lee, J.; Yim, Y.; Lee, J.; Hah, Y.; Kang, S. *Arch. Biochem. Biophys.* **1996**, *334*, 341–348.

(19) Lanzilotta, W.; Schuller, D.; Thorsteinsson, M.; Kerby, R.; Roberts, G.; Poulos, T. *Nat. Struct. Biol.* **2000**, *7*, 876–880.

(20) Harrop, T.; Olmstead, M.; Mascharak, P. *Inorg. Chem.* **2006**, *45*, 3424–3436.

(21) Lindahl, P. *Biochemistry* **2002**, *41*, 2097–2105.

(22) Volbeda, A.; FontecillaCamps, J.; Frey, M. *Curr. Opin. Struct. Biol.* **1996**, *6*, 804–812.

(23) Kruger, H.; Peng, G.; Holm, R. *Inorg. Chem.* **1991**, *30*, 734–742.

(24) Herbst, R. W.; Guce, A.; Bryngelson, P. A.; Higgins, K. A.; Ryan, K. C.; Cabelli, D. E.; Garman, S. C.; Maroney, M. J. *Biochemistry* **2009**, *48*, 3354–3369.

(25) Mullins, C.; Grapperhaus, C.; Kozlowski, P. *J. Biol. Inorg. Chem.* **2006**, *11*, 617–625.

(26) Volbeda, A.; Garcin, E.; Piras, C.; deLacey, A.; Fernandez, V.; Hatchikian, E.; Frey, M.; FontecillaCamps, J. *J. Am. Chem. Soc.* **1996**, *118*, 12989–12996.

(27) Grapperhaus, C.; Darensbourg, M. *Acc. Chem. Res.* **1998**, *31*, 451–459.

(28) Grapperhaus, C.; Mullins, C.; Kozlowski, P.; Mashuta, M. *Inorg. Chem.* **2004**, *43*, 2859–2866.

(29) Fiedler, A. T.; Brunold, T. C. *Inorg. Chem.* **2007**, *46*, 8511–8523.

(30) Fiedler, A.; Bryngelson, P.; Maroney, M.; Brunold, T. *J. Am. Chem. Soc.* **2005**, *127*, 5449–5462.

(31) Jenkins, R. M.; Singleton, M. L.; Almaraz, E.; Relbenspies, J. H.; Darensbourg, M. Y. *Inorg. Chem.* **2009**, *48*, 7280–7293.

(32) Neupane, K. P.; Gearty, K.; Francis, A.; Shearer, J. *J. Am. Chem. Soc.* **2007**, *129*, 14605–14618.

(33) Neupane, K. P.; Shearer, J. *Inorg. Chem.* **2006**, *45*, 10552–10566.

(34) Shearer, J.; Dehestani, A.; Abanda, F. *Inorg. Chem.* **2008**, *47*, 2649–2660.

(35) Shearer, J.; Long, L. *Inorg. Chem.* **2006**, *45*, 2358–2360.

(36) Shearer, J.; Neupane, K. P.; Callan, P. E. *Inorg. Chem.* **2009**, *48*, 10560–10571.

(37) Shearer, J.; Zhao, N. *Inorg. Chem.* **2006**, *45*, 9637–9639.

(38) Pelmenschikov, V.; Siegbahn, P. *J. Am. Chem. Soc.* **2006**, *128*, 7466–7475.

(39) Lee, H.-I.; Lee, J.-W.; Yang, T.-C.; Kang, S.-O.; Hoffman, B. M. *J. Biol. Inorg. Chem.* **2010**, *15*, 175–182.

(40) Ryan, K. C.; Johnson, O. E.; Cabelli, D. E.; Brunold, T. C.; Maroney, M. J. *J. Biol. Inorg. Chem.* **2010**, *15*, 795–807.

(41) Johnson, O. E.; Ryan, K. C.; Maroney, M. J.; Brunold, T. C. *J. Biol. Inorg. Chem.* **2010**, *15*, 777–793.

(42) Tietze, D.; Breitzke, H.; Imhof, D.; Kothe, E.; Weston, J.; Buntkowsky, G. *Chem. - Eur. J.* **2009**, *15*, 517–523.

(43) Krause, M. E.; Glass, A. M.; Jackson, T. A.; Laurence, J. S. *Inorg. Chem.* **2010**, *49*, 362–364.

(44) Schmidt, M.; Zahn, S.; Carella, M.; Ohlenschlaeger, O.; Goerlach, M.; Kothe, E.; Weston, J. *ChemBioChem* **2008**, *9*, 2135–2146.

(45) Tabbí, G.; Driessen, W.; Reedijk, J.; Bonomo, R.; Veldman, N.; Spek, A. *Inorg. Chem.* **1997**, *36*, 1168–1175.

(46) Mullins, C. S.; Grapperhaus, C. A.; Frye, B. C.; Wood, L. H.; Hay, A. J.; Buchanan, R. M.; Mashuta, M. S. *Inorg. Chem.* **2009**, *48*, 9974–9976.

(47) Jenkins, R. M.; Singleton, M. L.; Leamer, L. A.; Reibenspies, J. H.; Darensbourg, M. Y. *Inorg. Chem.* **2010**, *49*, 5503–5514.

(48) Ma, H.; Chattopadhyay, S.; Petersen, J. L.; Jensen, M. P. *Inorg. Chem.* **2008**, *47*, 7966–7968.

(49) Ma, H.; Wang, G.; Yee, G. T.; Petersen, J. L.; Jensen, M. P. *Inorg. Chim. Acta* **2009**, *362*, 4563–4569.

(50) Mathrubootham, V.; Thomas, J.; Staples, R.; McCraken, J.; Shearer, J.; Hegg, E. L. *Inorg. Chem.* **2010**, *49*, 5393–5406.

(51) Gale, E. M.; Patra, A. K.; Harrop, T. C. *Inorg. Chem.* **2009**, *48*, 5620–5622.

(52) Szilagyi, R.; Bryngelson, P.; Maroney, M.; Hedman, B.; Hodgson, K.; Solomon, E. *J. Am. Chem. Soc.* **2004**, *126*, 3018–3019.

(53) Prabhakar, R.; Morokuma, K.; Musaev, D. G. *J. Comput. Chem.* **2006**, *27*, 1438–1445.

(54) Dey, A.; Jenney, F. E., Jr.; Adams, M. W. W.; Johnson, M. K.; Hodgson, K. O.; Hedman, B.; Solomon, E. I. *J. Am. Chem. Soc.* **2007**, *129*, 12418–12431.

(55) Dey, A.; Okamura, T.; Ueyama, N.; Hedman, B.; Hodgson, K.; Solomon, E. *J. Am. Chem. Soc.* **2005**, *127*, 12046–12053.

(56) Maynard, A.; Covell, D. *J. Am. Chem. Soc.* **2001**, *123*, 1047–1058.

(57) Ueyama, N.; Yamada, Y.; Okamura, T.; Kimura, S.; Nakamura, A. *Inorg. Chem.* **1996**, *35*, 6473–6484.

(58) Cohen, A.; Handy, N. *Mol. Phys.* **2001**, *99*, 607–615.

(59) Lee, C.; Yang, W.; Parr, R. *Phys. Rev. B* **1988**, *37*, 785–789.

(60) Weigend, F.; Ahlrichs, R. *Phys. Chem. Chem. Phys.* **2005**, *7*, 3297–3305.

(61) Shao, Y. et al. *Phys. Chem. Chem. Phys.* **2006**, *8*, 3172–3191.

(62) Li, Y.; Zamble, D. B. *Chem. Rev.* **2009**, *109*, 4617–4643.

(63) Neese, F. ORCA - an ab initio, Density Functional and Semiempirical Program Package, version 2.7; University of Bonn: Bonn, Germany, 2009.

(64) Dey, A.; Green, K. N.; Jenkins, R. M.; Jeffrey, S. P.; Darensbourg, M.; Hodgson, K. O.; Hedman, B.; Solomon, E. I. *Inorg. Chem.* **2007**, *46*, 9655–9660.

(65) Bobadova-Parvanova, P.; Galabov, B. *J. Phys. Chem. A* **1998**, *102*, 1815–1819.

(66) Galabov, B.; Bobadova-Parvanova, P. *J. Phys. Chem. A* **1999**, *103*, 6793–6799.

(67) Perdew, J.; Levy, M. *Phys. Rev. B* **1997**, *56*, 16021–16028.

(68) Bryngelson, P.; Arobo, S.; Pinkham, J.; Cabelli, D.; Maroney, M. *J. Am. Chem. Soc.* **2004**, *126*, 460–461.

Chapter 4

Investigating the Effects of Basis Set on Metal-Metal and Metal-Ligand Bond Distances in Stable Transition Metal Carbonyls: Performance of Correlation Consistent Basis Sets with 35 Density Functionals*

*Narendrapurapu, B. S.; Richardson, N. A.; Copan, A. V.; Estep, M. L.; Yang, Z.; Schaefer, H. F., III, Submitted to *J. Chem. Theory Comput.*, 02/19/2013.

4.1 Abstract

Density functional theory (DFT) is a widely used method for predicting equilibrium geometries of organometallic compounds involving transition metals, with a wide choice of functional and basis set combinations. A study of the role of basis set size in predicting the structural parameters can be insightful with respect to the effectiveness of using small basis sets to optimize larger molecular systems. In this study, we compare the equilibrium metal-ligand and metal-metal distances of six transition metal carbonyl compounds predicted by the Hood-Pitzer double-ζ polarization (DZP) basis set, against those predicted employing the standard correlation consistent cc-pVXZ (X=D,T,Q) basis sets, for 35 different DFT methods. The effects of systematically increasing the basis set size on the structural parameters are carefully investigated. Our results show that, in general, DZP basis sets predict structural parameters with an accuracy comparable to the triple and quadruple-ζ basis sets. The Mn-Mn bond distance in $Mn_2(CO)_{10}$ shows a greater dependence on basis set size compared to the other M-M bonds. However, the DZP predictions for r_e(Mn-Mn) are closer to experiment than those obtained with the much larger cc-pVQZ basis set. Overall, the DZP M06-L method predicts structures that are very consistent with experiment.

4.2 Introduction

Density Functional Theory (DFT) has become a method of choice for predicting the molecular properties of large molecular systems, especially those that contain transition metals.[1] Systems that contain transition metal atoms often exhibit degenerate or near degenerate electronic states, rendering it challenging to systematically include large amount of multi-reference character in wavefunction based methods. Apart from this, DFT competes well in accuracy, for most systems, with simple wavefunction based methods. The

cost-effectiveness of DFT renders it a very practical method for computing the properties of very large systems. In the past few decades, the equilibrium geometries of many transition metal organometallic compounds and metal clusters have been obtained using DFT. In cases where crystallographic information is not yet available, DFT structures are typically the only ones known. The DFT computed structures and vibrational frequencies of a number of homoleptic binuclear metal carbonyl compounds have been reported in the past.[2] The metal-metal and metal-carbon bond distances in these compounds were often computed using standard double zeta plus polarization (DZP) basis sets. A critical structural feature of the binuclear transition metal compounds is the metal-metal bond, especially multiple bonds in case of unsaturated metal carbonyls. Though not infallible, the metal-metal bond distance is an indicator for direct metal-metal interactions in these compounds.

DFT offers a wide choice of functional and basis set combinations for modeling the structures of organometallic compounds involving metal-metal bonds. Functionals that are calibrated for main group elements are to be used with caution for transition metal compounds. Recent studies have focussed on benchmarking functionals that are suitable for computing various transition metal properties. In regard to metal-metal and metal-ligand bond lengths, Zhao and Truhlar examined the performance of 57 functionals with double and triple-ζ basis sets and suggested G96LYP, MPWLYP1M, XLYP, BLYP, MOHLYP and mPWLYP as functionals of best choice.[3,4] In their 2003 assessment of the role of basis sets in density functional theory, Handy *et. al.* suggested that basis sets of triple-zeta quality are preferable over basis sets of double zeta quality.[5] Previous studies have suggested that Dunning basis sets are not an optimal choice for density functional computations,[6] yet there are many studies which use Dunning basis sets in literature. In relation to the behavior of correlation consistent basis sets in DFT, Wilson and co-workers tested six commonly used functionals with cc-pVxZ (x= D, T, Q, 5) basis sets to predict the molecular properties of first-row closed shell molecules and observed a convergence in molecular properties

with increasing basis set size.[7] In another related study, Cundari, Wilson and coworkers indicated increased accuracies for enthalpies of formation for transition metal carbonyls upon increasing the basis set size from cc-pVTZ to cc-pVQZ for generalized gradient exchange (GGE), hybrid GGA (HGGA) and hybrid meta-GGA (HMGGA) functionals.[8]

In this study, we have performed full geometry optimizations on six transition metal carbonyl compounds, three of which are bimetallic. We studied the changes in metal-metal (M-M) and metal-carbon bond parameter with increasing basis set size from double to triple and quadruple-ζ basis sets and for 35 different density functionals.

4.3 Methods

Four basis sets were chosen for this study. The first is an extension of the Dunning double-ζ plus polarization (DZP) basis, and the others are the standard Dunning correlation consistent cc-pVXZ (X = D, T, Q) basis sets.[9–11] The Dunning's DZP basis sets for C and O have one set of pure spherical harmonic d-functions with orbital components α_d(C) = 0.75 and α_d(O) =0.85 in addition to Dunning's standard double-ζ (DZ) contraction[12] of Huzinaga's primitive sets[13] and are designated (9s5p1d/4s2p1d). The extended DZP basis sets for transition metals, designated (14s11p6d/10s8p3d), are constructed from Watcher's primitive sets[14] augmented by two sets of p functions and one set of d functions and contracted following Hood and Pitzer.[15]

Geometries of all the six transition metal carbonyls were optimized using the NWChem6.1 package.[16] The dependence of metal-metal bond distances on basis set was tested for 35 functionals: five generalized gradient approximation (GGA) functionals, two meta GGA functionals, seveteen hybrid GGA functionals, nine hybrid meta GGAs, and two long-range correlated hybrid meta GGAs. Since the M05-2X method and the M06 suite of functionals are sensitive to the choice of quadrature grid, the NWChem fine integration grid with (140,

974) points for the five 3d transition metals and (70, 590) points for C and O, was chosen.[17] The grid employs the Mura-Knowles radial quadrature and Lebedev angular quadrature and was used for all DFT methods. All geometries were optimized employing the NWChem 'tight' convergence option with an SCF convergence of 10^{-8}.

4.4 Results and Discussion

Metal-carbon (M-C) and metal-metal (M-M) bond distances for the six carbonyl compounds, computed by the 35 functionals using the four basis sets, are reported in Tables 1-6 and compared with the available experimental structures. The Tables consist of functionals grouped according to their type and arranged in decreasing order of the Hartree Fock contribution to the DFT method within each group, wherever applicable. The functionals we have chosen in this study predict geometries that are reasonably close to the experimental structures. We have computed the mean absolute deviation (MAD) of each bond length by averaging over the absolute deviations (from experimental values) of bond lengths obtained from the four basis sets. For all molecules other than $Mn_2(CO)_{10}$, fewer than five functionals yield M-M and M-C bond distances with MADs greater than 0.05 Å(see Tables C1a - C6a in appendix C). Almost all the functionals predict M-C bond distances with greater consistency than M-M bond lengths. Overall, the M06-L functional performs the best in predicting molecular geometries, with the exception of the bond between Co and the bridging carbon which is overestimated by $\sim$0.022 Å compared to the experimental bond distance.[18] The primary focus of our study is to investigate the role of increasing basis set size on the convergence of structural parameters. Tables 1 - 6 compare optimized bond parameters across the four basis sets for various DFT functionals. We have also provided Tables to compare the predicted structures with experiment (see Tables C1a - C6a). Also reported are comparisons of bond distances from cc-pVXZ (X= D,T,Q) basis sets to the DZP results

(see Tables C1b - C6b in the supplementary material).

A. $Ni(CO)_4$: Solid state and gaseous state structures of the well-known tetrahedral $Ni(CO)_4$ molecule have been determined in the past by X-ray diffraction[19,20] and electron diffraction (ED) experiments.[21] The geometry of $NiCO)_4$ was previously optimized by a number of DFT methods which determined the bond parameters with reasonable accuracy.[22–24] 4.1 shows the variation of M-C bond lengths with increasing basis set size. The computed bond lengths are in good agreement with the experimental values. All four basis sets predict similar structural parameters with differences in M-C bond lengths ranging from lower than 0.001 Å to 0.007 Å across the basis sets. Increasing the size of correlation consistent basis sets from the double-ζ to the triple- and quadruple-ζ has no significant effect on the of M-C bonds distances; the differences are as small as 0.002 Å. The bond lengths increase slightly, with a mean value of 0.003 Å, from DZP to cc-pVDZ basis and contract by about the same amount upon approaching cc-pVQZ basis.

B. $Fe(CO)_5$: $Fe(CO)_5$ is a trigonal bipyramidal molecule with D_{3h} symmetry and two different M-C distances representing the axial (Fe-C^{ax}) and equatorial (Fe-C^{eq}) bonds. There is some experimental uncertainty regarding the relative lengths of the axial and equatorial Fe-C bonds. Gas phase electron diffraction studies[20,25–30] predict shorter Fe-C^{ax} bonds compared to Fe-C^{eq}, whereas the X-ray diffraction study of the crystal[20] suggest an opposite trend. Theoretical studies, both ab initio[31–33] and DFT[32–36] gave divided results about the relative axial and equatorial Fe-C bond distances. Fe-C distances obtained from the density functional methods employed in this study are well within 0.05 Å of the gas electron diffraction experiment.[29] Except for the pure GGA functionals and the M05 hybrid meta GGA, all functionals employed in our study predict slightly longer axial than equatorial bonds. The axial bonds are shorter than the equatorial bonds by ∼0.003 Å in the case of pure GGAs and the M05 functional. The Fe-C^{ax} bonds are longer than the Fe-C^{eq} by ∼0.008 Å for most hybrid and hybrid meta GGAs, and this trend is consistent with the solid state

experimental results. For methods with more than 40% Hartree-Fock contribution, the axial Fe-C bond lengths are significantly longer than Fe-C equatorial bond lengths (∼0.031 Å and ∼0.012 Å for BHLYP and M06-HF, respectively).

C2b shows the variation of Fe-C^{ax} and Fe-C^{eq} bonds with increasing basis set size. For most of the methods, the correlation consistent basis sets predict slightly longer Fe-C bonds compared to those from the DZP basis set. Fe-C bond lengths converge at the cc-pVTZ basis set and do not seem to differ by any more than 0.001 Å with further increase in basis set size. Both Fe-C^{ax} and Fe-C^{eq} elongate by an average distance of 0.004 Å with increase in basis set size from DZP to cc-pVTZ basis, with the exception of M06-HF functional, where bond distances decrease with increase in basis set size.

C. $Cr(CO)_6$: Structure of the octahedral Cr(CO)6 molecule had been studied theoretically[37–43] by a number of density functional methods and the agreement with experimental results[44–46] has been demonstrated in the past. The Cr-C bond distance is reasonably independent of the basis set size for the functionals considered in this study. In all the mononuclear carbonyl compounds considered in this study, the DZP basis set performs exceptionally well in predicting M-C bond distances on par with the cc-pVQZ basis set results.

D. $Co_2(CO)_8$:

$Co_2(CO)_8$ is a very important highly fluxional molecule. In solution, the dibridged C_{2v} structure (see 4.1) exists in equilibrium with the nonbridged D_{3d} structure, and a D_{2d} nonbridged structure has also been suggested by experiments.[47–50] Out of the three structures, the C_{2v} structure is lowest in energy.[51] In the present study, we have optimized the dibridged structure whose crystal structure is well-known[18,52,53] and is used to compare M-M bond lengths in various theoretical studies.[54–62] The Co-Co and Co-C bond differences are presented in C4b . The B97-2, M06-L and M06 functionals predict Co-Co and the two terminal Co-C bond distances within 0.010 Å of experimental values with all four basis sets,

the differences being least in the case of the DZP basis set. But in the case of the bridging Co-C_b, the M06-L functional overestimates the bond distance by ∼0.022 Å .

The structural parameters between DZP and cc-pVXZ (X=D,T,Q) basis sets differ much more in $Co_2(CO)_8$ than in the mononuclear transition metal carbonyls and the difference is much more pronounced for the M06-HF, M05-2X, M06-2X and BHLYP functionals. The Co-Co bond distances predicted employing the DZP basis set are closer to the cc-pVTZ values compared to the cc-pVDZ and cc-pVQZ values, with differences ranging from 0.015 Å (for M06-2X) to less than 0.001 Å (for M06-L). For most functionals, the difference in DZP and cc-pVTZ results for the Co-Co bond length is between 0.005 and 0.003 Å. The Co-C bond distances are less dependent on the size of the correlation consistent basis sets but differ from DZP values from 0.008 to less than 0.001 Å . In spite of these differences in structural parameters between DZP an cc-pVXZ (X=D,T,Q) basis sets, one must note that the triple and quadruple-ζ quality basis sets do not give any more accurate bond lengths than the DZP basis set, compared to the experimental structures. Most functionals predict bond distances that are 0.02-0.04 Å away from the experimental values, regardless of the size or type of basis set employed.

E. $Fe_2(CO)_9$: The triply bridged structure with D_{3h} symmetry is the experimental structure of the $Fe_2(CO)_9$ dimer (see 4.2). Even though the Fe-Fe bond distance in the dimer is only 2% larger than Fe-Fe bond distance in the bulk metal, theoretical studies[56,63–69] suggest the absence of a direct Fe-Fe bond in the triply bridged $Fe_2(CO)_9$. Jang *et. al.* optimized the geometry of the dimer employing the DZP B3LYP method and determined the lengths of the Fe-Fe, Fe-C and C-O bonds within 0.002, 0.01 and 0.005 Å of experiment.[35,69] Considering the fact that the experimental structures are solid state structures, bond distances in C5b determined for isolated $Fe_2(CO)_9$ molecule are reasonably close to experiment, especially for the BP86, HCTH-147, M06-L, B1LYP, MPW1LYP, X3LYP, B3LYP and M06-2X functionals, which predict Fe-Fe, Fe-C^b and Fe-C^t distances

within 0.008, 0.011and 0.019 Å . Increasing the basis set size from DZP to cc-pVQZ results in changes in bond lengths of less than 0.01 Å. In fact, the cc-pVTZ bond distances are very close to the DZP results; the Fe-Fe and Fe-C bond lengths are lengthened by not more than 0.003 Å upon changing the basis set from DZP to cc-pVTZ for as many as 21 functionals used in this study.

F. $Mn_2(CO)_{10}$: $Mn_2(CO)_{10}$ is a homoleptic binuclear carbonyl compound that was isolated later than the other 3d transition metal carbonyl compounds.[70–72] The molecule has D_{4d} symmetry (see 4.3) with non-bridging carbonyls arranged in a staggered confirmation, and this structure was found to be the global minimum.[73] The structure of $Mn_2(CO)_{10}$ with its undisputed direct Mn-Mn bond has been determined by a number of crystallographic[74–77] and electron diffraction studies.[78] The bond distances determined by various DFT methods in this study differ from the gas phase electron diffraction structures by 0.01 to 0.13 Å. The MPWB1K and BB1K methods give the largest differences in Mn-Mn bond distances, 0.133 to 0.129 Å respectively, from the gas electron diffraction[78] value (2.977 Å). All the functionals correctly reproduce the relative lengths of the axial (Mn-C_{ax}) and equatorial (Mn-C_{eq}) bonds, with smaller absolute deviations from experiment for the Mn-C_{ax} bond distance than Mn-C_{eq}. The Mn-Mn bond length increases by 0.015 to 0.034 Å from double-ζ (DZP) to the triple-ζ basis set. From the triple to the quadruple-ζ basis set, the Mn-Mn distance increases further, by 0.006 to 0.015 Å. This suggests a significant basis set dependence of the Mn-Mn bond distance. Despite this, the DZP basis predictions for r_e(Mn-Mn) are closer to experiment than are the cc-pVQZ results.

With the large basis sets cc-pVTZ and cc-pVQZ, the Mn-Mn bond lengths deviate from the electron diffraction experiment by 0.12 Å (for the BLYP functional) to less than 0.005 Å (for BP86, BHandH, B97-1, B97-2, M06-HF, M05-2X and M06-2X). Mean absolute deviations from the experiment are 0.05 Å for both the cc-pVTZ and cc-pVQZ basis. In contrast to the performance of the M06-HF, M05-2X and M06-2X methods for predicting

other M-M bonds distances, the Fe-Fe bond distances predicted by the three methods are very close to experiment, in fact, closer than those predicted by most of the functionals. The M06-HF, M05-2X and M06-2X methods with the cc-pVQZ basis set predict Fe-Fe distances within 0.003, 0.004 and 0.002 Å , respectively, of experiment.

4.5 Conclusions

Structures of $Ni(CO)_4$, $Fe(CO)_5$, $Cr(CO)_6$, $Co_2(CO)_8$, $Fe_2(CO)_9$ and $Mn_2(CO)_{10}$ have been optimized in this study, employing the double, triple and quadruple-ζ correlation consistent basis sets (cc-pVXZ) and the Hood-Pitzer extended double-ζ polarization (DZP) basis set. Comparison of M-M and M-L bond distances as a function of basis set size for 35 functionals shows that the DZP basis set generally predicts structural parameters on par with the correlation consistent triple and quadruple-ζ basis sets. The Mn-Mn bond distance shows more basis set dependance than the other two M-M bond lengths. Overall, the M06-L method predicts M-M and M-L bond distances in better agreement with experimental values, even with a relatively small basis set like the Hood-Pitzer DZP basis set. The DZP basis set, surprisingly, predicts structural parameters with reasonable accuracy and greatly reduces the computational cost of optimizing the structures of larger systems. In our study, the DZP M06-L method bests the other methods in terms of accuracy and computational cost.

Large basis sets such as cc-pVQZ can be applied to small organometallic systems such as those studied here. However, when one considers large transition metal systems (e.g., 1000 atoms), recently developed linear scaling methods[79] become necessary for *ab initio* computations. For such large systems, the powerful advantages of linear scaling methods are severely compromised when extended basis sets such as cc-pVQZ are employed. Linear scaling methods demand that basis functions be local, and this is not the case with the more diffuse basis functions that exist in the quadruple-ζ sets. Thus the general reliability

of smaller basis sets, such as the Hood-Pitzer sets, is important for the future of quantum chemistry.

Supporting Information Available

Tables C1a - C6a in appendix C compare M-M and M-L bond distances with experiment. Tables C1b - C6b in appendix C compare bond distances from cc-pVXZ (X=D,T,Q) basis sets with DZP results. This information is also available free of charge via the Internet at http://pubs.acs.org

4.6 Acknowledgements

This research was supported by the National Science Foundation (NSF), Grant No. CHE-1054286.

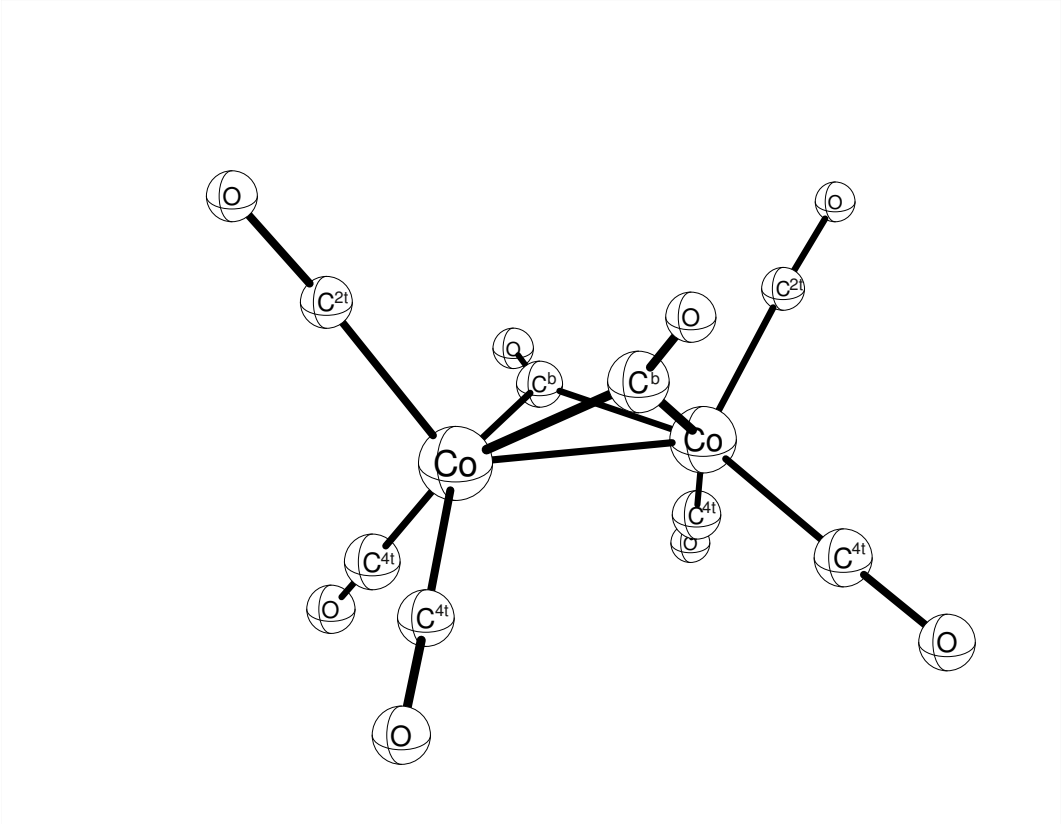

Figure 4.1: $Co_2(CO)_8$ - C_{2v} symmetry

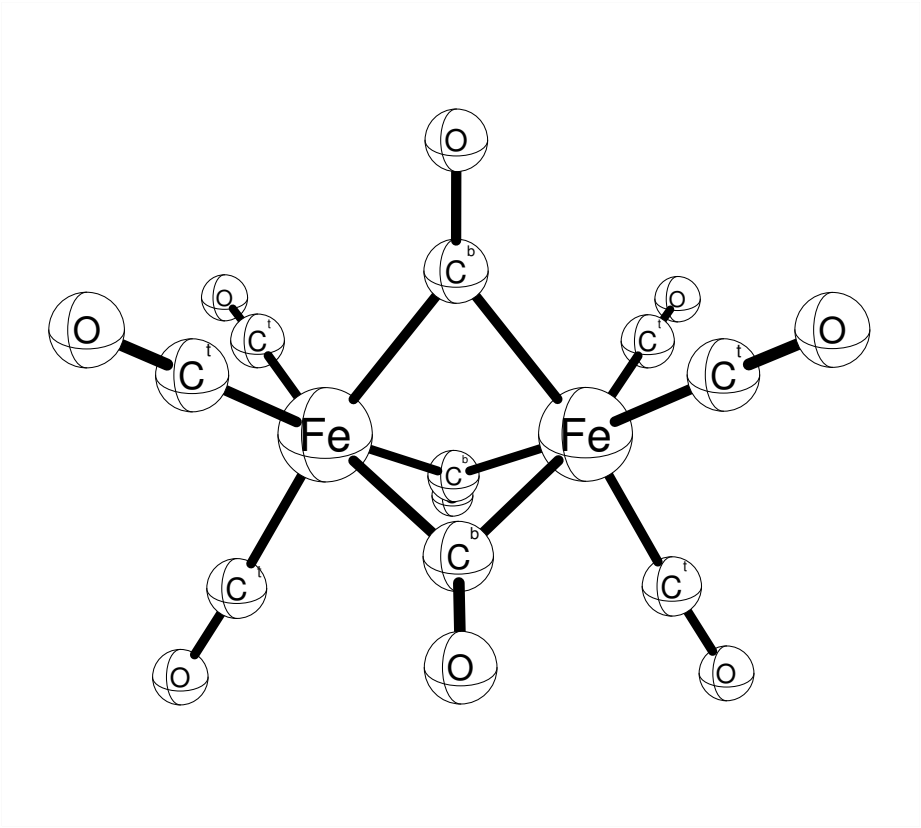

Figure 4.2: $Fe_2(CO)_9$ - D_{3h} symmetry

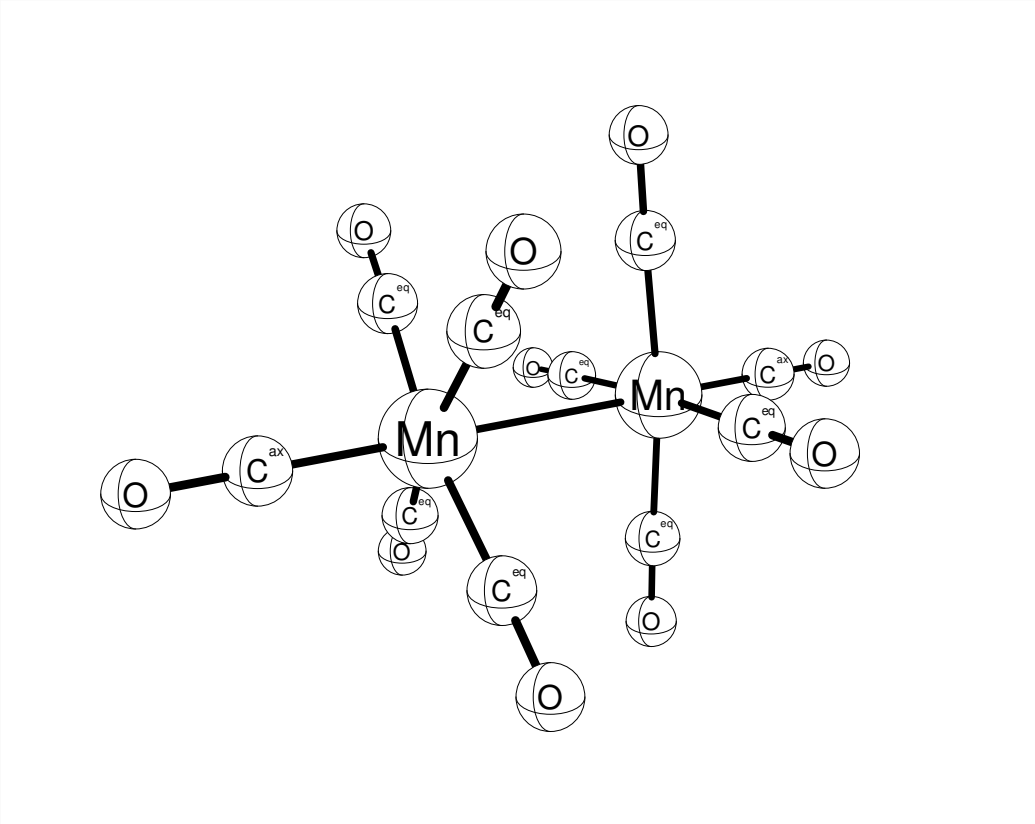

Figure 4.3: $Mn_2(CO)_{10}$ - D_{4d} symmetry

Table 4.1: $Ni(CO)_4$ bond distances in Angstroms

DFT Method	DZP Ni-C	cc-pVDZ Ni-C	cc-pVTZ Ni-C	cc-pVQZ Ni-C
GGA				
BLYP	1.847	1.853	1.853	1.852
BP86	1.826	1.829	1.829	1.827
B97-D	1.843	1.847	1.845	1.845
HCTH147	1.833	1.836	1.834	1.833
HCTH407	1.831	1.833	1.832	1.831
Meta GGA				
M06-L	1.838	1.839	1.836	1.835
VSXC	1.859	1.863	1.861	1.860
Hybrid GGA				
BHLYP	1.848	1.854	1.853	1.852
MPW1K	1.823	1.826	1.825	1.824
BHandH	1.832	1.837	1.836	1.835
MPW1PW91	1.823	1.826	1.824	1.824
MPW1PBE	1.821	1.824	1.822	1.821
B1LYP	1.846	1.851	1.851	1.850
PBE1PBE	1.821	1.824	1.823	1.822
MPW1LYP	1.844	1.850	1.850	1.849
B98	1.837	1.841	1.840	1.839
X3LYP	1.840	1.845	1.845	1.844
B97-1	1.838	1.841	1.841	1.840
B97-2	1.831	1.834	1.833	1.832
MPW3PBE	1.821	1.825	1.824	1.823
B3LYP	1.841	1.846	1.846	1.845
B3PW91	1.824	1.827	1.826	1.825
B3P86	1.820	1.823	1.822	1.821
O3LYP	1.831	1.834	1.833	1.832
Hybrid Meta GGA				
M06-HF	1.929	1.930	1.926	1.928
M05-2X	1.871	1.877	1.876	1.875
M06-2X	1.899	1.906	1.905	1.905
MPWB1K	1.827	1.830	1.829	1.828
BB1K	1.828	1.831	1.830	1.829
M05	1.845	1.850	1.851	1.848
B1B95	1.827	1.830	1.829	1.828
M06	1.844	1.850	1.851	1.849
TPSSH	1.827	1.830	1.828	1.827
LC Hybrid GGA				
CAM-B3LYP	1.831	1.836	1.837	1.836
LC-ωPBE†	1.817	1.819	1.819	1.818
Experiment-1 [a]	1.838	1.838	1.838	1.838
Experiment-2 [b]	1.84	1.84	1.84	1.84
Experiment-3 [c]	1.817	1.817	1.817	1.817

[a] Ref-21, gas ED structure; [b] Ref-19, crystal structure; [c] Ref-20, crystal structure.
† cam 0.3 cam_alpha 0.00 cam_beta 1.00 parameters are used to define the functional (See Ref-80).

Table 4.2: $Fe(CO)_5$ bond distances in Angstroms

DFT	DZP		cc-pVDZ		cc-pVTZ		cc-pVQZ	
Method	Fe-C^{ax}	Fe-C^{eq}	Fe-C^{ax}	Fe-C^{eq}	Fe-C^{ax}	Fe-C^{eq}	Fe-C^{ax}	Fe-C^{eq}
GGA								
BLYP	1.826	1.827	1.834	1.833	1.831	1.832	1.831	1.832
BP86	1.805	1.805	1.811	1.810	1.809	1.809	1.808	1.809
B97-D	1.812	1.812	1.818	1.817	1.815	1.816	1.814	1.816
HCTH147	1.799	1.801	1.805	1.805	1.802	1.804	1.801	1.804
HCTH407	1.794	1.796	1.800	1.801	1.797	1.800	1.796	1.799
Meta GGA								
M06-L	1.816	1.813	1.820	1.816	1.816	1.812	1.815	1.812
VSXC	1.835	1.835	1.841	1.839	1.838	1.837	1.837	1.837
Hybrid GGA								
BHLYP	1.854	1.822	1.865	1.829	1.859	1.827	1.859	1.827
MPW1K	1.812	1.794	1.819	1.798	1.814	1.797	1.814	1.797
BHandH	1.830	1.806	1.839	1.811	1.834	1.810	1.833	1.809
MPW1PW91	1.803	1.795	1.809	1.800	1.806	1.798	1.806	1.798
MPW1PBE	1.801	1.793	1.807	1.797	1.804	1.796	1.803	1.796
B1LYP	1.830	1.820	1.839	1.827	1.836	1.825	1.835	1.825
PBE1PBE	1.801	1.793	1.806	1.797	1.803	1.796	1.803	1.796
MPW1LYP	1.829	1.819	1.838	1.826	1.835	1.825	1.834	1.824
B98	1.816	1.809	1.823	1.814	1.819	1.812	1.819	1.812
X3LYP	1.823	1.815	1.831	1.821	1.828	1.820	1.827	1.820
B97-1	1.816	1.810	1.824	1.815	1.820	1.813	1.819	1.813
B97-2	1.805	1.799	1.811	1.804	1.807	1.802	1.807	1.802
MPW3PBE	1.801	1.795	1.807	1.800	1.804	1.798	1.803	1.798
B3LYP	1.823	1.816	1.831	1.822	1.828	1.821	1.827	1.821
B3PW91	1.803	1.797	1.809	1.802	1.806	1.800	1.806	1.800
B3P86	1.800	1.794	1.806	1.799	1.803	1.798	1.802	1.797
O3LYP	1.800	1.798	1.805	1.802	1.802	1.801	1.802	1.800
Hybrid Meta GGA								
M06-HF	1.964	1.849	1.992	1.860	1.960	1.845	1.961	1.840
M05-2X	1.853	1.824	1.865	1.831	1.855	1.825	1.854	1.824
M06-2X	1.883	1.840	1.898	1.848	1.882	1.839	1.881	1.838
MPWB1K	1.814	1.796	1.821	1.800	1.818	1.800	1.817	1.799
BB1K	1.813	1.797	1.821	1.801	1.817	1.800	1.816	1.800
M05	1.808	1.811	1.813	1.815	1.811	1.815	1.809	1.813
B1B95	1.806	1.797	1.812	1.801	1.809	1.801	1.809	1.801
M06	1.816	1.816	1.821	1.820	1.822	1.822	1.821	1.821
TPSSH	1.810	1.806	1.816	1.810	1.813	1.808	1.812	1.808
LC Hybrid GGA								
CAM-B3LYP	1.815	1.806	1.824	1.812	1.821	1.812	1.820	1.811
LC-ωPBE†	1.791	1.789	1.797	1.794	1.795	1.794	1.794	1.793
Experiment-1^{a}	1.807	1.827	1.807	1.827	1.807	1.827	1.807	1.827
Experiment-2^{b}	1.810	1.842	1.810	1.842	1.810	1.842	1.810	1.842
Experiment-3^{c}	1.811	1.803	1.811	1.803	1.811	1.803	1.811	1.803

^{a} Ref-29, gas ED structure; ^{b} Ref-30, gas ED structure; ^{c} Ref-20, crystal structure.
† Refer 4.1 footnote.

Table 4.3: $Cr(CO)_6$ bond distances in Angstroms

DFT Method	DZP Cr-C	cc-pVDZ Cr-C	cc-pVTZ Cr-C	cc-pVQZ Cr-C
GGA				
BLYP	1.931	1.931	1.934	1.934
BP86	1.907	1.905	1.908	1.909
B97-D	1.919	1.917	1.921	1.921
HCTH147	1.903	1.901	1.905	1.905
HCTH407	1.898	1.897	1.900	1.900
Meta GGA				
M06-L	1.922	1.919	1.919	1.921
VSXC	1.946	1.943	1.946	1.946
Hybrid GGA				
BHLYP	1.933	1.933	1.935	1.935
MPW1K	1.900	1.897	1.900	1.901
BHandH	1.915	1.913	1.916	1.916
MPW1PW91	1.900	1.897	1.900	1.901
MPW1PBE	1.897	1.895	1.898	1.898
B1LYP	1.928	1.928	1.931	1.931
q PBE1PBE	1.897	1.895	1.897	1.898
MPW1LYP	1.927	1.927	1.930	1.930
B98	1.913	1.913	1.914	1.915
X3LYP	1.922	1.922	1.925	1.925
B97-1	1.914	1.913	1.915	1.915
B97-2	1.904	1.901	1.904	1.905
MPW3PBE	1.899	1.897	1.900	1.900
B3LYP	1.923	1.923	1.925	1.925
B3PW91	1.901	1.899	1.902	1.903
B3P86	1.898	1.896	1.899	1.900
O3LYP	1.900	1.898	1.901	1.901
Hybrid Meta GGA				
M06-HF	1.950	1.954	1.943	1.940
M05-2X	1.929	1.928	1.928	1.929
M06-2X	1.945	1.944	1.942	1.942
MPWB1K	1.902	1.899	1.903	1.903
BB1K	1.902	1.899	1.903	1.904
M05	1.910	1.907	1.910	1.910
B1B95	1.901	1.899	1.903	1.904
M06	1.915	1.913	1.918	1.919
TPSSH	1.911	1.909	1.911	1.912
LC Hybrid GGA				
CAM-B3LYP	1.913	1.912	1.916	1.917
LC-ωPBE†	1.891	1.887	1.892	1.893
Experiment-1[a]	1.914	1.914	1.914	1.914
Experiment-2[b]	1.909	1.909	1.909	1.909
Experiment-3[c]	1.915	1.915	1.915	1.915

[a] Ref-44, Neutron diffraction; [b] Ref-45, crystal structure; [c] Ref-46, crystal structure (higher order X-ray data).
† Refer 4.1 footnote.

Table 4.4: $Co_2(CO)_8$ bond distances in Angstroms

DFT	DZP				cc-pVDZ				cc-pVTZ				cc-pVQZ			
Method	Co-Co	Co-C^b	Co-C^{2t}	Co-C^{4t}	Co-Co	Co-C^b	Co-C^{2t}	Co-C^{4t}	Co-Co	Co-C^b	Co-C^{2t}	Co-C^{4t}	Co-Co	Co-C^b	Co-C^{2t}	Co-C^{4t}
GGA																
BLYP	2.599	1.982	1.828	1.835	2.606	1.986	1.833	1.841	2.605	1.987	1.834	1.840				
BP86	2.550	1.957	1.805	1.813	2.556	1.961	1.809	1.818	2.553	1.960	1.808	1.815				
B97-D	2.548	1.969	1.821	1.824	2.555	1.973	1.825	1.829	2.552	1.972	1.824	1.827				
HCTH147	2.554	1.957	1.806	1.812	2.562	1.960	1.810	1.817	2.558	1.959	1.809	1.814	2.561	1.958	1.809	1.813
HCTH407	2.545	1.952	1.802	1.808	2.554	1.955	1.806	1.812	2.548	1.953	1.805	1.808	2.551	1.953	1.805	1.808
Meta GGA																
M06-L	2.525	1.961	1.815	1.825	2.536	1.962	1.818	1.829	2.527	1.960	1.815	1.822	2.526	1.960	1.813	1.822
VSXC	2.496	1.990	1.841	1.859	2.499	1.986	1.845	1.863	2.496	1.988	1.844	1.861				
Hybrid GGA																
BHLYP	2.533	1.940	1.828	1.839	2.546	1.946	1.833	1.844	2.545	1.947	1.833	1.841	2.548	1.947	1.834	1.841
MPW1K	2.487	1.919	1.798	1.807	2.495	1.923	1.801	1.811	2.493	1.923	1.800	1.807	2.496	1.923	1.801	1.807
BHandH	2.504	1.926	1.809	1.819	2.515	1.931	1.813	1.824	2.513	1.931	1.813	1.821	2.516	1.931	1.813	1.820
MPW1PW91	2.507	1.932	1.798	1.806	2.514	1.935	1.802	1.810	2.512	1.935	1.801	1.806	2.515	1.935	1.801	1.806
MPW1PBE	2.503	1.930	1.796	1.804	2.510	1.933	1.799	1.808	2.508	1.933	1.798	1.804	2.511	1.933	1.799	1.804
B1LYP	2.559	1.956	1.825	1.832	2.570	1.961	1.830	1.837	2.568	1.962	1.830	1.835	2.571	1.962	1.831	1.835
PBE1PBE	2.503	1.930	1.796	1.803	2.511	1.933	1.799	1.807	2.508	1.933	1.798	1.804	2.511	1.932	1.799	1.804
MPW1LYP	2.557	1.955	1.823	1.830	2.568	1.960	1.828	1.836	2.566	1.961	1.829	1.834	2.570	1.960	1.829	1.834
B98	2.539	1.947	1.813	1.820	2.547	1.952	1.817	1.825	2.545	1.951	1.817	1.821	2.548	1.951	1.817	1.821
X3LYP	2.553	1.953	1.819	1.825	2.563	1.958	1.824	1.831	2.561	1.958	1.824	1.829	2.565	1.958	1.825	1.829
B97-1	2.539	1.949	1.813	1.821	2.546	1.953	1.817	1.826	2.544	1.952	1.817	1.822	2.547	1.952	1.817	1.822
B97-2	2.521	1.939	1.805	1.811	2.530	1.942	1.809	1.815	2.526	1.942	1.808	1.811	2.529	1.941	1.808	1.811
MPW3PBE	2.513	1.935	1.798	1.805	2.520	1.938	1.801	1.809	2.517	1.938	1.801	1.806	2.521	1.938	1.801	1.806
B3LYP	2.557	1.955	1.820	1.826	2.567	1.960	1.825	1.832	2.565	1.961	1.825	1.830	2.568	1.961	1.825	1.829
B3PW91	2.517	1.937	1.800	1.807	2.525	1.941	1.804	1.812	2.522	1.940	1.803	1.808	2.525	1.940	1.804	1.808
B3P86	2.514	1.933	1.797	1.804	2.521	1.936	1.801	1.808	2.518	1.936	1.800	1.805	2.522	1.936	1.800	1.805
O3LYP	2.531	1.944	1.803	1.809	2.537	1.947	1.807	1.814	2.534	1.946	1.805	1.810	2.538	1.946	1.806	1.810
Hybrid Meta GGA																
M06-HF	2.661	2.031	1.942	1.927	2.678	2.066	1.945	1.933	2.675	2.048	1.941	1.926	2.679	2.052	1.948	1.921
M05-2X	2.554	1.947	1.845	1.847	2.567	1.955	1.849	1.852	2.565	1.954	1.849	1.845	2.567	1.954	1.849	1.845
M06-2X	2.575	1.965	1.864	1.873	2.592	1.972	1.868	1.881	2.589	1.972	1.867	1.871	2.592	1.972	1.868	1.871
MPWB1K	2.468	1.916	1.801	1.810	2.477	1.919	1.804	1.814	2.473	1.919	1.804	1.810	2.476	1.919	1.805	1.810
BB1K	2.471	1.919	1.802	1.810	2.480	1.921	1.805	1.814	2.476	1.921	1.805	1.811	2.479	1.921	1.806	1.810
M05	2.520	1.945	1.825	1.817	2.531	1.947	1.832	1.822	2.527	1.950	1.832	1.819	2.526	1.948	1.832	1.818
B1B95	2.487	1.929	1.802	1.809	2.495	1.931	1.806	1.813	2.491	1.931	1.805	1.810	2.494	1.931	1.806	1.810
M06	2.531	1.947	1.826	1.824	2.538	1.948	1.831	1.828	2.537	1.952	1.833	1.829	2.538	1.952	1.833	1.828
TPSSH	2.514	1.946	1.806	1.816	2.520	1.948	1.809	1.820	2.516	1.947	1.808	1.816	2.519	1.947	1.808	1.816
LC Hybrid GGA																
CAM-B3LYP	2.514	1.930	1.812	1.818	2.526	1.934	1.817	1.824	2.523	1.935	1.818	1.822	2.526	1.935	1.818	1.822
LC-ωPBE†	2.477	1.918	1.795	1.801	2.485	1.921	1.799	1.806	2.481	1.920	1.798	1.803				
Experiment-1 [a]	2.528	1.939	1.816	1.832	2.528	1.939	1.816	1.832	2.528	1.939	1.816	1.832	2.528	1.939	1.816	1.832

[a] Ref-18, crystal structure.
† Refer 4.1 footnote.

Table 4.5: $Fe_2(CO)_9$ bond distances in Angstroms

DFT	DZP			cc-pVDZ			cc-pVTZ			cc-pVQZ		
Method	Fe-Fe	Fe-C^b	Fe-C^t	Fe-Fe	Fe-C^b	Fe-C^t	Fe-Fe	Fe-C^b	Fe-C^t	Fe-Fe	Fe-C^b	Fe-C^t
GGA												
BLYP	2.566	2.034	1.841	2.575	2.040	1.849	2.572	2.040	1.846	2.575	2.040	1.846
BP86	2.519	2.006	1.819	2.526	2.010	1.826	2.522	2.010	1.822	2.524	2.010	1.822
B97-D	2.536	2.020	1.829	2.544	2.025	1.837	2.540	2.024	1.833	2.542	2.023	1.833
HCTH147	2.516	2.004	1.815	2.525	2.009	1.822	2.519	2.007	1.818	2.522	2.007	1.817
HCTH407	2.504	1.998	1.810	2.513	2.001	1.817	2.506	1.999	1.812	2.509	1.999	1.812
Meta GGA												
M06-L	2.515	2.010	1.827	2.521	2.011	1.834	2.512	2.009	1.827	2.514	2.010	1.826
VSXC	2.561	2.034	1.856	2.560	2.031	1.864	2.559	2.034	1.858	2.561	2.034	1.859
Hybrid GGA												
BHLYP	2.502	1.996	1.839	2.515	2.004	1.847	2.510	2.002	1.842	2.512	2.002	1.842
MPW1K	2.459	1.970	1.807	2.466	1.973	1.813	2.462	1.972	1.808	2.464	1.973	1.809
BHandH	2.473	1.978	1.819	2.484	1.985	1.827	2.478	1.983	1.822	2.481	1.984	1.822
MPW1PW91	2.479	1.981	1.807	2.485	1.984	1.814	2.481	1.984	1.810	2.484	1.984	1.810
MPW1PBE	2.475	1.979	1.805	2.481	1.982	1.812	2.477	1.981	1.807	2.480	1.981	1.807
B1LYP	2.528	2.009	1.833	2.539	2.016	1.841	2.535	2.015	1.837	2.537	2.015	1.838
PBE1PBE	2.473	1.978	1.805	2.480	1.981	1.811	2.476	1.980	1.807	2.478	1.981	1.807
MPW1LYP	2.526	2.008	1.832	2.537	2.014	1.840	2.533	2.013	1.837	2.535	2.014	1.837
B98	2.507	1.998	1.821	2.516	2.003	1.829	2.510	2.001	1.824	2.513	2.001	1.824
X3LYP	2.522	2.005	1.828	2.532	2.011	1.836	2.528	2.010	1.832	2.530	2.011	1.832
B97-1	2.507	2.000	1.822	2.515	2.004	1.830	2.510	2.002	1.824	2.512	2.002	1.825
B97-2	2.490	1.987	1.812	2.497	1.991	1.818	2.492	1.990	1.814	2.495	1.990	1.814
MPW3PBE	2.484	1.984	1.807	2.490	1.987	1.814	2.486	1.986	1.810	2.489	1.987	1.810
B3LYP	2.526	2.008	1.829	2.536	2.014	1.837	2.532	2.013	1.833	2.534	2.013	1.833
B3PW91	2.488	1.986	1.810	2.495	1.990	1.816	2.491	1.989	1.812	2.494	1.990	1.812
B3P86	2.483	1.982	1.807	2.490	1.986	1.813	2.486	1.985	1.809	2.489	1.985	1.809
O3LYP	2.495	1.991	1.810	2.501	1.994	1.817	2.496	1.992	1.812	2.499	1.993	1.812
Hybrid Meta GGA												
M06-HF	2.477	2.026	1.894	2.496	2.057	1.909	2.466	2.031	1.888	2.471	2.030	1.887
M05-2X	2.498	1.996	1.839	2.514	2.008	1.848	2.503	2.003	1.839	2.506	2.003	1.839
M06-2X	2.517	2.014	1.859	2.535	2.027	1.869	2.519	2.018	1.857	2.522	2.020	1.857
MPWB1K	2.449	1.965	1.809	2.455	1.967	1.816	2.451	1.966	1.812	2.454	1.967	1.812
BB1K	2.453	1.967	1.810	2.458	1.969	1.816	2.454	1.968	1.812	2.457	1.969	1.812
M05	2.479	1.988	1.821	2.485	1.987	1.829	2.480	1.989	1.824	2.480	1.987	1.823
B1B95	2.468	1.976	1.810	2.473	1.978	1.817	2.470	1.977	1.813	2.472	1.978	1.813
M06	2.497	1.993	1.827	2.501	1.994	1.835	2.503	1.998	1.833	2.504	1.998	1.833
TPSSH	2.499	1.996	1.819	2.503	1.998	1.826	2.499	1.997	1.821	2.502	1.998	1.821
LC Hybrid GGA												
CAM-B3LYP	2.485	1.980	1.821	2.495	1.985	1.829	2.491	1.985	1.826	2.494	1.985	1.826
LC-ωPBE†	2.452	1.963	1.804	2.457	1.964	1.812	2.454	1.965	1.807	2.457	1.965	1.808
Experiment [a]	2.523	2.016	1.838	2.523	2.016	1.838	2.523	2.016	1.838	2.523	2.016	1.838

[a] Ref-69, crystal structure.
† Refer 4.1 footnote.

Table 4.6: $Mn_2(CO)_{10}$ bond distances in Angstroms

DFT		DZP			cc-pVDZ			cc-pVTZ			cc-pVQZ	
Method	Mn-Mn	Mn-C^{ax}	Mn-C^{eq}	Mn-Mn	Mn-C^{ax}	Mn-C^{eq}	Mn-Mn	Mn-C^{ax}	Mn-C^{eq}	Mn-Mn	Mn-C^{ax}	Mn-C^{eq}
GGA												
BLYP	3.067	1.825	1.871	3.056	1.831	1.875	3.093	1.828	1.876	3.101	1.828	1.875
BP86	2.955	1.803	1.851	2.956	1.807	1.853	2.974	1.804	1.853	2.983	1.804	1.853
B97-D	2.988	1.812	1.855	2.989	1.817	1.857	3.004	1.814	1.858	3.011	1.813	1.858
HCTH147	3.037	1.792	1.845	3.031	1.796	1.847	3.061	1.793	1.848	3.071	1.792	1.847
HCTH407	3.046	1.786	1.841	3.031	1.796	1.847	3.075	1.786	1.844	3.084	1.786	1.843
Meta GGA												
M06-L	2.901	1.811	1.864	2.940	1.815	1.865	2.934	1.809	1.863	2.938	1.808	1.864
VSXC	2.973	1.841	1.883	3.005	1.849	1.884	2.994	1.843	1.885	3.008	1.843	1.885
Hybrid GGA												
BHLYP	3.013	1.832	1.881	3.033	1.841	1.888	3.045	1.834	1.886	3.050	1.833	1.885
MPW1K	2.903	1.796	1.848	2.925	1.801	1.851	2.927	1.796	1.850	2.935	1.795	1.850
BHandH	2.953	1.812	1.862	2.974	1.819	1.867	2.980	1.813	1.865	2.987	1.812	1.865
MPW1PW91	2.910	1.793	1.845	2.925	1.797	1.847	2.933	1.793	1.847	2.941	1.793	1.847
MPW1PBE	2.915	1.792	1.843	2.926	1.796	1.846	2.936	1.793	1.846	2.945	1.792	1.846
B1LYP	3.019	1.820	1.870	3.025	1.826	1.875	3.048	1.822	1.875	3.054	1.821	1.874
PBE1PBE	2.897	1.791	1.842	2.914	1.794	1.844	2.919	1.791	1.845	2.927	1.790	1.844
MPW1LYP	3.010	1.819	1.869	3.016	1.826	1.874	3.038	1.822	1.874	3.045	1.821	1.873
B98	2.968	1.807	1.858	2.977	1.812	1.861	2.989	1.808	1.860	2.997	1.807	1.861
X3LYP	2.998	1.814	1.864	3.004	1.820	1.868	3.025	1.816	1.868	3.032	1.815	1.868
B97-1	2.958	1.808	1.859	2.970	1.813	1.862	2.981	1.808	1.861	2.988	1.808	1.861
B97-2	2.958	1.794	1.848	2.969	1.797	1.850	2.982	1.794	1.850	2.991	1.793	1.849
MPW3PBE	2.903	1.791	1.843	2.917	1.794	1.845	2.924	1.791	1.845	2.933	1.790	1.844
B3LYP	3.007	1.814	1.864	3.011	1.820	1.869	3.034	1.817	1.869	3.041	1.816	1.868
B3PW91	2.928	1.794	1.846	2.939	1.798	1.848	2.949	1.794	1.848	2.958	1.794	1.848
B3P86	2.912	1.792	1.842	2.923	1.795	1.845	2.933	1.792	1.845	2.942	1.792	1.845
O3LYP	2.991	1.790	1.844	2.998	1.792	1.846	3.016	1.789	1.846	3.026	1.789	1.846
Hybrid Meta GGA												
M06-HF	2.953	1.892	1.927	2.982	1.916	1.944	2.958	1.883	1.922	2.974	1.877	1.916
M05-2X	2.948	1.822	1.877	2.964	1.831	1.884	2.963	1.820	1.879	2.973	1.818	1.878
M06-2X	2.950	1.841	1.898	2.982	1.853	1.907	2.970	1.837	1.899	2.979	1.834	1.898
MPWB1K	2.844	1.799	1.850	2.879	1.805	1.853	2.869	1.800	1.853	2.877	1.799	1.853
BB1K	2.848	1.799	1.850	2.882	1.804	1.853	2.872	1.799	1.853	2.882	1.798	1.853
M05	2.901	1.802	1.853	2.931	1.805	1.854	2.936	1.802	1.855	2.935	1.801	1.854
B1B95	2.851	1.795	1.847	2.881	1.800	1.849	2.873	1.796	1.850	2.886	1.796	1.850
M06	2.913	1.812	1.859	2.914	1.817	1.861	2.933	1.815	1.864	2.934	1.814	1.863
TPSSH	2.897	1.806	1.855	2.915	1.810	1.857	2.917	1.806	1.857	2.926	1.806	1.856
LC Hybrid GGA												
CAM-B3LYP	2.932	1.807	1.855	2.946	1.814	1.859	2.959	1.810	1.860	2.966	1.809	1.859
LC-ωPBE†	2.836	1.787	1.835	2.857	1.791	1.837	2.856	1.788	1.838	2.866	1.788	1.838
Experiment-1[a]	2.895	1.820	1.859	2.895	1.820	1.859	2.895	1.820	1.859	2.895	1.820	1.859
Experiment-2[b]	2.923	1.792	1.830	2.923	1.792	1.830	2.923	1.792	1.830	2.923	1.792	1.830
Experiment-3[c]	2.977	1.803	1.873	2.977	1.803	1.873	2.977	1.803	1.873	2.977	1.803	1.873

[a] Ref-77, structure from electron density; [b] Ref-74, crystal structure; [c] Ref-78, gas phase electron diffraction.
† Refer 4.1 footnote.

References

(1) Ziegler, T. *Can. J. Chem.* **1995**, *73*, 743–761.

(2) Ignatyev, I. S.; Schaefer, H. F. III,; King, R. B.; Brown, S. T. *J. Am. Chem. Soc.* **2000**, *122*, 1989–1994.

(3) Schultz, N. E.; Zhao, Y.; Truhlar, D. G. *J. Phys. Chem. A* **2005**, *109*, 11127–11143.

(4) Schultz, N. E.; Zhao, Y.; Truhlar, D. G. *J. Phys. Chem. A* **2005**, *109*, 4388–4403.

(5) Boese, A. D.; Martin, J. M. L.; Handy, N. C. *J. Chem. Phys.* **2003**, *119*, 3005–3014.

(6) Jensen, F. *J. Chem. Phys.* **2002**, *116*, 7372–7379.

(7) Wang, N. X.; Wilson, A. K. *J. Chem. Phys.* **2004**, *121*, 7632–7646.

(8) Tekarli, S. M.; Drummond, M. L.; Williams, T. G.; Cundari, T. R.; Wilson, A. K. *J. Phys. Chem. A* **2009**, *113*, 8607–8614.

(9) Dunning, T. H. *J. Chem. Phys.* **1989**, *90*, 1007–1023.

(10) Balabanov, N. B.; Peterson, K. A. *J. Chem. Phys.* **2005**, *123*, 064107.

(11) Balabanov, N. B.; Peterson, K. A. *J. Chem. Phys.* **2006**, *125*, 074110.

(12) Dunning, T. H. *J. Chem. Phys.* **1970**, *53*, 2823–2833.

(13) Huzinaga, S. *J. Chem. Phys.* **1965**, *43*, 1293–1302.

(14) Wachters, A. J. H. *J. Chem. Phys.* **1970**, *52*, 1033–1036.

(15) Hood, D. M.; Pitzer, R. M.; Schaefer, H. F. III, *J. Chem. Phys.* **1979**, *71*, 705–712.

(16) Valiev, M.; Bylaska, E. J.; Govind, N.; Kowalski, K.; Straatsma, T. P.; van Dam, H. J. J.; Wang, D.; Nieplocha, J.; Apra, E.; Windus, T. L.; de Jong, W. A. *Comput. Phys. Commun.* **2010**, *181*, 1477–1489.

(17) Papas, B. N.; Schaefer, H. F. III, *J. Mol. Struct. THEOCHEM* **2006**, *768*, 175–181.

(18) Leung, P. C.; Coppens, P. *Acta Cryst.* **1983**, *B39*, 535–542.

(19) Ladell, J.; Post, B.; Fankuchen, I. *Acta Cryst.* **1952**, *5*, 795–800.

(20) Braga, D.; Grepioni, F.; Orpen, A. G. *Organometallics* **1993**, *12*, 1481–1483.

(21) Hedberg, L.; Iijima, T.; Hedberg, K. *J. Chem. Phys.* **1979**, *70*, 3224–3229.

(22) Mitin, A. V.; Baker, J.; Pulay, P. *J. Chem. Phys.* **2003**, *118*, 7775–7782.

(23) Bolshakov, V. I.; Rossikhin, V. V.; Voronkov, E. U.; Okovytyy, S. I.; Leszczynski, J. *J. Comput. Chem.* **2007**, *28*, 778–782.

(24) Calaminici, P.; Janetzko, F.; Köster, A. M.; Mejia-Olvera, R.; Zuniga-Gutierrez, B. *J. Chem. Phys.* **2007**, *126*, 044108.

(25) Davis, M. I.; Hanson, H. P. *J. Phys. Chem.* **1965**, *69*, 3405–3410.

(26) Hanson, H. P. *J. Phys. Chem.* **1967**, *71*, 775–777.

(27) Beagley, B.; Cruickshank, D. W. J.; Pinder, P. M.; Robiette, A. G.; Sheldrick, G. M. *Acta Crystallog., Sect. B* **1969**, *25*, 737.

(28) Almenningen, A.; Haaland, A.; Wahl, K. *Acta Chem. Scand.* **1969**, *23*, 2245–2252.

(29) Beagley, B.; Schmidling, D. G. *J. Mol. Struct.* **1974**, *22*, 466–468.

(30) McClelland, B. W.; Robiette, A. G.; Hedberg, L.; Hedberg, K. *Inorg. Chem.* **2001**, *40*, 1358–1362.

(31) Lüthi, H. P.; Siegbahn, P. E. M.; Almlöf, J. *J. Phys. Chem.* **1985**, *89*, 2156–2161.

(32) Jonas, V.; Thiel, W. *J. Chem. Phys.* **1995**, *102*, 8474–8484.

(33) Bérces, A.; Ziegler, T. *J. Phys. Chem.* **1995**, *99*, 11417–11423.

(34) Li, J.; Schreckenbach, G.; Ziegler, T. *J. Am. Chem. Soc.* **1995**, *117*, 486–494.

(35) Jang, J. H.; Lee, J. G.; Lee, H.; Xie, Y.; Schaefer, H. F. III, *J. Phys. Chem. A* **1998**, *102*, 5298–5304.

(36) González-Blanco, O.; Branchadell, V. *J. Chem. Phys.* **1999**, *110*, 778–783.

(37) Ehlers, A. W.; Frenking, G. *J. Am. Chem. Soc.* **1994**, *116*, 1514–1520.

(38) Fan, L. Y.; Ziegler, T. *J. Chem. Phys.* **1991**, *95*, 7401–7408.

(39) Fournier, R. *J. Chem. Phys.* **1993**, *99*, 1801–1815.

(40) Farrugia, L. J.; Evans, C. *J. Phys. Chem. A* **2005**, *109*, 8834–8848.

(41) Ishikawa, Y.; Kawakami, K. *J. Phys. Chem. A* **2007**, *111*, 9940–9944.

(42) Delley, B.; Wrinn, M.; Lüthi, H. P. *J. Chem. Phys.* **1994**, *100*, 5785–5791.

(43) Li, J.; Schreckenbach, G.; Ziegler, T. *J. Phys. Chem.* **1994**, *98*, 4838–4841.

(44) Jost, A.; Rees, B.; Yelon, W. B. *Acta Cryst.* **1975**, *B31*, 2649–2658.

(45) Whitaker, A.; Jeffery, J. W. *Acta Cryst.* **1967**, *23*, 977–984.

(46) Rees, B.; Mitschler, A. *J. Am. Chem. Soc.* **1976**, *98*, 7918–7924.

(47) Koelle, U. In *Encyclopedia of Inorganic Chemistry*; King, R., Ed.; Wiley: Chichester, England, 1994; pp 773–747.

(48) Bor, G.; Noack, K. *J. Organomet. Chem.* **1974**, *64*, 367–372.

(49) Bor, G.; Dietler, U. K.; Noack, K. *J. Chem. Soc. Chem. Commun.* **1976**, 914–916.

(50) Onaka, S.; Shriver, D. F. *Inorg. Chem.* **1976**, *15*, 915–918.

(51) Kenny, J. P.; King, R. B.; Schaefer, H. F. III, *Inorg. Chem.* **2001**, *40*, 900–911.

(52) Sumner, G. G.; Klug, H. P.; Alexander, L. E. *Acta Cryst.* **1964**, *17*, 732–742.

(53) Braga, D.; Grepioni, F.; Sabatino, P.; Gavezzotti, A. *J. Chem. Soc., Dalton Trans.* **1992**, 1185–1191.

(54) Thorn, D. L. *Inorg. Chem.* **1978**, *17*, 126–140.

(55) Dedieu, A.; Albright, T. A.; Hoffmann, R. *J. Am. Chem. Soc.* **1979**, *101*, 3141–3151.

(56) Heijser, W.; Baerends, E. J.; Ros, P. *Faraday Symp. Chem. Soc.* **1980**, *14*, 211–234.

(57) Bellagamba, V.; Ercoli, R.; Gamba, A.; Suffritti, G. B. *J. Organomet. Chem.* **1980**, *190*, 381–392.

(58) Low, A. A.; Kunze, K. L.; MacDougall, P. J.; Hall, M. B. *Inorg. Chem.* **1991**, *30*, 1079–1086.

(59) Folga, E.; Ziegler, T. *J. Am. Chem. Soc.* **1993**, *115*, 5169–5176.

(60) Uffing, C.; Ecker, A.; Köppe, R.; Schnöckel, H. *Organometallics* **1998**, *17*, 2373–2375.

(61) Barckholtz, T. A.; Bursten, B. E. *J. Am. Chem. Soc.* **1998**, *120*, 1926–1927.

(62) Barckholtz, T. A.; Bursten, B. E. *J. Organomet. Chem.* **2000**, *596*, 212–220.

(63) Summerville, R. H.; Hoffmann, R. *J. Am. Chem. Soc.* **1979**, *98*, 7240–7254.

(64) Bauschlicher, C. W. *J. Chem. Phys.* **1986**, *84*, 872–875.

(65) Rosa, A.; Baerends, E. J. *New. J. Chem.* **1991**, *15*, 815–829.

(66) Bo, C.; Sarasa, J.-P.; Poblet, J.-M. *J. Phys. Chem.* **1993**, *97*, 6362–6366.

(67) Reinhold, J.; Hunstock, E. *New J. Chem.* **1994**, *18*, 465–471.

(68) Jacobsen, H.; Ziegler, T. *J. Am. Chem. Soc.* **1996**, *118*, 4631–4635.

(69) Cotton, F. A.; Troup, J. M. *J. Chem. Soc., Dalton Trans.* **1974**, 800–802.

(70) Brimm, E. O.; Lynch, M. A.; Sesny, W. J. *J. Am. Chem. Soc.* **1954**, *76*, 3831–3835.

(71) Closson, R. D.; Buzbee, L. R.; Ecke, G. C. *J. Am. Chem. Soc.* **1958**, *80*, 6167–6170.

(72) Podall, H. E.; Dunn, J. H.; Shapiro, H. J. *J. Am. Chem. Soc.* **1960**, *82*, 1325–1330.

(73) Xie, Y.; Jang, J. H.; King, R. B.; Schaefer, H. F. III, *Inorg. Chem.* **2003**, *42*, 5219–5230.

(74) Dahl, L. F.; Rundle, R. E. *Acta Cryst.* **1963**, *16*, 419–426.

(75) Dahl, L. F.; Ishishi, E.; Rundle, R. E. *J. Chem. Phys.* **1957**, *26*, 1750–1751.

(76) Churchill, M. R.; Amoh, K. N.; Wasserman, H. J. *Inorg. Chem.* **1981**, *20*, 1609–1611.

(77) Martin, M.; Rees, B.; Mitschler, A. *Acta Cryst.* **1982**, *B38*, 6–15.

(78) Almennin, A.; Jacobsen, G. G.; Seip, H. M. *Acta Chem. Scand.* **1969**, *23*, 685–686.

(79) Maurer, S. A.; Lambrecht, D. S.; Flaig, D.; Ochsenfeld, C. *J. Chem. Phys.* **2012**, *136*, 144107.

(80) `http://www.nwchem-sw.org/index.php/Release61:Density_Functional_Theory_for_Molecules`.

Chapter 5

Conclusions

In this dissertation, ab initio methods and density functional theory were employed to in areas of bio-inorganic and combustion chemistry. The powerful applications of computational chemistry for providing accurate energetic data for kinetic modeling studies and for interpreting experimental data was demonstrated. Also, a benchmarking study was conducted to assess the role of basis set size in the prediction of metal-metal and metal-ligand bonds by a number of density functional methods.

Kinetic modeling studies of reaction mechanisms that are relevant combustion studies often rely on accurate energetic data. We have employed high level *ab initio* coupled cluster methods to compute relative energies of reactants, products and transition states on the C_3H_5 potential energy surface (PES). An unrestricted Hartree-Fock (UHF) method was used as a reference wavefunction for all the open shell structures in the study. The choice of UHF reference was justified by demonstrating that the powerful correlation treatment provided by coupled cluster theory causes only negligible deviation in spin purity. The final barrier heights were obtained by extrapolating the relative energies into the complete basis set limit using the focal point technique. The study acts as a guide for choice of methodology for future combustion chemistry studies. A combination of high-level theory and accurate experimental data is important to construct kinetic models that can explain the mechanisms of reactions that are significant in poly aromatic hydrocarbon formation and can eventually lead to the development of 'clean' fuel technologies.

In the second study, density functional theory was employed to explain the role of hydrogen bonding in model complexes of Nickel Superoxide Dismutase. The optimized geometries of the model complexes compare well with the crystallographic data. Composition of frontier molecular orbitals, natural charges and point electrostatic potentials demonstrate a correlation between hydrogen bonding and protection against S-oxidation in the model complexes. The study demonstrates the importance of electronic structure computations to understand the molecular level interactions that are conducive to metal based oxidation in Nickel Superoxide Dismutase. It is an example of how theory and experiment work together for arriving at meaningful conclusions.

In the last study, we have shown that relatively small basis sets, such as the Hood-Pitzer basis set, can give surprisingly accurate structures for compounds involving 3d transition metals. We have used metal-metal and metal-carbon bond lengths as a diagnostic for comparing the structures with experiment. Unlike in wavefunction methods, where increase in basis set size systematically improves the geometries of optimized structures, density functional methods do not guarantee a significant amount of improvement in predicted structures with large basis sets such as cc-pVTZ or cc-pVQZ. Moreover, while optimizing large systems involving transition metals, using large basis sets is not practicable. Even when one resorts to linear scaling methods for decreasing the computational time, extended basis sets that involve diffuse functions are not advantageous. Our study provides an alternative to optimizing large systems that involve transition metals by showing that the Hood-Pitzer basis set predicts reasonably accurate geometries.

APPENDIX A

Table A1 : Valence focal point analysis of the relative energy (in kcal mol^{-1}) of **Propyne+H** with respect to allene+H.[a]

	HF	+δMP2	+δCCSD	+δCCSD(T)	+δCCSDT	+δCCSDT(Q)	ΔE_e[CCSDT(Q)]
cc-pVDZ	−1.11	−3.08	+3.44	+0.28	+0.17	−0.09	[−0.39]
cc-pVTZ	−1.62	−3.04	+3.20	+0.29	+0.17	[−0.09]	[−1.09]
cc-pVQZ	−1.62	−3.11	+3.11	+0.32	[+0.17]	[−0.09]	[−1.23]
cc-pV5Z	−1.59	−3.18	[+3.11]	[+0.32]	[+0.17]	[−0.09]	[−1.27]
cc-pV6Z	−1.59	−3.23	[+3.11]	[+0.32]	[+0.17]	[−0.09]	[−1.31]
CBS LIMIT	[−1.58]	[−3.29]	[+3.11]	[+0.32]	[+0.17]	[−0.09]	[−**1.38**]
ΔE_0(final)	=	ΔE_e[CBS CCSDT(Q)] + ΔE_{core} + $\Delta E_{\text{relativity}}$ + ΔE_{ZPVE}					
	=	-1.38 -0.05 +0.00 +0.29 = **-1.14 kcal mol^{-1}**					

[a]The symbol δ denotes the increment in the relative energy (ΔE_e) with respect to the preceding level of theory in the hierarchy RHF→ MP2→ CCSD→ CCSD(T)→ CCSDT → CCSDT(Q). Square brackets signify results obtained from basis set extrapolations or additivity assumptions. Final predictions are boldfaced.

Table A2 : Valence focal point analysis of the relative energy (in kcal mol^{-1}) of $\mathbf{C_3H_3}$+$\mathbf{H_2}$ with respect to allene+H.

	HF	+δMP2	+δCCSD	+δCCSD(T)	+δCCSDT	+δCCSDT(Q)	ΔE_e[CCSDT(Q)]
cc-pVDZ	−11.44	+12.32	−10.01	+0.87	−0.34	−0.08	[−8.67]
cc-pVTZ	−13.36	+12.20	−10.75	+1.07	−0.41	[−0.08]	[−11.34]
cc-pVQZ	−13.47	+12.27	−11.00	+1.09	[−0.41]	[−0.08]	[−11.59]
cc-pV5Z	−13.45	+12.25	[−11.00]	[+1.09]	[−0.41]	[−0.08]	[−11.60]
cc-pV6Z	−13.45	+12.25	[−11.00]	[+1.09]	[−0.41]	[−0.08]	[−11.59]
CBS LIMIT	[−13.45]	[+12.25]	[−11.00]	[+1.09]	[−0.41]	[−0.08]	[**−11.59**]
ΔE_0(final)	=	ΔE_e[CBS CCSDT(Q)] + $\Delta E_{\rm core}$ + $\Delta E_{\rm relativity}$ + $\Delta E_{\rm ZPVE}$					
	=	-11.59 +0.08 -0.02 -2.49 = **-14.02 kcal mol^{-1}**					

[a]See footnote of A1 for an explanation of the notation used.

Table A3 : Valence focal point analysis of the relative energy (in kcal mol^{-1}) of **Allyl** with respect to allene+H.

	HF	+δMP2	+δCCSD	+δCCSD(T)	+δCCSDT	+δCCSDT(Q)	ΔE_e[CCSDT(Q)]
cc-pVDZ	−67.36	+14.01	−9.57	+1.76	−0.45	+0.15	[−61.45]
cc-pVTZ	−66.84	+13.09	−10.36	+2.03	−0.61	[+0.15]	[−62.53]
cc-pVQZ	−66.76	+13.06	−10.63	+2.07	[−0.61]	[+0.15]	[−62.73]
cc-pV5Z	−66.77	+13.02	[−10.63]	[+2.07]	[−0.61]	[+0.15]	[−62.77]
cc-pV6Z	−66.77	+13.03	[−10.63]	[+2.07]	[−0.61]	[+0.15]	[−62.76]
CBS LIMIT	[−66.77]	[+13.04]	[−10.63]	[+2.07]	[−0.61]	[+0.15]	[**−62.75**]
ΔE_0(final)	=	ΔE_e[CBS CCSDT(Q)] + $\Delta E_{\rm core}$ + $\Delta E_{\rm relativity}$ + $\Delta E_{\rm ZPVE}$					
	=	-62.75 +0.11 +0.02 +6.97 = **-55.65 kcal mol^{-1}**					

[a]See footnote of A1 for an explanation of the notation used.

Table A4 : Valence focal point analysis of the relative energy (in kcal mol^{-1}) of $\mathbf{CH_3CCH_2}$ with respect to allene+H.

	HF	+δMP2	+δCCSD	+δCCSD(T)	+δCCSDT	+δCCSDT(Q)	ΔE_e[CCSDT(Q)]
cc-pVDZ	−45.76	+11.89	−9.47	+1.65	−0.41	+0.17	[−41.92]
cc-pVTZ	−45.11	+11.17	−10.14	+1.90	−0.55	[+0.17]	[−42.55]
cc-pVQZ	−45.04	+11.25	−10.44	+1.95	[−0.55]	[+0.17]	[−42.66]
cc-pV5Z	−45.03	+11.27	[−10.44]	[+1.95]	[−0.55]	[+0.17]	[−42.63]
cc-pV6Z	−45.04	+11.32	[−10.44]	[+1.95]	[−0.55]	[+0.17]	[−42.59]
CBS LIMIT	[−45.04]	[+11.38]	[−10.44]	[+1.95]	[−0.55]	[+0.17]	[−**42.52**]
ΔE_0(final)	=	ΔE_e[CBS CCSDT(Q)] + ΔE_{core} + $\Delta E_{\text{relativity}}$ + ΔE_{ZPVE}					
	=	-42.52+0.14 +0.02 +6.83 = **-35.53 kcal mol^{-1}**					

[a]See footnote of A1 for an explanation of the notation used.

Table A5 : Valence focal point analysis of the relative energy (in kcal mol^{-1}) of $\mathbf{CH_3CHCH}$-**trans** with respect to allene+H.

	HF	+δMP2	+δCCSD	+δCCSD(T)	+δCCSDT	+δCCSDT(Q)	ΔE_e[CCSDT(Q)]
cc-pVDZ	−42.42	+12.58	−9.91	+1.64	−0.42	+0.17	[−38.37]
cc-pVTZ	−41.69	+12.01	−10.62	+1.89	−0.56	[+0.17]	[−38.81]
cc-pVQZ	−41.61	+12.17	−10.93	+1.94	[−0.56]	[+0.17]	[−38.83]
cc-pV5Z	−41.60	+12.21	[−10.93]	[+1.94]	[−0.56]	[+0.17]	[−38.77]
cc-pV6Z	−41.60	+12.27	[−10.93]	[+1.94]	[−0.56]	[+0.17]	[−38.71]
CBS LIMIT	[−41.60]	[+12.35]	[−10.93]	[+1.94]	[−0.56]	[+0.17]	[−**38.63**]
ΔE_0(final)	=	ΔE_e[CBS CCSDT(Q)] + ΔE_{core} + $\Delta E_{\text{relativity}}$ + ΔE_{ZPVE}					
	=	-38.63 +0.19 +0.02 +7.02 = **-31.40 kcal mol^{-1}**					

[a]See footnote of A1 for an explanation of the notation used.

Table A6 : Valence focal point analysis of the relative energy (in kcal mol^{-1}) of **CH_3CHCH-cis** with respect to allene+H.

	HF	+δMP2	+δCCSD	+δCCSD(T)	+δCCSDT	+δCCSDT(Q)	ΔE_e[CCSDT(Q)]
cc-pVDZ	−42.70	+12.48	−9.83	+1.66	−0.41	+0.17	[−38.64]
cc-pVTZ	−41.98	+11.87	−10.55	+1.92	−0.55	[+0.17]	[−39.14]
cc-pVQZ	−41.91	+12.01	−10.86	+1.96	[−0.55]	[+0.17]	[−39.17]
cc-pV5Z	−41.90	+12.05	[−10.86]	[+1.96]	[−0.55]	[+0.17]	[−39.12]
cc-pV6Z	−41.90	+12.11	[−10.86]	[+1.96]	[−0.55]	[+0.17]	[−39.06]
CBS LIMIT	[−41.90]	[+12.19]	[−10.86]	[+1.96]	[−0.55]	[+0.17]	[−**38.98**]
ΔE_0(final)	=	ΔE_e[CBS CCSDT(Q)] + $\Delta E_{\rm core}$ + $\Delta E_{\rm relativity}$ + $\Delta E_{\rm ZPVE}$					
	=	-38.98 +0.16 +0.02 +6.89 = **-31.91 kcal mol^{-1}**					

[a]See footnote of A1 for an explanation of the notation used.

Table A7 : Valence focal point analysis of the relative energy (in kcal mol^{-1}) of **ts2** with respect to allene+H.

	HF	+δMP2	+δCCSD	+δCCSD(T)	+δCCSDT	+δCCSDT(Q)	ΔE_e[CCSDT(Q)]
cc-pVDZ	+19.06	+7.66	−12.48	−0.63	−0.80	−0.16	[+12.64]
cc-pVTZ	+19.22	+7.33	−13.14	−0.74	−0.85	[−0.16]	[+11.65]
cc-pVQZ	+19.25	+7.34	−13.39	−0.81	[−0.85]	[−0.16]	[+11.38]
cc-pV5Z	+19.27	+7.38	[−13.39]	[−0.81]	[−0.85]	[−0.16]	[+11.44]
cc-pV6Z	+19.27	+7.41	[−13.39]	[−0.81]	[−0.85]	[−0.16]	[+11.47]
CBS LIMIT	[+19.27]	[+7.45]	[−13.39]	[−0.81]	[−0.85]	[−0.16]	[+**11.52**]
ΔE_0(final)	=	ΔE_e[CBS CCSDT(Q)] + $\Delta E_{\rm core}$ + $\Delta E_{\rm relativity}$ + $\Delta E_{\rm ZPVE}$					
	=	+11.52 +0.07 -0.02 -1.62 = **+9.95 kcal mol^{-1}**					

[a]See footnote of A1 for an explanation of the notation used.

Table A8 : Valence focal point analysis of the relative energy (in kcal mol^{-1}) of **ts5** with respect to allene+H.

	HF	+δMP2	+δCCSD	+δCCSD(T)	+δCCSDT	+δCCSDT(Q)	ΔE_e[CCSDT(Q)]
cc-pVDZ	+7.79	+3.63	−5.86	+0.06	−0.24	−0.11	[+5.27]
cc-pVTZ	+7.46	+2.75	−6.36	−0.02	−0.28	[−0.11]	[+3.45]
cc-pVQZ	+7.48	+2.53	−6.58	−0.06	[−0.28]	[−0.11]	[+2.98]
cc-pV5Z	+7.52	+2.41	[−6.58]	[−0.06]	[−0.28]	[−0.11]	[+2.90]
cc-pV6Z	+7.52	+2.37	[−6.58]	[−0.06]	[−0.28]	[−0.11]	[+2.87]
CBS LIMIT	[+7.52]	[+2.33]	[−6.58]	[−0.06]	[−0.28]	[−0.11]	[+**2.83**]
ΔE_0(final)	=	ΔE_e[CBS CCSDT(Q)] + ΔE_{core} + $\Delta E_{\text{relativity}}$ + ΔE_{ZPVE}					
	=	+2.83 +0.03 -0.01 +1.44 = **+4.29 kcal mol^{-1}**					

[a]See footnote of A1 for an explanation of the notation used.

Table A9 : Valence focal point analysis of the relative energy (in kcal mol^{-1}) of **ts8** with respect to allene+H.

	HF	+δMP2	+δCCSD	+δCCSD(T)	+δCCSDT	+δCCSDT(Q)	ΔE_e[CCSDT(Q)]
cc-pVDZ	+5.90	+2.96	−4.74	+0.11	−0.19	−0.10	[+3.94]
cc-pVTZ	+5.50	+2.18	−5.28	+0.05	−0.22	[−0.10]	[+2.13]
cc-pVQZ	+5.54	+1.97	−5.50	+0.02	[−0.22]	[−0.10]	[+1.70]
cc-pV5Z	+5.58	+1.86	[−5.50]	[+0.02]	[−0.22]	[−0.10]	[+1.63]
cc-pV6Z	+5.58	+1.82	[−5.50]	[+0.02]	[−0.22]	[−0.10]	[+1.59]
CBS LIMIT	[+5.58]	[+1.76]	[−5.50]	[+0.02]	[−0.22]	[−0.10]	[+**1.54**]
ΔE_0(final)	=	ΔE_e[CBS CCSDT(Q)] + ΔE_{core} + $\Delta E_{\text{relativity}}$ + ΔE_{ZPVE}					
	=	+1.54 +0.00 -0.01 +1.13 = **+2.66 kcal mol^{-1}**					

[a]See footnote of A1 for an explanation of the notation used.

Table A10 : Valence focal point analysis of the relative energy (in kcal mol^{-1}) of **ts9** with respect to allene+H.

	HF	+δMP2	+δCCSD	+δCCSD(T)	+δCCSDT	+δCCSDT(Q)	ΔE_e[CCSDT(Q)]
cc-pVDZ	+19.11	−3.42	−3.91	−0.25	−0.15	−0.15	[+11.23]
cc-pVTZ	+18.64	−4.17	−4.27	−0.36	−0.17	[−0.15]	[+9.52]
cc-pVQZ	+18.64	−4.38	−4.40	−0.39	[−0.17]	[−0.15]	[+9.15]
cc-pV5Z	+18.67	−4.51	[−4.40]	[−0.39]	[−0.17]	[−0.15]	[+9.05]
cc-pV6Z	+18.68	−4.56	[−4.40]	[−0.39]	[−0.17]	[−0.15]	[+9.00]
CBS LIMIT	[+18.68]	[−4.64]	[−4.40]	[−0.39]	[−0.17]	[−0.15]	[+**8.93**]
ΔE_0(final)	=	ΔE_e[CBS CCSDT(Q)] + $\Delta E_{\rm core}$ + $\Delta E_{\rm relativity}$ + $\Delta E_{\rm ZPVE}$					
	=	+8.93 +0.02 -0.01 -1.27 = **+7.64 kcal mol^{-1}**					

[a]See footnote of A1 for an explanation of the notation used.

Table A11 : Valence focal point analysis of the relative energy (in kcal mol^{-1}) of **ts14** with respect to allene+H.

	HF	+δMP2	+δCCSD	+δCCSD(T)	+δCCSDT	+δCCSDT(Q)	ΔE_e[CCSDT(Q)]
cc-pVDZ	+14.01	+2.67	−10.69	−0.07	−0.50	−0.07	[+5.36]
cc-pVTZ	+15.16	+1.71	−11.14	−0.20	−0.56	[−0.07]	[+4.89]
cc-pVQZ	+15.25	+1.65	−11.34	−0.25	[−0.56]	[−0.07]	[+4.68]
cc-pV5Z	+15.28	+1.59	[−11.34]	[−0.25]	[−0.56]	[−0.07]	[+4.65]
cc-pV6Z	+15.28	+1.60	[−11.34]	[−0.25]	[−0.56]	[−0.07]	[+4.65]
CBS LIMIT	[+15.28]	[+1.60]	[−11.34]	[−0.25]	[−0.56]	[−0.07]	[+**4.66**]
ΔE_0(final)	=	ΔE_e[CBS CCSDT(Q)] + $\Delta E_{\rm core}$ + $\Delta E_{\rm relativity}$ + $\Delta E_{\rm ZPVE}$					
	=	+4.66 +0.28 +0.00 +3.58 = **+8.52 kcal mol^{-1}**					

[a]See footnote of A1 for an explanation of the notation used.

APPENDIX B

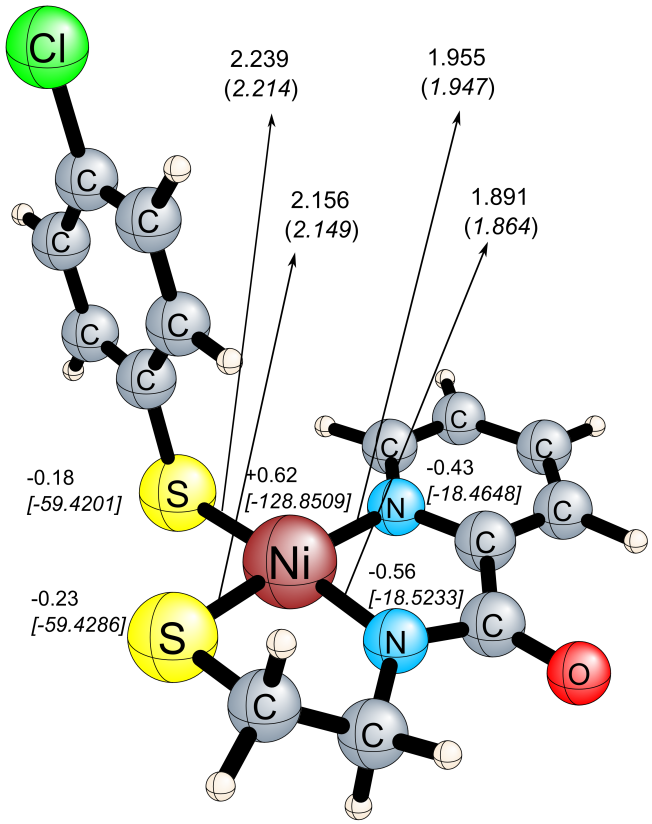

Figure B1 : DFT geometry optimized model of $[Ni(nmp)(SC_6H_4\text{-}p\text{-}Cl)]^-$ (anion of **2**) featuring optimized bond lengths (Å) (crystallographically determined bond lengths in parenthesis), atomic charges and electrostatic potentials [a.u. in brackets for select atoms].

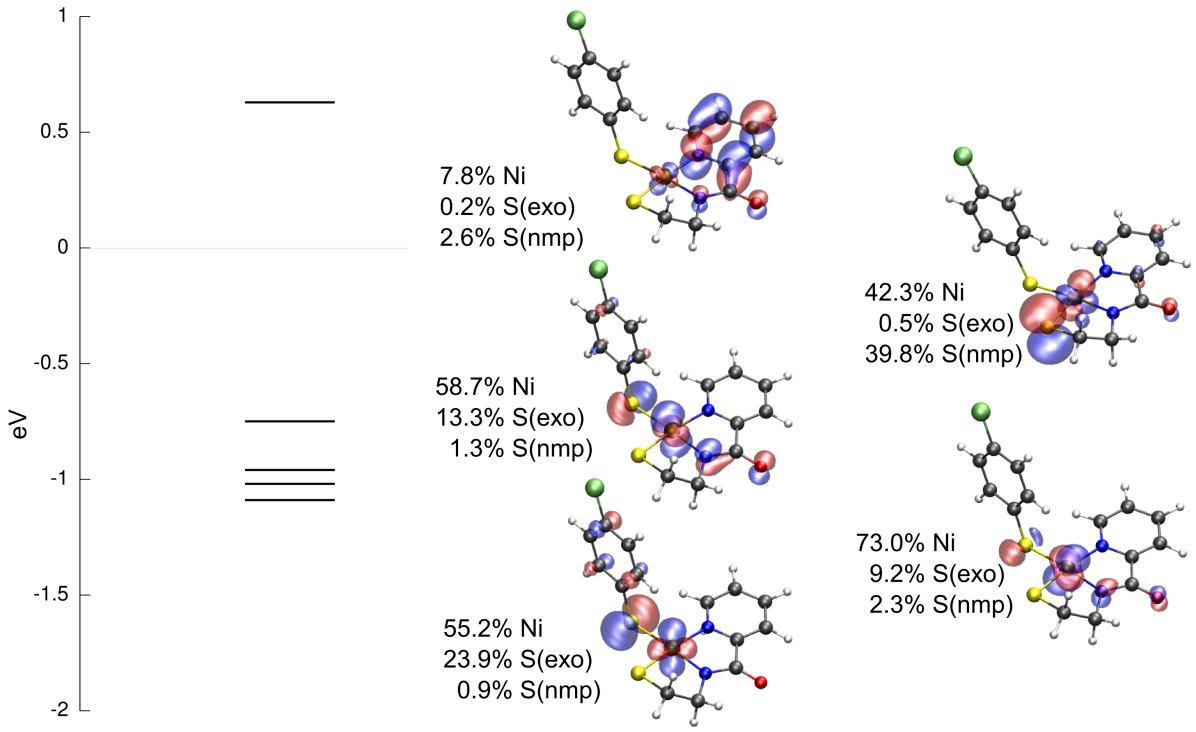

Figure B2 : DFT generated isosurface plots of the frontier MOs of the geometry optimized structure of **2**. In each column, the MOs descend in the order LUMO, HOMO, HOMO-1, HOMO-2, and HOMO-3.

Table B1 : Löwdin Orbital Compositions Derived from the DFT Calculations for Selected Molecular Orbitals of Complex **2**.

MO label	MO	E (eV)	%Ni[a]	%N[b]	%S[c]	Orbital Composition
LUMO[d]	98	0.63	7.8	18.8	2.8	$Ni(d_{x_z})$ – $N_{py}(p_z)$, $N_{am}(p_z)$
HOMO	97	-0.73	42.3	1.3	40.3	$Ni(d_{xz})$ – $S_{nmp}(p_z)$
HOMO-1	96	-0.94	58.7	6.6	14.6	$Ni(d_{yz})$ – $N_{am}(p_z)$, $S_{exo}(p_x)$
HOMO-2	95	-1.00	73.0	4.2	11.5	$Ni(d_{z^2})$/$Ni(d_{yz})$ – $N_{am}(p_z)$, $S_{exo}(p_x)$
HOMO-3	94	-1.07	55.2	1.9	24.8	$Ni(d_{zsuper2})$, $N_{am}(p_z)$, $N_{py}(p_x)$, $S_{exo}(p_x)$
HOMO-4	93	-2.04	36.0	3.2	33.1	$Ni(d_{xz})$ + $S_{nmp}(p_z)$, $N_{am}(p_y)$/$N_{am}(p_x)$/$N_{am}(p_z)$
HOMO-5	92	-2.08	25.9	4.8	14.4	$Ni(d_{xy})$ + $N_{am}(p_y)$/$N_{am}(p_x)$/$N_{am}(p_z)$, $S_{exo}(p_x)$/$S_{exo}(p_y)$
HOMO-6	91	-2.28	42.5	4.4	18.5	$Ni(d_{xy})$ + $N_{am}(p_z)$, $S_{nmp}(p_z)$/$S_{nmp}(p_x)$/$S_{nmp}(p_y)$, $S_{exo}(p_x)$

[a]MO contribution from the Ni AOs. [b]MO contribution from the N AOs of N_{py} and the coordinated $N_{carboxamide}$. [c]MO contribution from the S AOs. The composition is given in order of AO contribution to the MO. [d]The major contributions to the LUMO involves C($p\pi$) AOs from the pyridine ring of nmp (56.8 %). Bonding interactions are represented with a + and antibonding interactions are denoted with a –. The coordinate system used for figuring out the type of AO on Ni, N and S are as follows: z-axis is normal to the square planar ligand field; x-axis is parallel to S_{nmp}–Ni–N_{py}; y-axis is parallel to S_{exo}–Ni–$N_{carboxamide}$.

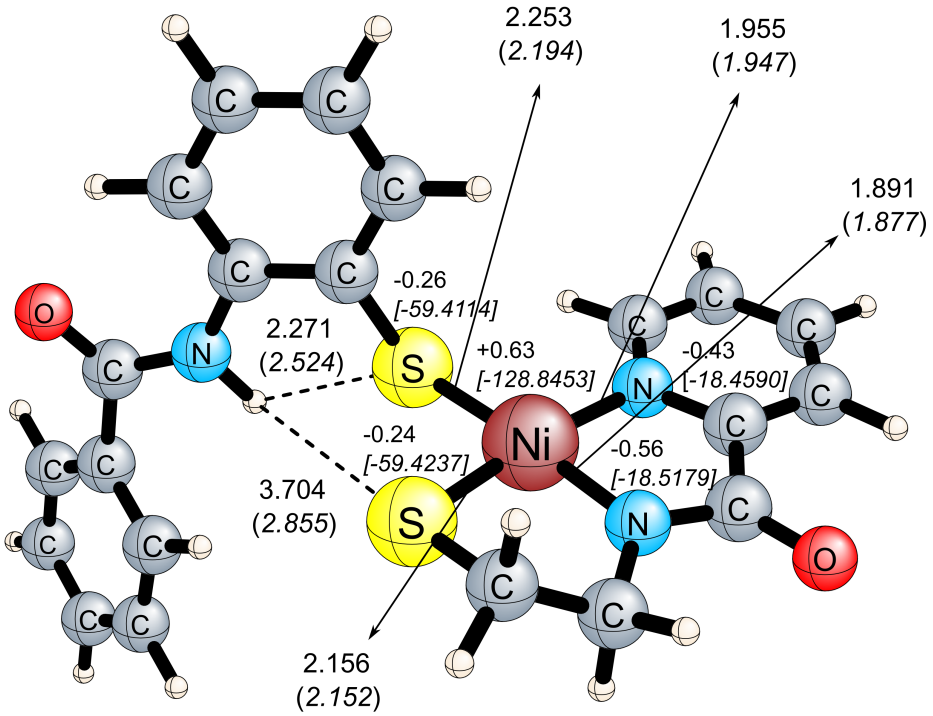

Figure B3 : DFT geometry optimized model of $[Ni(nmp)(S\text{-}o\text{-}babt)]^-$ (anion of **4**) featuring optimized bond lengths (Å) (crystallographically determined bond lengths in parenthesis), atomic charges and electrostatic potentials [a.u. in brackets for select atoms].

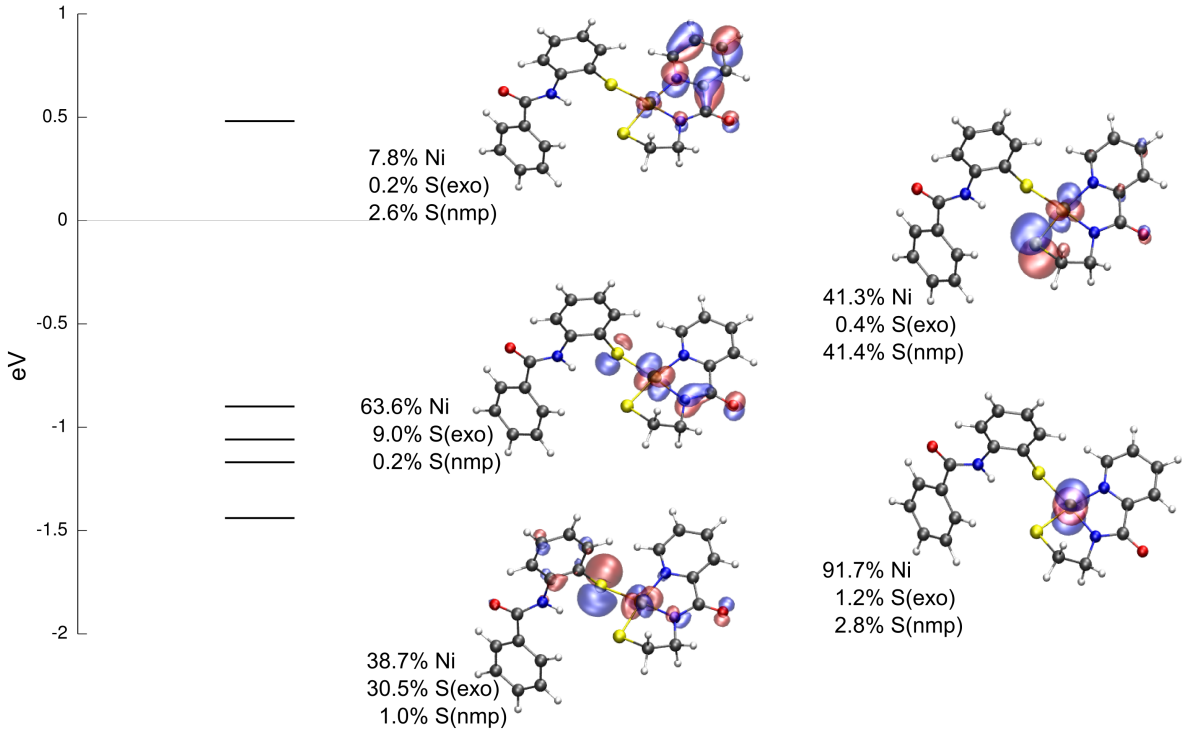

Figure B4 : DFT generated isosurface plots of the frontier MOs of the geometry optimized structure of **4**. In each column, the MOs descend in the order LUMO, HOMO, HOMO-1, HOMO-2, and HOMO-3.

Table B2 : Löwdin Orbital Compositions Derived from the DFT Calculations for Selected Molecular Orbitals of Complex **4**.

MO label	MO	E (eV)	%Ni[a]	%N[b]	%S[c]	Orbital Composition
LUMO[d]	121	0.48	7.8	18.5	2.8	$Ni(d_{xz})$ – $N_{py}(p_z)$, $N_{am}(p_z)$
HOMO	120	-0.88	41.3	1.1	41.8	$Ni(d_{xz})$ – $S_{nmp}(p_z)$
HOMO-1	119	-1.04	63.6	8.1	9.2	$Ni(d_{zy})$ – $N_{am}(p_z)$, $S_{exo}(p_x)$
HOMO-2	118	-1.15	91.7	1.8	4.0	$Ni(d_{z^2})$
HOMO-3	117	-1.42	38.7	3.8	31.5	$Ni(d_{xy})$/$Ni(d_{yz})$, $N_{am}(p_z)$, $S_{exo}(p_x)$
HOMO-4	116	-2.14	33.7	3.0	30.1	$Ni(d_{xz})$/$Ni(d_{xy})$, $N_{am}(p_y)$/$N_{am}(d_x)$, $S_{nmp}(d_z)$/$S_{nmp}(p_y)$, $S_{exo}(p_y)$/$S_{exo}(d_z)$
HOMO-5	115	-2.27	31.3	1.7	13.6	$Ni(d_{xy})$/$Ni(d_{xz})$, $N_{am}(d_z)$/$N_{am}(d_x)$, $S_{nmp}(d_z)$/$S_{nmp}(d_x)$
HOMO-6	114	-2.35	19.4	5.3	16.1	$Ni(d_{xz})$/$Ni(d_{yz})$, $N_{am}(d_z)$/$N_{am}(p_y)$/$N_{am}(d_x)$, $S_{nmp}(d_z)$, $S_{exo}(d_x)$/$S_{exo}(p_y)$

[a]MO contribution from the Ni AOs. [b]MO contribution from the N AOs of N_{py} and the coordinated $N_{carboxamide}$. [c]MO contribution from the S AOs. The composition is given in order of AO contribution to the MO. [d]The major contributions to the LUMO involves C($p\pi$) AOs from the pyridine ring of nmp (55.7 %). Bonding interactions are represented with a + and antibonding interactions are denoted with a –. The coordinate system used for figuring out the type of AO on Ni, N and S are as follows: z-axis is normal to the square planar ligand field; x-axis is parallel to S_{nmp}–Ni–N_{py}; y-axis is parallel to S_{exo}–Ni–$N_{carboxamide}$.

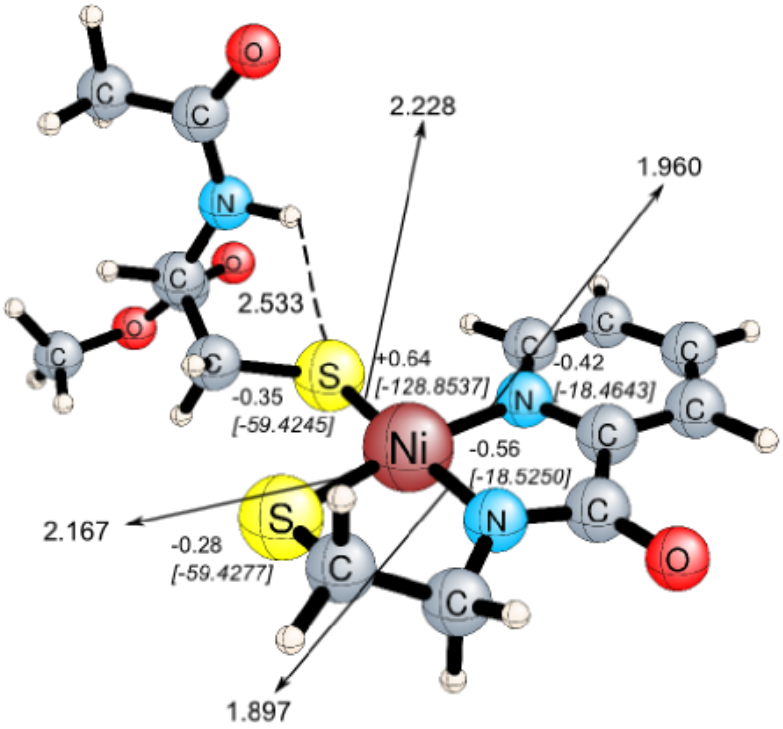

Figure B5 : DFT geometry optimized model of $[Ni(nmp)(S\text{-}NAc)]^-$ (anion of **6**) featuring optimized bond lengths (Å), atomic charges and electrostatic potentials [a.u. in brackets for select atoms].

APPENDIX C

Table C1a : Deviations of $Ni(CO)_4$ bond parameter from experimental values

DFT functional	δ DZP[a] Ni-C	δ cc-pVDZ[a] Ni-C	δ cc-pVTZ[a] Ni-C	δ cc-pVQZ[a] Ni-C	MAD[b] Ni-C
GGA					
BLYP	0.009	0.014	0.015	0.014	0.013
BP86	-0.012	-0.009	-0.010	-0.011	0.010
B97-D	0.005	0.009	0.007	0.006	0.007
HCTH147	-0.005	-0.002	-0.004	-0.005	0.004
HCTH407	-0.007	-0.005	-0.006	-0.007	0.006
mGGA					
M06-L	-0.000	0.001	-0.002	-0.004	0.002
VSXC	0.021	0.025	0.023	0.022	0.023
hGGA					
BHLYP	0.010	0.016	0.015	0.014	0.014
MPW1K	-0.015	-0.012	-0.013	-0.014	0.013
BHandH	-0.006	-0.001	-0.002	-0.003	0.003
MPW1PW91	-0.016	-0.012	-0.014	-0.014	0.014
MPW1PBE	-0.018	-0.014	-0.016	-0.017	0.016
B1LYP	0.008	0.013	0.013	0.012	0.011
PBE1PBE	-0.017	-0.014	-0.016	-0.016	0.016
MPW1LYP	0.006	0.012	0.012	0.011	0.010
B98	-0.001	0.003	0.002	0.001	0.002
X3LYP	0.002	0.007	0.007	0.006	0.005
B97-1	-0.000	0.003	0.003	0.002	0.002
B97-2	-0.007	-0.004	-0.005	-0.006	0.005
MPW3PBE	-0.017	-0.013	-0.014	-0.015	0.015
B3LYP	0.003	0.008	0.008	0.007	0.006
B3PW91	-0.014	-0.011	-0.012	-0.013	0.013
B3P86	-0.018	-0.015	-0.016	-0.017	0.017
O3LYP	-0.007	-0.004	-0.005	-0.006	0.005
hmGGA					
M06-HF	0.091	0.092	0.088	0.090	0.090
M05-2X	0.033	0.039	0.038	0.037	0.037
M06-2X	0.060	0.068	0.067	0.067	0.066
MPWB1K	-0.011	-0.008	-0.009	-0.010	0.009
BB1K	-0.010	-0.007	-0.008	-0.009	0.009
M05	0.007	0.012	0.013	0.010	0.011
B1B95	-0.011	-0.008	-0.009	-0.010	0.009
M06	0.006	0.012	0.013	0.011	0.010
TPSSH	-0.011	-0.008	-0.010	-0.011	0.010
LC-hGGA					
CAM-B3LYP	-0.007	-0.002	-0.001	-0.002	0.003
LC-ωPBE	-0.021	-0.019	-0.019	-0.020	0.020
Experiment [c]	1.838	1.838	1.838	1.838	

[a] δ DZP values are calculated as optimized DZP bond lengths minus the experimental value. δ cc-pVXZ (X = D,T,Q) values are calculated similarly.

[b] Mean absolute deviation (MAD) is the average of deviations across the four basis sets.

[c] Hedberg, L.; Iijima, T.; Hedberg, K. *J. Chem. Phys.* **1979,** *70,* 3224–3229.

Table C2a : Deviations of $Fe(CO)_5$ bond parameters from experimental values

DFT	δ DZP[a]		δ cc-pVDZ[a]		δ cc-pVTZ[a]		δ cc-pVQZ[a]		MAD[b]	
functional	Fe-C^{ax}	Fe-C^{eq}	Fe-C^{ax}	Fe-C^{eq}	Fe-C^{ax}	Fe-C^{eq}	Fe-C^{ax}	Fe-C^{eq}	Fe-C^{ax}	Fe-C^{eq}
GGA										
BLYP	0.019	-0.000	0.027	0.006	0.024	0.005	0.024	0.005	0.024	0.004
BP86	-0.002	-0.022	0.004	-0.017	0.002	-0.018	0.001	-0.018	0.002	0.019
B97-D	0.005	-0.015	0.011	-0.010	0.008	-0.011	0.007	-0.011	0.008	0.012
HCTH147	-0.008	-0.026	-0.002	-0.022	-0.005	-0.023	-0.006	-0.023	0.005	0.024
HCTH407	-0.013	-0.031	-0.007	-0.026	-0.010	-0.027	-0.011	-0.028	0.010	0.028
mGGA										
M06-L	0.009	-0.014	0.013	-0.011	0.009	-0.015	0.008	-0.015	0.010	0.014
VSXC	0.028	0.008	0.034	0.012	0.031	0.010	0.030	0.010	0.031	0.010
hGGA										
BHLYP	0.047	-0.005	0.058	0.002	0.052	0.000	0.052	-0.000	0.052	0.002
MPW1K	0.005	-0.033	0.012	-0.028	0.007	-0.030	0.007	-0.030	0.008	0.030
BHandH	0.023	-0.021	0.032	-0.016	0.027	-0.017	0.026	-0.018	0.027	0.018
MPW1PW91	-0.004	-0.032	0.002	-0.027	-0.001	-0.029	-0.001	-0.029	0.002	0.029
MPW1PBE	-0.006	-0.034	-0.000	-0.030	-0.003	-0.031	-0.004	-0.031	0.003	0.032
B1LYP	0.023	-0.007	0.032	-0.000	0.029	-0.002	0.028	-0.002	0.028	0.003
PBE1PBE	-0.006	-0.034	-0.000	-0.030	-0.004	-0.031	-0.004	-0.031	0.004	0.032
MPW1LYP	0.022	-0.008	0.031	-0.001	0.028	-0.002	0.027	-0.003	0.027	0.004
B98	0.009	-0.018	0.016	-0.013	0.012	-0.014	0.012	-0.015	0.012	0.015
X3LYP	0.016	-0.012	0.024	-0.006	0.021	-0.007	0.020	-0.007	0.020	0.008
B97-1	0.009	-0.017	0.017	-0.012	0.013	-0.014	0.012	-0.014	0.013	0.014
B97-2	-0.002	-0.028	0.004	-0.023	0.000	-0.025	-0.000	-0.025	0.002	0.025
MPW3PBE	-0.006	-0.032	-0.000	-0.027	-0.003	-0.028	-0.004	-0.029	0.003	0.029
B3LYP	0.016	-0.011	0.024	-0.005	0.021	-0.006	0.020	-0.006	0.020	0.007
B3PW91	-0.004	-0.030	0.002	-0.025	-0.001	-0.026	-0.001	-0.027	0.002	0.027
B3P86	-0.007	-0.033	-0.001	-0.028	-0.004	-0.029	-0.004	-0.030	0.004	0.030
O3LYP	-0.007	-0.029	-0.002	-0.025	-0.005	-0.026	-0.005	-0.027	0.005	0.027
hmGGA										
M06-HF	0.157	0.022	0.185	0.033	0.153	0.018	0.154	0.013	0.162	0.021
M05-2X	0.046	-0.003	0.058	0.004	0.048	-0.002	0.047	-0.003	0.050	0.003
M06-2X	0.076	0.013	0.091	0.021	0.075	0.012	0.074	0.011	0.079	0.014
MPWB1K	0.007	-0.031	0.014	-0.026	0.011	-0.027	0.010	-0.028	0.011	0.028
BB1K	0.006	-0.030	0.014	-0.026	0.010	-0.027	0.009	-0.027	0.010	0.027
M05	0.001	-0.016	0.006	-0.012	0.004	-0.012	0.002	-0.014	0.003	0.013
B1B95	-0.001	-0.030	0.005	-0.026	0.002	-0.026	0.002	-0.026	0.003	0.027
M06	0.009	-0.011	0.014	-0.007	0.015	-0.005	0.014	-0.006	0.013	0.007
TPSSH	0.004	-0.021	0.009	-0.017	0.006	-0.019	0.005	-0.019	0.006	0.019
LC-hGGA										
CAM-B3LYP	0.008	-0.021	0.017	-0.015	0.014	-0.015	0.013	-0.016	0.013	0.017
LC-ωPBE	-0.016	-0.038	-0.010	-0.033	-0.012	-0.033	-0.013	-0.034	0.013	0.035
Experiment[c]	1.807	1.827	1.807	1.827	1.807	1.827	1.807	1.827		

[a,b] See C1a footnotes.

[c] Beagley, B.; Schmidling, D. G. *J. Mol. Struct.* **1974,** *22,* 466–468.

Table C3a : Deviations of $Cr(CO)_6$ bond parameters from experimental values

DFT functional	δ DZP[a] Cr-C	δ cc-pVDZ[a] Cr-C	δ cc-pVTZ[a] Cr-C	δ cc-pVQZ[a] Cr-C	MAD[b] Cr-C
GGA					
BLYP	0.017	0.017	0.020	0.020	0.019
BP86	-0.007	-0.008	-0.006	-0.005	0.006
B97-D	0.005	0.004	0.007	0.007	0.006
HCTH147	-0.011	-0.012	-0.009	-0.009	0.010
HCTH407	-0.016	-0.017	-0.014	-0.014	0.015
mGGA					
M06-L	0.008	0.005	0.005	0.007	0.006
VSXC	0.032	0.029	0.032	0.032	0.031
hGGA					
BHLYP	0.019	0.019	0.021	0.021	0.020
MPW1K	-0.014	-0.017	-0.014	-0.013	0.014
BHandH	0.001	-0.001	0.002	0.002	0.002
MPW1PW91	-0.014	-0.017	-0.014	-0.013	0.014
MPW1PBE	-0.017	-0.019	-0.016	-0.016	0.017
B1LYP	0.014	0.014	0.017	0.017	0.015
PBE1PBE	-0.017	-0.019	-0.016	-0.016	0.017
MPW1LYP	0.013	0.013	0.016	0.016	0.014
B98	-0.000	-0.001	0.000	0.001	0.001
X3LYP	0.008	0.008	0.011	0.011	0.009
B97-1	0.000	-0.001	0.001	0.001	0.001
B97-2	-0.010	-0.012	-0.010	-0.009	0.010
MPW3PBE	-0.015	-0.017	-0.014	-0.014	0.015
B3LYP	0.009	0.009	0.011	0.012	0.010
B3PW91	-0.013	-0.015	-0.012	-0.011	0.013
B3P86	-0.016	-0.018	-0.015	-0.014	0.016
O3LYP	-0.014	-0.016	-0.013	-0.013	0.014
hmGGA					
M06-HF	0.036	0.040	0.029	0.026	0.033
M05-2X	0.015	0.014	0.014	0.015	0.014
M06-2X	0.031	0.030	0.028	0.028	0.029
MPWB1K	-0.012	-0.015	-0.011	-0.011	0.012
BB1K	-0.012	-0.014	-0.011	-0.010	0.012
M05	-0.004	-0.007	-0.004	-0.004	0.005
B1B95	-0.012	-0.015	-0.011	-0.010	0.012
M06	0.002	-0.001	0.004	0.005	0.003
TPSSH	-0.003	-0.005	-0.003	-0.002	0.003
LC-hGGA					
CAM-B3LYP	-0.001	-0.002	0.002	0.003	0.002
LC-ωPBE	-0.023	-0.027	-0.022	-0.021	0.023
Experiment[c]	1.914	1.914	1.914	1.914	

[a,b] See C1a footnotes.

[c] Jost, A.; Rees, B.; Yelon, W. B. *Acta Cryst.* **1975,** *B31,* 2649–2658.

Table C4a : Deviations of $Co_2(CO)_8$ bond parameters from experimental values

DFT	δ DZP[a]				δ cc-pVDZ[a]				δ cc-pVTZ[a]				δ cc-pVQZ[a]				MAD[b]			
functional	Co-Co	Co-C^b	Co-C^{2t}	Co-C^{4t}	Co-Co	Co-C^b	Co-C^{2t}	Co-C^{4t}	Co-Co	Co-C^b	Co-C^{2t}	Co-C^{4t}	Co-Co	Co-C^b	Co-C^{2t}	Co-C^{4t}	Co-Co	Co-C^b	Co-C^{2t}	Co-C^{4t}
GGA																				
BLYP	0.071	0.043	0.012	0.003	0.078	0.047	0.017	0.009	0.077	0.048	0.018	0.008					0.075	0.046	0.016	0.007
BP86	0.022	0.018	-0.011	-0.019	0.028	0.022	-0.007	-0.014	0.025	0.021	-0.008	-0.017					0.025	0.020	0.009	0.017
B97-D	0.020	0.030	0.005	-0.008	0.027	0.034	0.009	-0.003	0.024	0.033	0.008	-0.006					0.024	0.032	0.007	0.006
HCTH147	0.026	0.018	-0.010	-0.020	0.034	0.021	-0.006	-0.015	0.030	0.020	-0.007	-0.018	0.033	0.019	-0.007	-0.019	0.031	0.019	0.007	0.018
HCTH407	0.017	0.013	-0.014	-0.024	0.026	0.016	-0.010	-0.020	0.020	0.014	-0.011	-0.024	0.023	0.014	-0.011	-0.024	0.021	0.014	0.011	0.023
Meta GGA																				
M06-L	-0.003	0.022	-0.001	-0.007	0.008	0.023	0.002	-0.003	-0.001	0.021	-0.002	-0.010	-0.002	0.021	-0.003	-0.010	0.004	0.022	0.002	0.007
VSXC	-0.032	0.051	0.024	0.027	-0.029	0.047	0.029	0.031	-0.032	0.048	0.028	0.028					0.031	0.049	0.027	0.029
Hybrid GGA																				
BHLYP	0.005	0.001	0.012	0.007	0.018	0.007	0.016	0.012	0.017	0.008	0.017	0.008	0.020	0.008	0.018	0.009	0.015	0.006	0.016	0.009
MPW1K	-0.041	-0.020	-0.018	-0.025	-0.033	-0.016	-0.015	-0.021	-0.035	-0.016	-0.016	-0.025	-0.032	-0.016	-0.015	-0.025	0.035	0.017	0.016	0.024
BHandH	-0.024	-0.013	-0.007	-0.013	-0.013	-0.008	-0.003	-0.008	-0.015	-0.008	-0.003	-0.012	-0.012	-0.008	-0.003	-0.012	0.016	0.009	0.004	0.011
MPW1PW91	-0.021	-0.007	-0.018	-0.026	-0.014	-0.004	-0.014	-0.022	-0.016	-0.004	-0.015	-0.026	-0.013	-0.004	-0.015	-0.026	0.016	0.005	0.015	0.025
MPW1PBE	-0.025	-0.009	-0.020	-0.028	-0.018	-0.006	-0.017	-0.024	-0.020	-0.006	-0.018	-0.028	-0.017	-0.006	-0.017	-0.028	0.020	0.007	0.018	0.027
B1LYP	0.031	0.017	0.009	-0.000	0.042	0.022	0.014	0.005	0.040	0.023	0.014	0.003	0.043	0.023	0.015	0.003	0.039	0.021	0.013	0.003
PBE1PBE	-0.025	-0.009	-0.020	-0.029	-0.017	-0.006	-0.017	-0.025	-0.020	-0.006	-0.018	-0.028	-0.017	-0.007	-0.017	-0.028	0.020	0.007	0.018	0.028
MPW1LYP	0.029	0.016	0.007	-0.002	0.040	0.021	0.012	0.004	0.038	0.022	0.013	0.002	0.042	0.021	0.013	0.002	0.037	0.020	0.011	0.003
B98	0.011	0.008	-0.003	-0.012	0.019	0.013	0.001	-0.007	0.017	0.012	0.001	-0.011	0.020	0.012	0.001	-0.011	0.017	0.011	0.002	0.010
X3LYP	0.025	0.014	0.003	-0.007	0.035	0.019	0.008	-0.001	0.033	0.019	0.008	-0.003	0.037	0.019	0.009	-0.003	0.033	0.018	0.007	0.003
B97-1	0.011	0.010	-0.003	-0.011	0.018	0.014	0.001	-0.006	0.016	0.013	0.001	-0.010	0.019	0.013	0.001	-0.010	0.016	0.012	0.002	0.009
B97-2	-0.007	-0.000	-0.011	-0.021	0.002	0.003	-0.007	-0.017	-0.002	0.003	-0.008	-0.021	0.001	0.002	-0.008	-0.021	0.003	0.002	0.009	0.020
MPW3PBE	-0.015	-0.004	-0.018	-0.027	-0.008	-0.001	-0.015	-0.023	-0.011	-0.001	-0.015	-0.026	-0.007	-0.001	-0.015	-0.026	0.010	0.002	0.016	0.025
B3LYP	0.029	0.016	0.004	-0.006	0.039	0.021	0.009	0.000	0.037	0.022	0.009	-0.002	0.040	0.022	0.009	-0.003	0.036	0.020	0.008	0.003
B3PW91	-0.011	-0.002	-0.016	-0.025	-0.003	0.002	-0.012	-0.020	-0.006	0.001	-0.013	-0.024	-0.003	0.001	-0.012	-0.024	0.006	0.002	0.013	0.023
B3P86	-0.014	-0.006	-0.019	-0.028	-0.007	-0.003	-0.015	-0.024	-0.010	-0.003	-0.016	-0.027	-0.006	-0.003	-0.016	-0.027	0.009	0.004	0.017	0.026
O3LYP	-0.030	-0.016	-0.033	-0.043	-0.023	-0.013	-0.029	-0.039	-0.026	-0.014	-0.030	-0.042	-0.023	-0.014	-0.030	-0.042	0.026	0.014	0.030	0.042
Hybrid Meta GGA																				
M06-HF	0.133	0.092	0.126	0.095	0.150	0.127	0.129	0.101	0.147	0.109	0.125	0.094	0.151	0.113	0.132	0.089	0.145	0.110	0.128	0.095
M05-2X	0.026	0.008	0.029	0.015	0.039	0.016	0.033	0.020	0.037	0.015	0.033	0.013	0.039	0.015	0.033	0.013	0.035	0.013	0.032	0.015
M06-2X	0.046	0.026	0.048	0.041	0.064	0.033	0.052	0.049	0.061	0.033	0.051	0.039	0.064	0.033	0.052	0.039	0.059	0.031	0.051	0.042
MPWB1K	-0.060	-0.023	-0.015	-0.022	-0.051	-0.020	-0.012	-0.018	-0.055	-0.020	-0.012	-0.022	-0.052	-0.020	-0.011	-0.022	0.054	0.021	0.013	0.021
BB1K	-0.057	-0.020	-0.014	-0.022	-0.048	-0.018	-0.011	-0.018	-0.052	-0.018	-0.011	-0.021	-0.049	-0.018	-0.010	-0.022	0.052	0.018	0.012	0.021
M05	-0.008	0.006	0.009	-0.015	0.003	0.008	0.016	-0.010	-0.001	0.010	0.016	-0.013	-0.002	0.009	0.016	-0.014	0.004	0.008	0.014	0.013
B1B95	-0.041	-0.010	-0.014	-0.023	-0.033	-0.008	-0.010	-0.019	-0.037	-0.008	-0.011	-0.022	-0.034	-0.008	-0.010	-0.022	0.036	0.009	0.011	0.021
M06	0.003	0.008	0.010	-0.008	0.010	0.009	0.015	-0.004	0.009	0.013	0.017	-0.003	0.010	0.013	0.017	-0.004	0.008	0.011	0.015	0.005
TPSSH	-0.014	0.007	-0.010	-0.016	-0.008	0.009	-0.007	-0.012	-0.012	0.008	-0.008	-0.016	-0.009	0.008	-0.008	-0.016	0.011	0.008	0.008	0.015
LC Hybrid GGA																				
CAM-B3LYP	-0.014	-0.009	-0.004	-0.014	-0.002	-0.005	0.001	-0.008	-0.005	-0.004	0.002	-0.010	-0.002	-0.004	0.002	-0.010	0.006	0.005	0.002	0.011
LC-ωPBE	-0.051	-0.021	-0.021	-0.031	-0.043	-0.018	-0.017	-0.026	-0.047	-0.019	-0.018	-0.029					0.047	0.019	0.019	0.029
Experiment [c]	2.528	1.939	1.816	1.832	2.528	1.939	1.816	1.832	2.528	1.939	1.816	1.832	2.528	1.939	1.816	1.832				

[a,b] See C1a footnotes.

[a] Leung, P. C.; Coppens, P. *Acta Cryst.* **1983,** *B39,* 535–542

Table C5a : Deviations of $Fe_2(CO)_9$ bond parameters from experimental values

DFT	δ DZP[a]			δ cc-pVDZ[a]			δ cc-pVTZ[a]			δ cc-pVQZ[a]			MAD[b]		
functional	Fe-Fe	Fe-C^b	Fe-C^t	Fe-Fe	Fe-C^b	Fe-C^t	Fe-Fe	Fe-C^b	Fe-C^t	Fe-Fe	Fe-C^b	Fe-C^t	Fe-Fe	Fe-C^b	Fe-C^t
GGA															
BLYP	0.043	0.018	0.003	0.052	0.024	0.011	0.049	0.024	0.008	0.052	0.024	0.008	0.049	0.022	0.007
BP86	-0.004	-0.010	-0.019	0.003	-0.006	-0.012	-0.001	-0.006	-0.016	0.001	-0.006	-0.016	0.002	0.007	0.016
B97-D	0.013	0.004	-0.009	0.021	0.009	-0.001	0.017	0.008	-0.005	0.019	0.007	-0.006	0.018	0.007	0.005
HCTH147	-0.007	-0.012	-0.023	0.002	-0.007	-0.016	-0.004	-0.009	-0.020	-0.001	-0.009	-0.021	0.004	0.009	0.020
HCTH407	-0.019	-0.018	-0.028	-0.010	-0.015	-0.021	-0.017	-0.017	-0.026	-0.014	-0.017	-0.026	0.015	0.017	0.025
Meta GGA															
M06-L	-0.008	-0.006	-0.011	-0.002	-0.005	-0.004	-0.011	-0.007	-0.012	-0.009	-0.006	-0.012	0.007	0.006	0.010
VSXC	0.038	0.018	0.018	0.037	0.015	0.026	0.036	0.018	0.020	0.038	0.018	0.020	0.037	0.017	0.021
Hybrid GGA															
BHLYP	-0.021	-0.020	0.001	-0.008	-0.012	0.009	-0.014	-0.014	0.004	-0.011	-0.014	0.004	0.014	0.015	0.004
MPW1K	-0.064	-0.046	-0.031	-0.057	-0.043	-0.025	-0.061	-0.044	-0.030	-0.059	-0.043	-0.029	0.060	0.044	0.029
BHandH	-0.050	-0.038	-0.019	-0.039	-0.031	-0.011	-0.045	-0.033	-0.016	-0.042	-0.032	-0.016	0.044	0.034	0.015
MPW1PW91	-0.044	-0.035	-0.031	-0.038	-0.032	-0.024	-0.042	-0.032	-0.028	-0.039	-0.032	-0.028	0.041	0.033	0.028
MPW1PBE	-0.048	-0.037	-0.033	-0.042	-0.034	-0.026	-0.046	-0.035	-0.031	-0.043	-0.035	-0.031	0.045	0.035	0.030
B1LYP	0.005	-0.007	-0.005	0.016	-0.000	0.003	0.012	-0.001	-0.001	0.014	-0.001	-0.000	0.012	0.002	0.002
PBE1PBE	-0.050	-0.038	-0.033	-0.043	-0.035	-0.027	-0.047	-0.036	-0.031	-0.045	-0.035	-0.031	0.046	0.036	0.030
MPW1LYP	0.003	-0.008	-0.006	0.014	-0.002	0.002	0.010	-0.003	-0.002	0.012	-0.002	-0.001	0.010	0.004	0.003
B98	-0.016	-0.018	-0.017	-0.007	-0.013	-0.009	-0.013	-0.015	-0.014	-0.010	-0.015	-0.014	0.011	0.015	0.013
X3LYP	-0.001	-0.011	-0.010	0.009	-0.005	-0.002	0.005	-0.006	-0.006	0.007	-0.005	-0.006	0.005	0.007	0.006
B97-1	-0.016	-0.016	-0.016	-0.008	-0.012	-0.008	-0.013	-0.014	-0.014	-0.011	-0.014	-0.014	0.012	0.014	0.013
B97-2	-0.034	-0.029	-0.026	-0.026	-0.025	-0.020	-0.031	-0.026	-0.024	-0.028	-0.026	-0.024	0.030	0.026	0.024
MPW3PBE	-0.039	-0.032	-0.031	-0.033	-0.029	-0.024	-0.037	-0.030	-0.028	-0.034	-0.029	-0.028	0.036	0.030	0.028
B3LYP	0.003	-0.008	-0.009	0.013	-0.002	-0.001	0.009	-0.003	-0.005	0.011	-0.003	-0.005	0.009	0.004	0.005
B3PW91	-0.035	-0.030	-0.028	-0.028	-0.026	-0.022	-0.032	-0.027	-0.026	-0.030	-0.026	-0.026	0.031	0.027	0.025
B3P86	-0.040	-0.034	-0.031	-0.033	-0.030	-0.025	-0.037	-0.031	-0.029	-0.034	-0.031	-0.029	0.036	0.032	0.029
O3LYP	-0.028	-0.025	-0.028	-0.022	-0.022	-0.021	-0.027	-0.024	-0.026	-0.024	-0.023	-0.026	0.025	0.024	0.025
Hybrid Meta GGA															
M06-HF	-0.046	0.010	0.056	-0.027	0.041	0.071	-0.057	0.015	0.050	-0.052	0.014	0.049	0.045	0.020	0.056
M05-2X	-0.025	-0.020	0.000	-0.009	-0.008	0.010	-0.020	-0.013	0.001	-0.017	-0.013	0.000	0.018	0.013	0.003
M06-2X	-0.006	-0.002	0.021	0.012	0.011	0.031	-0.004	0.002	0.019	-0.001	0.004	0.019	0.006	0.005	0.023
MPWB1K	-0.074	-0.051	-0.029	-0.068	-0.049	-0.022	-0.072	-0.050	-0.026	-0.070	-0.049	-0.026	0.071	0.050	0.026
BB1K	-0.070	-0.049	-0.028	-0.065	-0.047	-0.022	-0.069	-0.048	-0.026	-0.066	-0.047	-0.026	0.068	0.048	0.025
M05	-0.044	-0.028	-0.017	-0.038	-0.029	-0.009	-0.043	-0.027	-0.014	-0.043	-0.029	-0.015	0.042	0.028	0.014
B1B95	-0.055	-0.040	-0.028	-0.050	-0.038	-0.022	-0.054	-0.039	-0.025	-0.051	-0.038	-0.025	0.052	0.039	0.025
M06	-0.026	-0.023	-0.011	-0.022	-0.022	-0.003	-0.020	-0.018	-0.005	-0.019	-0.018	-0.006	0.022	0.020	0.006
TPSSH	-0.024	-0.020	-0.019	-0.020	-0.018	-0.012	-0.024	-0.019	-0.017	-0.021	-0.018	-0.017	0.022	0.019	0.016
LC Hybrid GGA															
CAM-B3LYP	-0.038	-0.036	-0.017	-0.028	-0.031	-0.009	-0.032	-0.031	-0.012	-0.029	-0.031	-0.012	0.032	0.032	0.013
LC-ωPBE	-0.071	-0.053	-0.034	-0.066	-0.052	-0.026	-0.069	-0.051	-0.031	-0.067	-0.051	-0.030	0.068	0.052	0.030
Experiment [c]	2.523	2.016	1.838	2.523	2.016	1.838	2.523	2.016	1.838	2.523	2.016	1.838			

[a,b] See C1a footnotes.

[a] Cotton, F. A.; Troup, J. M. *J. Chem. Soc., Dalton Trans.* **1974,** 800–802.

Table C6a : Deviations of $Mn_2(CO)_{10}$ bond parameters from experimental values

DFT	δ DZP[a]			δ cc-pVDZ[a]			δ cc-pVTZ[a]			δ cc-pVQZ[a]			MAD[b]		
functional	Mn-Mn	Mn-C^{ax}	Mn-C^{eq}	Mn-Mn	Mn-C^{ax}	Mn-C^{eq}	Mn-Mn	Mn-C^{ax}	Mn-C^{eq}	Mn-Mn	Mn-C^{ax}	Mn-C^{eq}	Mn-Mn	Mn-C^{ax}	Mn-C^{eq}
GGA															
BLYP	0.090	0.022	-0.002	0.079	0.028	0.002	0.116	0.025	0.003	0.124	0.025	0.002	0.102	0.025	0.002
BP86	-0.022	-0.000	-0.022	-0.021	0.004	-0.020	-0.003	0.001	-0.020	0.006	0.001	-0.020	0.013	0.002	0.021
B97-D	0.011	0.009	-0.018	0.012	0.014	-0.016	0.027	0.011	-0.015	0.034	0.010	-0.015	0.021	0.011	0.016
HCTH147	0.060	-0.011	-0.028	0.054	-0.007	-0.026	0.084	-0.010	-0.025	0.094	-0.010	-0.026	0.073	0.009	0.026
HCTH407	0.070	-0.017	-0.032	0.054	-0.007	-0.026	0.098	-0.017	-0.029	0.107	-0.017	-0.030	0.082	0.015	0.029
mGGA															
M06-L	-0.076	0.008	-0.009	-0.037	0.012	-0.008	-0.043	0.006	-0.010	-0.038	0.005	-0.009	0.048	0.008	0.009
VSXC	-0.004	0.038	0.010	0.028	0.046	0.011	0.018	0.040	0.012	0.031	0.040	0.012	0.020	0.041	0.011
hGGA															
BHLYP	0.036	0.029	0.008	0.056	0.038	0.015	0.068	0.031	0.013	0.073	0.030	0.012	0.058	0.032	0.012
MPW1K	-0.074	-0.006	-0.025	-0.052	-0.002	-0.022	-0.050	-0.007	-0.023	-0.042	-0.008	-0.023	0.054	0.006	0.023
BHandH	-0.024	0.009	-0.011	-0.003	0.016	-0.006	0.003	0.010	-0.008	0.010	0.009	-0.008	0.010	0.011	0.008
MPW1PW91	-0.067	-0.010	-0.028	-0.052	-0.006	-0.026	-0.044	-0.010	-0.026	-0.036	-0.010	-0.026	0.050	0.009	0.026
MPW1PBE	-0.062	-0.011	-0.030	-0.051	-0.007	-0.027	-0.041	-0.010	-0.027	-0.032	-0.011	-0.027	0.046	0.010	0.028
B1LYP	0.042	0.017	-0.003	0.048	0.023	0.002	0.071	0.019	0.002	0.077	0.018	0.001	0.059	0.019	0.002
PBE1PBE	-0.080	-0.012	-0.031	-0.063	-0.008	-0.029	-0.058	-0.012	-0.028	-0.050	-0.013	-0.029	0.063	0.011	0.029
MPW1LYP	0.033	0.016	-0.004	0.039	0.023	0.001	0.062	0.019	0.001	0.068	0.018	0.000	0.051	0.019	0.002
B98	-0.009	0.004	-0.015	-0.000	0.009	-0.012	0.012	0.005	-0.013	0.020	0.004	-0.012	0.010	0.005	0.013
X3LYP	0.021	0.011	-0.009	0.027	0.017	-0.005	0.048	0.013	-0.005	0.055	0.012	-0.005	0.038	0.013	0.006
B97-1	-0.019	0.005	-0.014	-0.006	0.010	-0.011	0.004	0.005	-0.012	0.011	0.005	-0.012	0.010	0.006	0.012
B97-2	-0.019	-0.009	-0.025	-0.008	-0.006	-0.023	0.005	-0.009	-0.023	0.014	-0.010	-0.024	0.011	0.009	0.024
MPW3PBE	-0.074	-0.012	-0.030	-0.059	-0.009	-0.028	-0.053	-0.012	-0.028	-0.044	-0.013	-0.029	0.057	0.011	0.029
B3LYP	0.030	0.011	-0.009	0.034	0.017	-0.004	0.057	0.014	-0.004	0.064	0.013	-0.005	0.046	0.014	0.006
B3PW91	-0.049	-0.009	-0.027	-0.038	-0.005	-0.025	-0.028	-0.008	-0.025	-0.019	-0.009	-0.025	0.033	0.008	0.026
B3P86	-0.065	-0.011	-0.031	-0.054	-0.008	-0.028	-0.044	-0.011	-0.028	-0.035	-0.011	-0.028	0.049	0.010	0.029
O3LYP	0.014	-0.013	-0.029	0.021	-0.010	-0.027	0.039	-0.014	-0.027	0.049	-0.014	-0.027	0.031	0.013	0.028
hmGGA															
M06-HF	-0.024	0.089	0.054	0.005	0.113	0.071	-0.019	0.081	0.049	-0.003	0.074	0.043	0.013	0.089	0.054
M05-2X	-0.029	0.019	0.004	-0.013	0.028	0.011	-0.014	0.017	0.006	-0.004	0.015	0.005	0.015	0.020	0.006
M06-2X	-0.027	0.038	0.025	0.005	0.050	0.034	-0.007	0.034	0.026	0.002	0.031	0.025	0.010	0.038	0.028
MPWB1K	-0.133	-0.004	-0.023	-0.098	0.002	-0.020	-0.108	-0.003	-0.020	-0.099	-0.004	-0.020	0.110	0.003	0.021
BB1K	-0.129	-0.004	-0.023	-0.095	0.001	-0.020	-0.105	-0.004	-0.020	-0.095	-0.005	-0.020	0.106	0.004	0.021
M05	-0.076	-0.001	-0.020	-0.046	0.002	-0.019	-0.041	-0.001	-0.018	-0.042	-0.002	-0.019	0.051	0.002	0.019
B1B95	-0.126	-0.008	-0.026	-0.096	-0.003	-0.024	-0.104	-0.006	-0.023	-0.091	-0.007	-0.023	0.104	0.006	0.024
M06	-0.064	0.009	-0.014	-0.063	0.014	-0.012	-0.044	0.012	-0.009	-0.043	0.011	-0.010	0.053	0.011	0.011
TPSSH	-0.080	0.003	-0.018	-0.062	0.007	-0.016	-0.060	0.003	-0.016	-0.051	0.003	-0.017	0.063	0.004	0.017
LC-hGGA															
CAM-B3LYP	-0.045	0.004	-0.018	-0.031	0.011	-0.014	-0.018	0.007	-0.013	-0.011	0.006	-0.014	0.026	0.007	0.015
LC-ωPBE	-0.141	-0.016	-0.038	-0.120	-0.012	-0.036	-0.121	-0.015	-0.035	-0.111	-0.015	-0.035	0.123	0.014	0.036
Expt.[c]	2.977	1.803	1.873	2.977	1.803	1.873	2.977	1.803	1.873	2.977	1.803	1.873			

[a,b] See C1a footnotes.

[c] Almenningen, A.; Jacobsen, G. G.; Seip, H. M. *Acta Chem. Scand.* **1969,** *23,* 685–686.

Table C1b : $Ni(CO)_4$ - comparison with DZP bond lengths

DFT functional	DZP Ni-C	Δ cc-pVDZ[a] Ni-C	Δ cc-pVTZ[a] Ni-C	Δ cc-pVQZ[a] Ni-C
GGA				
BLYP	1.847	0.005	0.006	0.005
BP86	1.826	0.003	0.002	0.001
B97-D	1.843	0.003	0.002	0.001
HCTH147	1.833	0.003	0.001	0.000
HCTH407	1.831	0.002	0.001	0.000
Meta GGA				
M06-L	1.838	0.002	-0.001	-0.003
VSXC	1.859	0.004	0.001	0.001
Hybrid GGA				
BHLYP	1.848	0.006	0.005	0.004
MPW1K	1.823	0.003	0.002	0.001
BHandH	1.832	0.004	0.004	0.003
MPW1PW91	1.823	0.003	0.002	0.001
MPW1PBE	1.821	0.003	0.002	0.001
B1LYP	1.846	0.005	0.005	0.004
PBE1PBE	1.821	0.003	0.002	0.001
MPW1LYP	1.844	0.006	0.006	0.005
B98	1.837	0.004	0.003	0.002
X3LYP	1.840	0.005	0.005	0.004
B97-1	1.838	0.004	0.003	0.002
B97-2	1.831	0.003	0.002	0.001
MPW3PBE	1.821	0.003	0.002	0.001
B3LYP	1.841	0.005	0.005	0.004
B3PW91	1.824	0.003	0.002	0.001
B3P86	1.820	0.003	0.002	0.001
O3LYP	1.831	0.003	0.001	0.001
Hybrid Meta GGA				
M06-HF	1.929	0.001	-0.003	-0.000
M05-2X	1.871	0.006	0.005	0.004
M06-2X	1.899	0.007	0.006	0.006
MPWB1K	1.827	0.003	0.002	0.001
BB1K	1.828	0.003	0.002	0.001
M05	1.845	0.005	0.006	0.003
B1B95	1.827	0.003	0.002	0.001
M06	1.844	0.005	0.007	0.005
TPSSH	1.827	0.003	0.001	0.000
LC Hybrid GGA				
CAM-B3LYP	1.831	0.005	0.005	0.004
LC-ωPBE	1.817	0.003	0.002	0.001
Experiment-1 [b]	1.838	1.838	1.838	1.838
Experiment-2 [c]	1.84	1.84	1.84	1.84
Experiment-3 [d]	1.817	1.817	1.817	1.817

[a] Δ cc-pVXZ = cc-pVXZ bond length − DZP bond length, (X = D, T, Q).

[b] Hedberg, L.; Iijima, T.; Hedberg, K. *J. Chem. Phys.* **1979,** *70,* 3224–3229.

[c] Ladell, J.; Post, B.; Fankuchen, I. *Acta Cryst.* **1952,** *5,* 795–800.

[d] Braga, D.; Grepioni, F.; Orpen, A. G. *Organometallics* **1993,** *12,* 1481–1483.

Table C2b : $Fe(CO)_5$ - comparison with DZP bond lengths

DFT functional	DZP		Δ cc-pVDZ[a]		Δ cc-pVTZ[a]		Δ cc-pVQZ[a]	
	Fe-C^{ax}	Fe-C^{eq}	Fe-C^{ax}	Fe-C^{eq}	Fe-C^{ax}	Fe-C^{eq}	Fe-C^{ax}	Fe-C^{eq}
GGA								
BLYP	1.826	1.827	0.008	0.006	0.005	0.006	0.005	0.005
BP86	1.805	1.805	0.006	0.004	0.004	0.004	0.003	0.003
B97-D	1.812	1.812	0.006	0.005	0.004	0.004	0.003	0.004
HCTH147	1.799	1.801	0.006	0.005	0.003	0.004	0.002	0.003
HCTH407	1.794	1.796	0.005	0.005	0.003	0.004	0.002	0.002
Meta GGA								
M06-L	1.816	1.813	0.005	0.003	-0.000	-0.001	-0.001	-0.001
VSXC	1.835	1.835	0.005	0.004	0.002	0.002	0.002	0.002
Hybrid GGA								
BHLYP	1.854	1.822	0.011	0.006	0.005	0.005	0.005	0.004
MPW1K	1.812	1.794	0.007	0.004	0.002	0.003	0.002	0.003
BHandH	1.830	1.806	0.009	0.005	0.004	0.004	0.004	0.004
MPW1PW91	1.803	1.795	0.006	0.004	0.003	0.003	0.003	0.003
MPW1PBE	1.801	1.793	0.006	0.004	0.003	0.003	0.002	0.003
B1LYP	1.830	1.820	0.009	0.006	0.005	0.005	0.005	0.005
PBE1PBE	1.801	1.793	0.006	0.004	0.003	0.003	0.002	0.003
MPW1LYP	1.829	1.819	0.009	0.006	0.006	0.006	0.005	0.005
B98	1.816	1.809	0.008	0.005	0.004	0.004	0.003	0.003
X3LYP	1.823	1.815	0.008	0.006	0.005	0.005	0.005	0.005
B97-1	1.816	1.810	0.007	0.005	0.003	0.003	0.003	0.003
B97-2	1.805	1.799	0.006	0.004	0.003	0.003	0.002	0.003
MPW3PBE	1.801	1.795	0.006	0.005	0.003	0.004	0.003	0.003
B3LYP	1.823	1.816	0.008	0.006	0.005	0.005	0.004	0.005
B3PW91	1.803	1.797	0.006	0.004	0.003	0.003	0.003	0.003
B3P86	1.800	1.794	0.006	0.004	0.003	0.004	0.003	0.003
O3LYP	1.800	1.798	0.006	0.005	0.003	0.003	0.002	0.003
Hybrid Meta GGA								
M06-HF	1.964	1.849	0.028	0.011	-0.004	-0.004	-0.003	-0.009
M05-2X	1.853	1.824	0.012	0.007	0.001	0.001	0.001	0.000
M06-2X	1.883	1.840	0.015	0.008	-0.001	-0.001	-0.002	-0.002
MPWB1K	1.814	1.796	0.007	0.004	0.004	0.004	0.003	0.003
BB1K	1.813	1.797	0.007	0.004	0.003	0.004	0.003	0.003
M05	1.808	1.811	0.005	0.004	0.003	0.004	0.002	0.002
B1B95	1.806	1.797	0.006	0.004	0.004	0.004	0.003	0.004
M06	1.816	1.816	0.005	0.004	0.006	0.006	0.005	0.006
TPSSH	1.810	1.806	0.005	0.004	0.002	0.002	0.002	0.002
LC Hybrid GGA								
CAM-B3LYP	1.815	1.806	0.009	0.006	0.006	0.006	0.005	0.005
LC-ωPBE	1.791	1.789	0.006	0.004	0.004	0.004	0.004	0.004
Experiment-1[b]	1.807	1.827	1.807	1.827	1.807	1.827	1.807	1.827
Experiment-2[c]	1.810	1.842	1.810	1.842	1.810	1.842	1.810	1.842
Experiment-3[d]	1.811	1.803	1.811	1.803	1.811	1.803	1.811	1.803

[a] See C1b footnote.

[b] Beagley, B.; Schmidling, D. G. *J. Mol. Struct.* **1974,** *22,* 466–468.

[c] McClelland, B. W.; Robiette, A. G.; Hedberg, L.; Hedberg, K. *Inorg. Chem.* **2001,** *40,* 1358–1362.

[d] Braga, D.; Grepioni, F.; Orpen, A. G. *Organometallics* **1993,** *12,* 1481–1483.

Table C3b : $Cr(CO)_6$ - comparison with DZP bond lengths

DFT functional	DZP Cr-C	Δ cc-pVDZ[a] Cr-C	Δ cc-pVTZ[a] Cr-C	Δ cc-pVQZ[a] Cr-C
GGA				
BLYP	1.931	0.000	0.003	0.003
BP86	1.907	-0.001	0.001	0.002
B97-D	1.919	-0.001	0.002	0.002
HCTH147	1.903	-0.002	0.001	0.001
HCTH407	1.898	-0.001	0.001	0.001
Meta GGA				
M06-L	1.922	-0.003	-0.003	-0.001
VSXC	1.946	-0.003	0.000	0.001
Hybrid GGA				
BHLYP	1.933	-0.000	0.002	0.002
MPW1K	1.900	-0.003	-0.000	0.001
BHandH	1.915	-0.002	0.001	0.002
MPW1PW91	1.900	-0.002	0.000	0.001
MPW1PBE	1.897	-0.003	0.000	0.001
B1LYP	1.928	0.000	0.003	0.003
PBE1PBE	1.897	-0.002	0.000	0.001
MPW1LYP	1.927	0.000	0.003	0.003
B98	1.913	-0.001	0.001	0.001
X3LYP	1.922	-0.000	0.003	0.003
B97-1	1.914	-0.001	0.001	0.001
B97-2	1.904	-0.002	0.000	0.001
MPW3PBE	1.899	-0.002	0.001	0.002
B3LYP	1.923	-0.000	0.003	0.003
B3PW91	1.901	-0.002	0.001	0.002
B3P86	1.898	-0.002	0.001	0.002
O3LYP	1.900	-0.002	0.001	0.001
Hybrid Meta GGA				
M06-HF	1.950	0.004	-0.007	-0.010
M05-2X	1.929	-0.002	-0.001	-0.001
M06-2X	1.945	-0.001	-0.003	-0.003
MPWB1K	1.902	-0.003	0.001	0.002
BB1K	1.902	-0.003	0.001	0.002
M05	1.910	-0.003	0.000	-0.001
B1B95	1.901	-0.002	0.001	0.002
M06	1.915	-0.003	0.003	0.003
TPSSH	1.911	-0.002	0.000	0.001
LC Hybrid GGA				
CAM-B3LYP	1.913	-0.001	0.003	0.003
LC-ωPBE	1.891	-0.004	0.001	0.002
Experiment-1[b]	1.914	1.914	1.914	1.914
Experiment-2[c]	1.909	1.909	1.909	1.909
Experiment-3[d]	1.915	1.915	1.915	1.915

[a] See C1b footnote.

[b] Jost, A.; Rees, B.; Yelon, W. B. *Acta Cryst.* **1975,** *B31,* 2649–2658.

[c] Whitaker, A.; Jeffery, J. W. *Acta Cryst.* **1967,** *23,* 977–984.

[d] Rees, B.; Mitschler, A. *J. Am. Chem. Soc.* **1976,** *98,* 7918–7924.

Table C4b : $Co_2(CO)_8$ - comparison with DZP bond lengths

DFT	DZP				Δ cc-pVDZ[a]				Δ cc-pVTZ[a]				Δ cc-pVQZ[a]			
functional	Co-Co	Co-C^b	Co-C^{2t}	Co-C^{4t}	Co-Co	Co-C^b	Co-C^{2t}	Co-C^{4t}	Co-Co	Co-C^b	Co-C^{2t}	Co-C^{4t}	Co-Co	Co-C^b	Co-C^{2t}	Co-C^{4t}
GGA																
BLYP	2.599	1.982	1.828	1.835	0.008	0.004	0.005	0.006	0.007	0.006	0.006	0.005				
BP86	2.550	1.957	1.805	1.813	0.006	0.003	0.004	0.004	0.003	0.003	0.003	0.002				
B97-D	2.548	1.969	1.821	1.824	0.007	0.004	0.004	0.005	0.004	0.003	0.003	0.002				
HCTH147	2.554	1.957	1.806	1.812	0.008	0.003	0.004	0.005	0.004	0.002	0.003	0.001	0.007	0.002	0.003	0.001
HCTH407	2.545	1.952	1.802	1.808	0.009	0.003	0.004	0.005	0.003	0.001	0.003	0.000	0.007	0.001	0.003	0.001
Meta GGA																
M06-L	2.525	1.961	1.815	1.825	0.011	0.001	0.004	0.004	0.003	-0.000	-0.000	-0.003	0.001	-0.000	-0.001	-0.002
VSXC	2.496	1.990	1.841	1.859	0.003	-0.004	0.004	0.005	0.000	-0.003	0.003	0.002				
Hybrid GGA																
BHLYP	2.533	1.940	1.828	1.839	0.013	0.006	0.005	0.006	0.012	0.007	0.005	0.002	0.015	0.007	0.006	0.002
MPW1K	2.487	1.919	1.798	1.807	0.009	0.004	0.003	0.004	0.006	0.003	0.003	-0.001	0.009	0.003	0.003	-0.000
BHandH	2.504	1.926	1.809	1.819	0.012	0.005	0.004	0.005	0.009	0.005	0.004	0.001	0.012	0.005	0.005	0.001
MPW1PW91	2.507	1.932	1.798	1.806	0.007	0.003	0.004	0.004	0.005	0.003	0.003	0.000	0.008	0.003	0.003	0.000
MPW1PBE	2.503	1.930	1.796	1.804	0.007	0.003	0.004	0.004	0.005	0.003	0.003	0.000	0.008	0.003	0.003	0.000
B1LYP	2.559	1.956	1.825	1.832	0.011	0.005	0.005	0.006	0.009	0.006	0.005	0.003	0.012	0.006	0.006	0.003
PBE1PBE	2.503	1.930	1.796	1.803	0.008	0.003	0.004	0.004	0.005	0.003	0.003	0.000	0.008	0.002	0.003	0.000
MPW1LYP	2.557	1.955	1.823	1.830	0.011	0.005	0.005	0.006	0.010	0.006	0.006	0.004	0.013	0.006	0.006	0.004
B98	2.539	1.947	1.813	1.820	0.007	0.004	0.005	0.005	0.005	0.004	0.004	0.001	0.008	0.003	0.004	0.001
X3LYP	2.553	1.953	1.819	1.825	0.010	0.005	0.005	0.006	0.008	0.006	0.005	0.003	0.012	0.005	0.006	0.003
B97-1	2.539	1.949	1.813	1.821	0.008	0.004	0.004	0.005	0.005	0.004	0.004	0.001	0.008	0.003	0.004	0.001
B97-2	2.521	1.939	1.805	1.811	0.008	0.003	0.004	0.004	0.005	0.003	0.003	0.000	0.008	0.002	0.003	-0.000
MPW3PBE	2.513	1.935	1.798	1.805	0.007	0.003	0.004	0.004	0.005	0.003	0.003	0.001	0.008	0.003	0.003	0.001
B3LYP	2.557	1.955	1.820	1.826	0.010	0.005	0.005	0.006	0.008	0.006	0.005	0.003	0.012	0.005	0.006	0.003
B3PW91	2.517	1.937	1.800	1.807	0.007	0.003	0.004	0.004	0.004	0.003	0.003	0.001	0.008	0.003	0.003	0.001
B3P86	2.514	1.933	1.797	1.804	0.007	0.004	0.004	0.004	0.005	0.003	0.003	0.001	0.008	0.003	0.004	0.001
O3LYP	2.531	1.944	1.803	1.809	0.006	0.003	0.004	0.004	0.003	0.001	0.002	0.000	0.007	0.001	0.003	0.000
Hybrid Meta GGA																
M06-HF	2.661	2.031	1.942	1.927	0.017	0.034	0.004	0.006	0.013	0.017	-0.001	-0.001	0.018	0.020	0.006	-0.006
M05-2X	2.554	1.947	1.845	1.847	0.013	0.008	0.004	0.005	0.011	0.007	0.004	-0.002	0.013	0.007	0.004	-0.002
M06-2X	2.575	1.965	1.864	1.873	0.017	0.008	0.004	0.007	0.015	0.007	0.003	-0.003	0.018	0.008	0.004	-0.002
MPWB1K	2.468	1.916	1.801	1.810	0.009	0.003	0.004	0.004	0.005	0.002	0.004	0.000	0.008	0.002	0.004	0.000
BB1K	2.471	1.919	1.802	1.810	0.009	0.003	0.003	0.004	0.005	0.002	0.003	0.000	0.008	0.002	0.004	0.000
M05	2.520	1.945	1.825	1.817	0.010	0.001	0.007	0.005	0.006	0.004	0.008	0.002	0.006	0.002	0.007	0.001
B1B95	2.487	1.929	1.802	1.809	0.008	0.003	0.004	0.004	0.004	0.002	0.003	0.001	0.007	0.002	0.004	0.001
M06	2.531	1.947	1.826	1.824	0.007	0.001	0.005	0.004	0.007	0.006	0.007	0.005	0.007	0.005	0.007	0.004
TPSSH	2.514	1.946	1.806	1.816	0.006	0.002	0.003	0.004	0.002	0.001	0.002	0.000	0.005	0.001	0.002	0.000
LC Hybrid GGA																
CAM-B3LYP	2.514	1.930	1.812	1.818	0.011	0.004	0.005	0.006	0.009	0.005	0.006	0.004	0.012	0.005	0.006	0.004
LC-ωPBE	2.477	1.918	1.795	1.801	0.008	0.003	0.004	0.004	0.004	0.002	0.003	0.002				
Experiment-1 [b]	2.528	1.939	1.816	1.832	2.528	1.939	1.816	1.832	2.528	1.939	1.816	1.832	2.528	1.939	1.816	1.832

[a] See C1b footnote.

[b] Leung, P. C.; Coppens, P. *Acta Cryst.* **1983,** *B39,* 535–542.

Table C5b : $Fe_2(CO)_9$ - comparison with DZP bond lengths

DFT		DZP		Δ cc-pVDZ[a]			Δ cc-pVTZ[a]			Δ cc-pVQZ[a]		
functional	Fe-Fe	Fe-C[b]	Fe-C[t]	Fe-Fe	Fe-C[b]	Fe-C[t]	Fe-Fe	Fe-C[b]	Fe-C[t]	Fe-Fe	Fe-C[b]	Fe-C[t]
GGA												
BLYP	2.566	2.034	1.841	0.009	0.006	0.008	0.006	0.006	0.005	0.009	0.006	0.005
BP86	2.519	2.006	1.819	0.006	0.004	0.007	0.002	0.003	0.003	0.005	0.003	0.003
B97-D	2.536	2.020	1.829	0.008	0.005	0.008	0.004	0.004	0.004	0.006	0.004	0.003
HCTH147	2.516	2.004	1.815	0.008	0.004	0.007	0.002	0.003	0.003	0.005	0.003	0.002
HCTH407	2.504	1.998	1.810	0.009	0.004	0.007	0.001	0.002	0.002	0.004	0.002	0.002
Meta GGA												
M06-L	2.515	2.010	1.827	0.006	0.001	0.007	-0.003	-0.002	-0.001	-0.000	-0.001	-0.001
VSXC	2.561	2.034	1.856	-0.001	-0.003	0.008	-0.002	-0.000	0.003	0.000	-0.000	0.003
Hybrid GGA												
BHLYP	2.502	1.996	1.839	0.013	0.008	0.008	0.007	0.006	0.003	0.009	0.006	0.004
MPW1K	2.459	1.970	1.807	0.007	0.004	0.006	0.003	0.003	0.001	0.005	0.003	0.002
BHandH	2.473	1.978	1.819	0.011	0.006	0.007	0.005	0.004	0.003	0.007	0.005	0.003
MPW1PW91	2.479	1.981	1.807	0.006	0.003	0.007	0.003	0.002	0.002	0.005	0.003	0.002
MPW1PBE	2.475	1.979	1.805	0.006	0.003	0.006	0.002	0.002	0.002	0.005	0.003	0.002
B1LYP	2.528	2.009	1.833	0.011	0.006	0.008	0.007	0.006	0.004	0.009	0.006	0.004
PBE1PBE	2.473	1.978	1.805	0.006	0.003	0.006	0.002	0.002	0.002	0.005	0.002	0.002
MPW1LYP	2.526	2.008	1.832	0.011	0.006	0.008	0.007	0.006	0.004	0.009	0.006	0.004
B98	2.507	1.998	1.821	0.008	0.005	0.008	0.003	0.003	0.002	0.005	0.003	0.003
X3LYP	2.522	2.005	1.828	0.010	0.006	0.008	0.006	0.005	0.004	0.009	0.006	0.004
B97-1	2.507	2.000	1.822	0.008	0.004	0.008	0.002	0.002	0.002	0.005	0.003	0.003
B97-2	2.490	1.987	1.812	0.007	0.003	0.006	0.003	0.002	0.002	0.005	0.003	0.002
MPW3PBE	2.484	1.984	1.807	0.007	0.003	0.007	0.003	0.003	0.003	0.005	0.003	0.003
B3LYP	2.526	2.008	1.829	0.010	0.006	0.008	0.006	0.005	0.004	0.009	0.006	0.004
B3PW91	2.488	1.986	1.810	0.007	0.003	0.007	0.003	0.003	0.002	0.005	0.003	0.002
B3P86	2.483	1.982	1.807	0.007	0.004	0.007	0.003	0.003	0.003	0.006	0.003	0.003
O3LYP	2.495	1.991	1.810	0.006	0.002	0.007	0.001	0.001	0.002	0.004	0.002	0.002
Hybrid Meta GGA												
M06-HF	2.477	2.026	1.894	0.019	0.031	0.015	-0.010	0.005	-0.007	-0.006	0.005	-0.007
M05-2X	2.498	1.996	1.839	0.016	0.011	0.009	0.005	0.007	0.000	0.008	0.007	0.000
M06-2X	2.517	2.014	1.859	0.018	0.013	0.010	0.002	0.004	-0.002	0.005	0.005	-0.001
MPWB1K	2.449	1.965	1.809	0.005	0.003	0.007	0.002	0.002	0.003	0.004	0.002	0.003
BB1K	2.453	1.967	1.810	0.005	0.003	0.007	0.002	0.002	0.002	0.004	0.002	0.002
M05	2.479	1.988	1.821	0.006	-0.001	0.008	0.001	0.001	0.003	0.000	-0.000	0.002
B1B95	2.468	1.976	1.810	0.005	0.002	0.007	0.001	0.001	0.003	0.004	0.002	0.003
M06	2.497	1.993	1.827	0.004	0.001	0.007	0.005	0.005	0.006	0.007	0.005	0.005
TPSSH	2.499	1.996	1.819	0.005	0.002	0.007	0.000	0.001	0.002	0.003	0.001	0.002
LC Hybrid GGA												
CAM-B3LYP	2.485	1.980	1.821	0.009	0.005	0.008	0.006	0.005	0.005	0.008	0.005	0.005
LC-ωPBE	2.452	1.963	1.804	0.005	0.001	0.007	0.002	0.002	0.003	0.004	0.002	0.003
Experiment [b]	2.523	2.016	1.838	2.523	2.016	1.838	2.523	2.016	1.838	2.523	2.016	1.838

[a] See C1b footnote.

[b] Cotton, F. A.; Troup, J. M. *J. Chem. Soc., Dalton Trans.* **1974,** 800–802.

Table C6b : $Mn_2(CO)_{10}$ - comparison with DZP bond lengths

DFT	DZP			Δ cc-pVDZ[a]			Δ cc-pVTZ[a]			Δ cc-pVQZ[a]		
functional	Mn-Mn	Mn-C^{ax}	Mn-C^{eq}	Mn-Mn	Mn-C^{ax}	Mn-C^{eq}	Mn-Mn	Mn-C^{ax}	Mn-C^{eq}	Mn-Mn	Mn-C^{ax}	Mn-C^{eq}
BLYP	3.067	1.825	1.871	-0.011	0.006	0.004	0.027	0.004	0.005	0.035	0.003	0.004
BP86	2.955	1.803	1.851	0.001	0.004	0.002	0.018	0.002	0.003	0.028	0.001	0.002
B97-D	2.988	1.812	1.855	0.001	0.005	0.002	0.016	0.002	0.003	0.023	0.001	0.002
HCTH147	3.037	1.792	1.845	-0.006	0.003	0.002	0.024	0.001	0.002	0.034	0.000	0.002
HCTH407	3.046	1.786	1.841	-0.015	0.010	0.006	0.028	0.000	0.002	0.038	-0.000	0.001
Meta GGA												
M06-L	2.901	1.811	1.864	0.038	0.004	0.002	0.033	-0.002	-0.001	0.037	-0.003	-0.000
VSXC	2.973	1.841	1.883	0.032	0.007	0.001	0.021	0.002	0.002	0.034	0.001	0.002
Hybrid GGA												
BHLYP	3.013	1.832	1.881	0.019	0.009	0.007	0.031	0.002	0.005	0.037	0.001	0.004
MPW1K	2.903	1.796	1.848	0.021	0.004	0.003	0.024	-0.001	0.002	0.032	-0.001	0.002
BHandH	2.953	1.812	1.862	0.021	0.007	0.005	0.027	0.001	0.004	0.034	0.000	0.003
MPW1PW91	2.910	1.793	1.845	0.014	0.004	0.002	0.022	0.000	0.002	0.031	-0.000	0.002
MPW1PBE	2.915	1.792	1.843	0.012	0.004	0.002	0.022	0.000	0.002	0.030	-0.000	0.002
B1LYP	3.019	1.820	1.870	0.006	0.007	0.005	0.029	0.002	0.004	0.035	0.002	0.004
PBE1PBE	2.897	1.791	1.842	0.017	0.004	0.002	0.022	-0.000	0.002	0.031	-0.000	0.002
MPW1LYP	3.010	1.819	1.869	0.006	0.007	0.005	0.029	0.003	0.005	0.035	0.002	0.004
B98	2.968	1.807	1.858	0.009	0.006	0.003	0.022	0.001	0.003	0.030	0.000	0.003
X3LYP	2.998	1.814	1.864	0.006	0.006	0.004	0.027	0.002	0.004	0.034	0.002	0.004
B97-1	2.958	1.808	1.859	0.012	0.005	0.003	0.022	0.001	0.002	0.030	0.000	0.002
B97-2	2.958	1.794	1.848	0.011	0.003	0.002	0.024	-0.000	0.002	0.033	-0.001	0.002
MPW3PBE	2.903	1.791	1.843	0.015	0.003	0.002	0.022	-0.000	0.002	0.031	-0.001	0.002
B3LYP	3.007	1.814	1.864	0.004	0.006	0.004	0.027	0.002	0.004	0.034	0.002	0.004
B3PW91	2.928	1.794	1.846	0.011	0.004	0.002	0.021	0.000	0.002	0.030	-0.000	0.002
B3P86	2.912	1.792	1.842	0.011	0.004	0.002	0.021	0.000	0.003	0.030	0.000	0.002
O3LYP	2.991	1.790	1.844	0.006	0.003	0.001	0.025	-0.000	0.002	0.034	-0.001	0.001
Hybrid Meta GGA												
M06-HF	2.953	1.892	1.927	0.028	0.024	0.016	0.005	-0.009	-0.005	0.020	-0.015	-0.011
M05-2X	2.948	1.822	1.877	0.016	0.009	0.007	0.015	-0.003	0.002	0.025	-0.005	0.001
M06-2X	2.950	1.841	1.898	0.032	0.012	0.009	0.020	-0.004	0.000	0.029	-0.007	-0.000
MPWB1K	2.844	1.799	1.850	0.035	0.006	0.004	0.024	0.001	0.003	0.033	-0.000	0.003
BB1K	2.848	1.799	1.850	0.034	0.006	0.003	0.024	0.000	0.003	0.034	-0.000	0.003
M05	2.901	1.802	1.853	0.030	0.004	0.001	0.034	0.001	0.002	0.034	-0.001	0.001
B1B95	2.851	1.795	1.847	0.030	0.005	0.002	0.022	0.001	0.003	0.034	0.000	0.003
M06	2.913	1.812	1.859	0.001	0.005	0.002	0.020	0.004	0.005	0.021	0.003	0.004
TPSSH	2.897	1.806	1.855	0.018	0.004	0.002	0.020	0.000	0.002	0.029	-0.000	0.001
LC Hybrid GGA												
CAM-B3LYP	2.932	1.807	1.855	0.014	0.007	0.005	0.028	0.003	0.005	0.035	0.002	0.004
LC-ωPBE	2.836	1.787	1.835	0.021	0.004	0.002	0.021	0.001	0.003	0.030	0.000	0.003
Experiment-1[b]	2.895	1.820	1.859	2.895	1.820	1.859	2.895	1.820	1.859	2.895	1.820	1.859
Experiment-2[c]	2.923	1.792	1.830	2.923	1.792	1.830	2.923	1.792	1.830	2.923	1.792	1.830
Experiment-3[d]	2.977	1.803	1.873	2.977	1.803	1.873	2.977	1.803	1.873	2.977	1.803	1.873

[a] See C1b footnote.

[b] Martin, M.; Rees, B.; Mitschler, A. *Acta Cryst.* **1982,** *B38,* 6–15.

[c] Dahl, L. F.; Rundle, R. E. *Acta Cryst.* **1963,** *16,* 419–426.

[d] Almenningen, A.; Jacobsen, G. G.; Seip, H. M. *Acta Chem. Scand.* **1969,** *23*, 685–686.